Open access • Posted Content • DOI:10.1101/2020.05.28.120543

Quantitative live-cell imaging yields novel insight into endogenous WNT/CTNNB1 signaling dynamics — Source link

Saskia Madelon Ada de Man, Gooitzen Zwanenburg, Mark A. Hink, Renée van Amerongen

Institutions: University of Amsterdam

Published on: 28 May 2020 - bioRxiv (Cold Spring Harbor Laboratory)

Topics: Wnt signaling pathway and Live cell imaging

Quantitative live-cell imaging and computational modelling yield novel insight into endogenous WNT/CTNNB1 signaling dynamics

Author information

S.M.A. de Man[1], G. Zwanenburg[2,^], T. van der Wal[1], M.A. Hink[3,4,*,^], R. van Amerongen[1,*,^,#]

[1] Developmental, Stem Cell and Cancer Biology, Swammerdam Institute for Life Sciences, University of Amsterdam, Amsterdam, The Netherlands

[2] Biosystems Data Analysis, Swammerdam Institute for Life Sciences, University of Amsterdam, Amsterdam, The Netherlands

[3] Molecular Cytology, Swammerdam Institute for Life Sciences, University of Amsterdam, Amsterdam, the Netherlands

[4] van Leeuwenhoek Centre for Advanced Microscopy, Swammerdam Institute for Life Sciences, University of Amsterdam, Amsterdam, the Netherlands

* These authors contributed equally

^ corresponding authors: r.vanamerongen@uva.nl (RvA, lead contact), m.a.hink@uva.nl (MAH), g.zwanenburg@uva.nl (GZ)

Twitter: @wntlab

Abstract

WNT/CTNNB1 signaling regulates tissue development and homeostasis in all multicellular animals. Multiple aspects of the underlying molecular mechanism remain poorly understood and critical information on endogenous WNT/CTNNB1 signaling dynamics is missing. Here we combine CRISPR/Cas9-mediated genome editing and quantitative live-cell microscopy to measure diffusion characteristics of fluorescently tagged, endogenous CTNNB1 in human cells with high spatiotemporal resolution under both physiological and oncogenic conditions. State-of-the-art functional imaging reveals that a substantial fraction of CTNNB1 resides in slow-diffusing complexes in the cytoplasm, irrespective of the activation status of the pathway. The identity of this cytoplasmic CTNNB1 complex changes according to the phosphorylation status of CTNNB1 as it undergoes a major reduction in size when WNT/CTNNB1 is (hyper)activated. We also measure the concentration of complexed and free CTNNB1 in both the cytoplasm and the nucleus before and after WNT stimulation, and use these parameters to build a minimal computational model of WNT/CTNNB1 signaling. Using this integrated experimental and computational approach, our work reveals that WNT pathway activation regulates the dynamic distribution of CTNNB1 across different functional pools by modulating three regulatory nodes: the cytoplasmic destruction complex, nucleocytoplasmic shuttling and nuclear retention.

Introduction

WNT signaling is one of the most ancient pattern-forming cell signaling cascades. It drives many biological processes from the onset of embryogenesis until adulthood in all multicellular animals (reviewed in van Amerongen and Nusse, 2009; Holstein, 2012; Loh et al., 2016). WNT signaling remains important throughout the lifespan of the organism and controls stem cell maintenance in many mammalian tissues, including the breast, intestine and skin (van Amerongen et al., 2012; Barker et al., 2007; Lim et al., 2013). Disruption of the pathway causes disease, with hyperactivation being a frequent event in human colorectal and other cancers (reviewed in Nusse & Clevers, 2017; Wiese, Nusse, & van Amerongen, 2018).

The key regulatory event in WNT/CTNNB1 signaling (traditionally known as 'canonical WNT signaling') is the accumulation and nuclear translocation of the transcriptional co-activator beta-catenin (CTNNB1) (Figure 1A). In the absence of WNT signaling, rapid turnover by the so-called destruction complex maintains low levels of CTNNB1. This cytoplasmic complex consists of the scaffold proteins APC and AXIN, which bind CTNNB1, and the serine/threonine kinases CSNK1 and GSK3, which subsequently phosphorylate residues S45, T41, S37 and S33 (Amit et al., 2002; Liu et al., 2002). This primes CTNNB1 for ubiquitination by E3 Ubiquitin Protein Ligase BTRC and subsequent proteasomal degradation (Aberle et al., 1997; Latres et al., 1999). In the current working model for WNT/CTNNB1 signaling, binding of WNT ligands to the FZD/LRP receptor complex sequesters and inhibits the destruction complex at the membrane in a process that involves DVL (Bilic et al., 2007; Schwarz-Romond et al., 2007). This allows newly synthesized CTNNB1 to accumulate. Upon stimulation, CTNNB1 also translocates to the nucleus, where CTNNB1 binds to TCF/LEF transcription factors to regulate target gene transcription as part of a larger transcriptional complex (Behrens et al., 1996; Fiedler et al., 2015; Molenaar et al., 1996; van Tienen et al., 2017).

The working model for WNT/CTNNB1 signaling described above is the result of almost 40 years of research. The use of traditional genetic and biochemical approaches has allowed identification of the core players, as well as dissection of the main signaling events. However, multiple aspects of WNT/CTNNB1 signaling remain poorly understood. For instance the exact molecular composition of the destruction complex as well as the mechanism for its inhibition remain unclear (reviewed in Tortelote et al., 2017), and how WNT/CTNNB1 signaling regulates the subcellular distribution of CTNNB1 requires further scrutiny.

Most biochemical techniques lead to loss of spatial information and averaging of cell-to-cell heterogeneity, since proteins are extracted from their cellular context. Additionally, temporal information is usually limited to intervals of several minutes or hours. Live-cell microscopy offers better spatiotemporal resolution. Currently, however, many of these studies are conducted by overexpressing the protein(s) of interest. This can severely affect activation, localization and complex formation (Gibson et al., 2013; Mahen et al., 2014). Although stabilization of CTNNB1 by WNT signaling has been extensively studied, very few studies have focused on the spatiotemporal dynamics of this process – especially at the endogenous level (Chhabra et al., 2019; Massey et al., 2019; Rim et al., 2020).

Here we use CRISPR/Cas9 mediated genome editing in haploid cells to generate clonal cell lines that express fluorescently tagged CTNNB1. Using confocal imaging and automated cell segmentation we quantify the dynamic subcellular increase of endogenous CTNNB1 upon WNT stimulation. Moreover, using Fluorescence Correlation Spectroscopy (FCS) and Number and Brightness (N&B) analysis we measure the mobility and concentration of CTNNB1, providing detailed information on CTNNB1 containing complexes in the cytoplasm and nucleus. Next, we use these biophysical parameters to build a computational model of

WNT/CTNNB1 signaling that predicts the levels and subcellular distribution of CTNNB1 across its cytoplasmic and nuclear pools. Using this integrated experimental and computational approach, we find that WNT regulates the dynamic distribution of CTNNB1 across different functional pools by modulating three regulatory nodes: cytoplasmic destruction, nucleocytoplasmic shuttling and nuclear retention. Finally, we strengthen the link between our data and the model via specific experimental perturbations, which shows that the regulatory nodes responsible for nuclear retention and nuclear shuttling of CTNNB1 are equally important under physiological and oncogenic conditions.

Results

Generation and functional validation of clonal HAP1$^{SGFP2\text{-}CTNNB1}$ cell lines

To visualize and quantify the spatiotemporal dynamics of WNT/CTNNB1 signaling at the endogenous level, we fluorescently tagged CTNNB1 in mammalian cells using CRISPR/Cas9 mediated homology directed repair (Ran et al., 2013) (Figure 1). To preserve the existing (epi)genetic control mechanisms of *CTNNB1* expression, only the coding sequence for SGFP2, a monomeric, bright and photostable green fluorescent protein (Kremers et al., 2007), was seamlessly inserted at the starting ATG of the *CTNNB1* coding sequence in HAP1 cells, a WNT-responsive near haploid cell line (Figure 1B, Figure 1 supplement 2A)(Andersson et al., 1987; Carette et al., 2011; Kotecki et al., 1999; Lebensohn et al., 2016). The choice for this haploid cell line ensured homozygous tagging of CTNNB1 (Figure 1C), thus overcoming the limitations of polyploid cell lines where genome editing often results in a combination of correctly and incorrectly edited alleles (Canaj et al., 2019).

We isolated clonal cell lines with the desired modification by FACS sorting (Figure 1D-F) with a gating strategy that specifically selected for haploid cells (Figure 1 supplement 1) as HAP1

cells can become diploid or polyploid over time (Essletzbichler et al., 2014; Yaguchi et al., 2018). Genome editing of wild-type HAP1 ($HAP1^{WT}$) cells resulted in a small population with low SGFP2 fluorescence (0.2%) (Figure 1D-E). The intensity, but not the number of cells in this population increased upon treatment with CHIR99021, a potent and selective GSK3 inhibitor (Bain et al., 2007), providing a strong indication that these fluorescent events corresponded to HAP1 cells in which the *SGFP2* sequence was successfully knocked into the endogenous *CTNNB1* locus ($HAP1^{SGFP2\text{-}CTNNB1}$) (Figure 1F). While scarless tagging of endogenous genes in HAP1 cells was relatively cumbersome (only 0.2% gated events), PCR based screening and sanger sequencing revealed that the desired repair occurred with almost 90% efficiency within this population (Figure 1 supplement 2).

Figure 1: Generation of $HAP1^{SGFP2\text{-}CTNNB1}$ cell lines. A) Cartoon depicting the current model of the WNT/CTNNB1 pathway. In the absence of WNT ligands (left, "OFF"), free cytoplasmic CTNNB1 is captured by the destruction complex consisting of AXIN, APC, CSNK1 and GSK3, which leads to its phosphorylation, BTRC mediated ubiquitination and subsequent proteasomal degradation, resulting in low levels of CTNNB1 in the cytoplasm and nucleus. Binding of the WNT protein (right, "ON") to the FZD and LRP receptors inhibits the destruction complex through DVL. CTNNB1 accumulates in the cytoplasm and subsequently translocates to the nucleus, where it promotes the transcription of target genes, such as AXIN2, as a co-activator of TCF/LEF transcription factors. B) Cartoon depicting exon 2 of the *CTNNB1* locus, which contains the start codon, and the CTNNB1 protein before (top) and after (bottom) introduction of the SGFP2 by CRISPR/Cas9 mediated homology directed repair. C) Schematic of the experimental workflow and timeline for generating $HAP1^{SGFP2\text{-}CTNNB1}$ clones. Cas9, gRNA and repair templates are transfected as plasmids. The repair template contains the coding sequence of SGFP2 surrounded by 800 bp homology arms on either side and lacks the gRNA recognition site (see supplement 2 of this figure). A short puromycin selection step is included from 24-48 hours after transfection to enrich for transfected cells. Haploid, GFP-positive cells are sorted and single cell clones are expanded for further analysis. D-F) FACS plots illustrating control (D) and SGFP2-CTNNB1 tagged cells (E-F). D) Cells transfected with Cas9 and gRNA in the absence of a repair template were used to set the gate for SGFP2-positive events. E) A small population of cells expressing low levels of SGFP2 can be detected when cells are transfected with Cas9, gRNA and repair template. F) Treatment for 24 hours of cells similar to those depicted in (D) with 8µM CHIR99021 does not change the amount of cells that are SGFP2 positive, but increases the SFP2 signal, most likely reflecting an increase in SGFP2-tagged beta catenin levels on a per cell basis and supporting the notion that the gated events indeed represent successfully tagged cells.
The following figure supplements are available for Figure 2:
Figure supplement 1: FACS Gating strategy for haploid HAP1 cells.
Figure supplement 2 : *SGFP2-CTNNB1* locus.

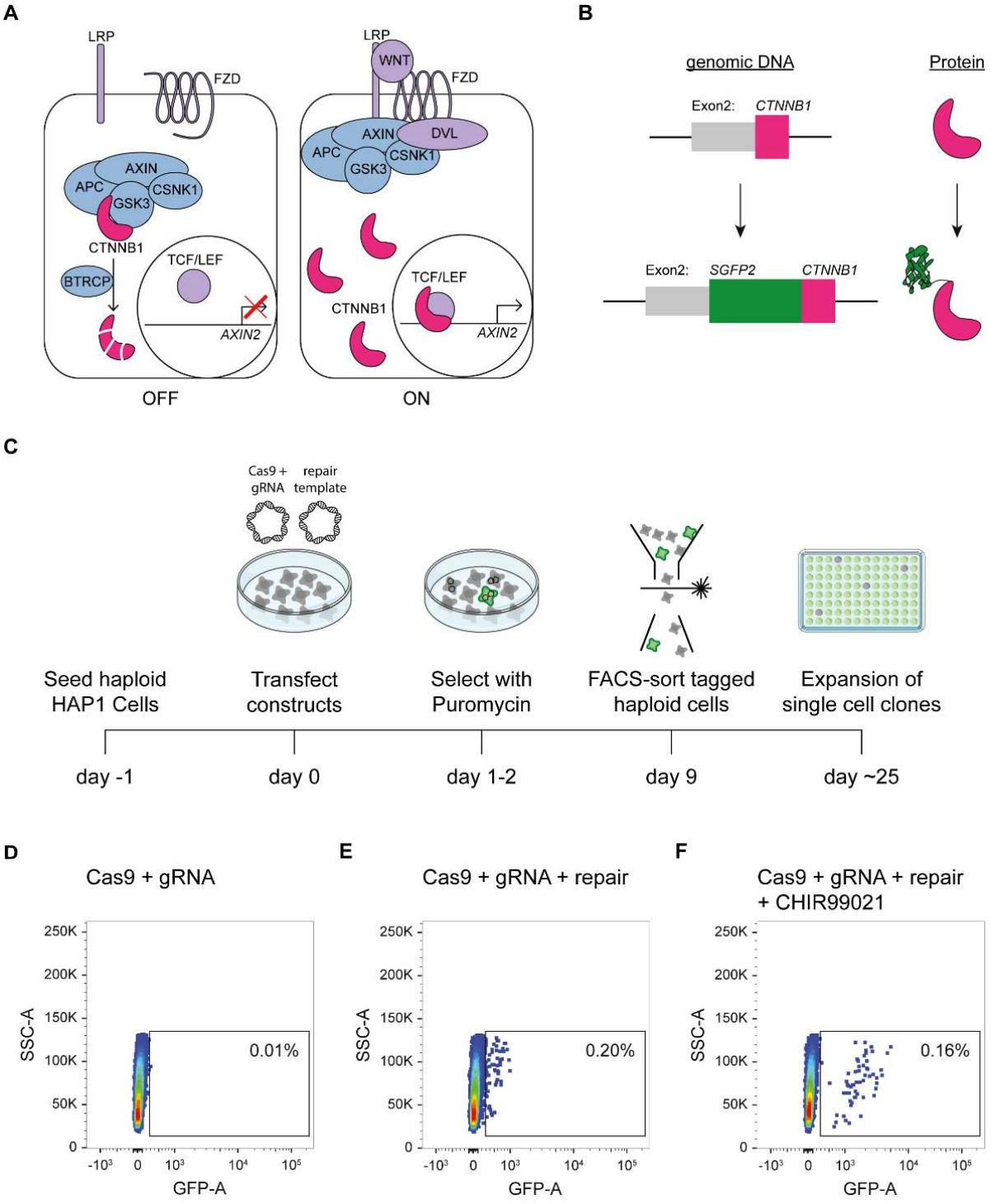

To verify that the SGFP2 tag did not interfere with CTNNB1 function, three clonal HAP1$^{SGFP2\text{-}CTNNB1}$ cell lines were further characterized using established experimental readouts for WNT/CTNNB1 signaling (Figure 2 and Figure 2 supplement 1). Western blot analysis confirmed that the HAP1$^{SGFP2\text{-}CTNNB1}$ clones did not contain any untagged CTNNB1 but only expressed the SGFP2-CTNNB1 fusion protein (Figure 2A). Moreover, the total levels of SGFP2-

CTNNB1 in tagged cell lines increased to the same extent as wild-type CTNNB1 in untagged cells in response to CHIR99021 treatment (Figure 2A-B). Similarly, untagged and tagged CTNNB1 induced target gene expression in equal measure, as measured by a TCF/LEF responsive luciferase reporter (Hu et al., 2007) (Figure 2C), and increased transcription of the universal WNT/CTNNB1 target *AXIN2* (Lustig et al., 2002) (Figure 2D). Finally, while unstimulated cells mainly showed SGFP2-CTNNB1 localization at the adherens junction, treatment with purified WNT3A protein (Figure 2E) and CHIR99021 (Figure 2 supplement 1E) increased SGFP2-CTNNB1 levels in the cytoplasm and nucleus consistent with its signaling function.

Taken together, WNT-responsive changes in CTNNB1 levels, localization and activity are preserved after CRISPR/Cas9 mediated homozygous tagging of CTNNB1. Although there is some variation between the three clones with respect to CTNNB1 stabilization and target gene activation, this is likely due to the sub-cloning of these cell lines rather than the targeting per se.

Figure2: Functional validation of three independent HAP1$^{SGFP2\text{-}CTNNB1}$ clones. A) Western blot, showing CTNNB1 (HAP1^{WT}) and SGFP2-CTNNB1 (HAP1$^{SGFP2\text{-}CTNNB1}$ clone 1, 2 and 3) accumulation in response to CHIR99021 treatment. All panels are from one blot that was cut at the 70 kDa mark and was stained with secondary antibodies with different fluorophores for detection. Top: HAP1^{WT} cells express CTNNB1 at the expected wild-type size. Each of the three clonal HAP1$^{SGFP2\text{-}CTNNB1}$ cell lines only express the larger, SGFP2-tagged form of CTNNB1, that runs at the expected height (~27 kDa above the wild-type CTNNB1). Middle: Only the tagged clones express the SGFP2-CTNNB1 fusion protein, as detected with an anti-GFP antibody at the same height. Bottom: alpha-Tubulin (TUBA) loading control. A representative image of n=3 independent experiments is shown. B) Quantification of Western blots from n=3 independent experiments, including the one in (A), confirming that the accumulation of CTNNB1 in response to WNT/CTNNB1 pathway activation is comparable between HAP1^{WT} and HAP1$^{SGFP2\text{-}CTNNB1}$ cells. Horizontal bar indicates the mean. C) Graph depicting the results from a MegaTopflash dual luciferase reporter assay, showing comparable levels of TCF/LEF reporter gene activation for HAP1^{WT} and HAP1$^{SGFP2\text{-}CTNNB1}$ cells in response to CHIR99021 treatment. Data points from n=3 independent experiments are shown. Horizontal bar indicates the mean. Values are depicted relative to the DMSO control, which was set to 1 for each individual cell line. D) Graph depicting *AXIN2* mRNA induction in response to CHIR99021 treatment, demonstrating that induced expression of an endogenous target gene is comparable between HAP1^{WT} and HAP1$^{SGFP2\text{-}CTNNB1}$ cells. Data points represent n=3 independent experiments. Horizontal bar represents the mean. *HPRT* was used as a reference gene. Values are depicted relative to the HAP1^{WT} DMSO control, which was set to 1. E) Representative confocal microscopy images of the three HAP1$^{SGFP2\text{-}CTNNB1}$ clones after 4-hour vehicle control or 100ng/ml WNT3A treatment from n=1 biological experiment, revealing intracellular accumulation of SGFP2-CTNNB1 (green). Nuclei were counterstained with SiR-DNA dye (magenta). Scale bar is 10µm.

The following figure supplements are available for Figure 2:

Figure supplement 1: Verification of the WNT/CTNNB1 responsiveness of HAP1 cells.

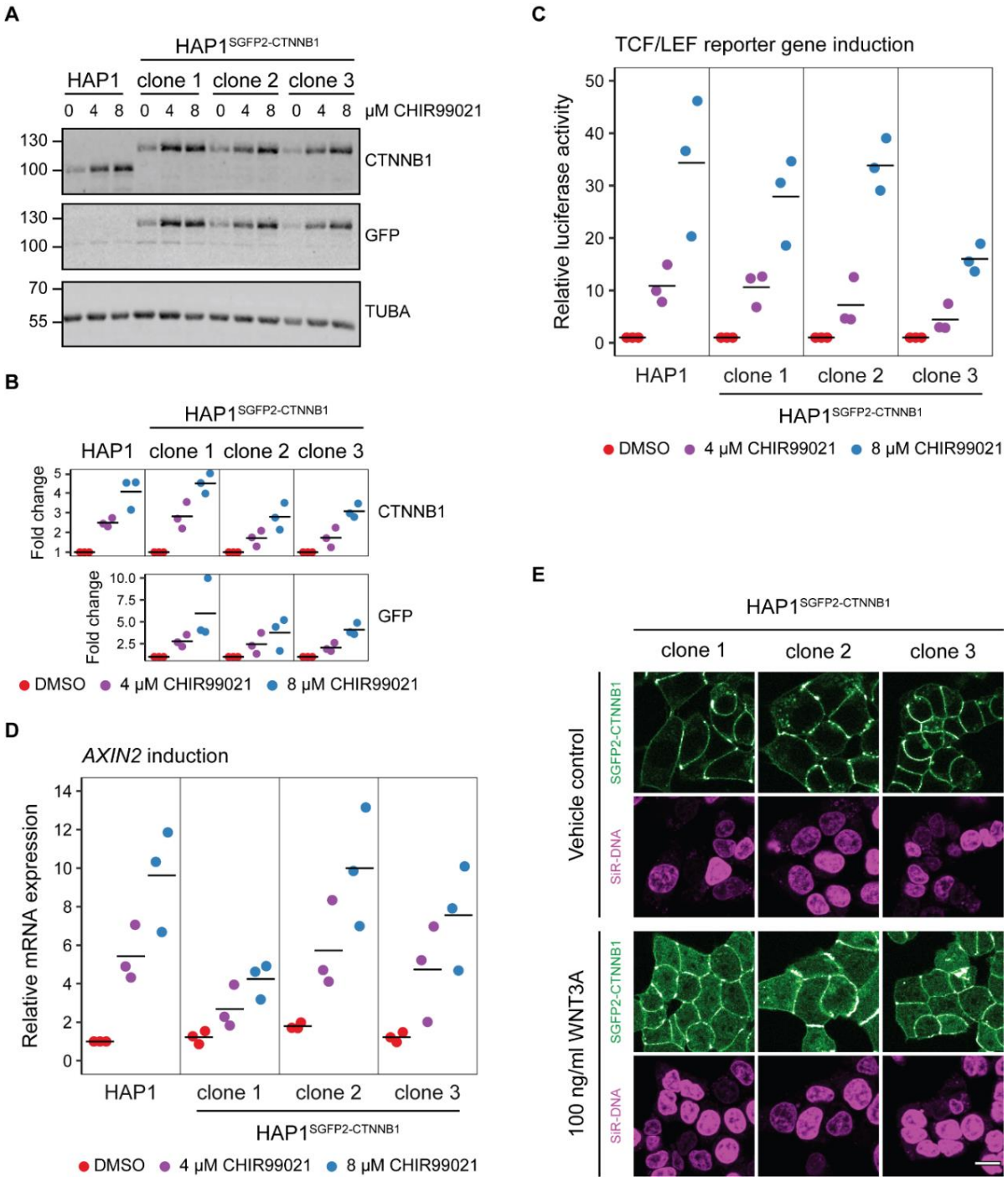

Live imaging of endogenous SGFP2-CTNNB1 during WNT pathway activation

To better understand the temporal dynamics of endogenous CTNNB1 stabilization, we performed live-cell imaging over 12 hours in HAP1$^{SGFP2\text{-}CTNNB1}$ cells (Figure 3, Supplementary Movie 1-2) with different levels of WNT stimulation. Unstimulated cells showed a stable CTNNB1 signal at the cell membrane throughout the imaging time course (Figure 3A,

Supplementary Movie 1). The membrane localization of CTNNB1 is consistent with its structural role in adherens junctions (Valenta et al., 2012; Yap et al., 1997), which we will not consider further in the current study. Stimulation with different concentrations of purified WNT3A resulted in a heterogeneous response pattern, with some cells in the population showing a far more prominent increase in CTNNB1 levels in the cytoplasm and nucleus than others (Figure 3A, Figure 3 supplement 2A-B, Supplementary Movie 2).

To quantify these dynamic changes, we developed a custom-built automated segmentation pipeline in CellProfiler™ (Figure 3D). Quantification showed that the dynamics of CTNNB1 accumulation were independent of the dose of WNT3A (Figure 3B-C, Supplementary Movies 4-5). Treatment with 100 ng/ml WNT3A increased SGFP2-CTNNB1 fluorescence 1.74-fold (mean, 95% CI 1.73-1.76) in the cytoplasm and 3.00-fold (mean, 95% CI 2.97-3.03) in the nucleus, with similar results in the other two HAP1$^{SGFP2\text{-}CTNNB1}$ clones (Figure 3 supplement 1).

Our quantification further shows that nuclear accumulation of CTNNB1 is favored over cytoplasmic increase (compare the fold-changes in Figure 3B-C). Moreover, the first statistically significant increases in fluorescence intensity in the cytoplasm could be detected after ~45 minutes of treatment (Supplementary Movie 4, Figure 3 supplement 2C), whereas in the nucleus an increase was first statistically significant after ~30 minutes (Supplementary Movie 5, Figure 3 supplement 2D). To examine the relation between the cytoplasmic and nuclear CTNNB1 pools more closely, we calculated the ratio between nuclear and cytoplasmic intensities of SGFP2-CTNNB1 (Figure 3D, Supplementary Movie 6). In untreated cells, the nuclear/cytoplasmic ratio was 0.652 (mean [3-5 hours], 95% CI 0.649-0.657), showing that SGFP2-CTNNB1 was preferentially localized to the cytoplasm (Figure 3D, Figure 3 supplement 3). For the first 3 hours after WNT3A, nuclear CTNNB1 levels rose considerably faster than

204 cytoplasmic CTNNB1 levels until the nuclear/cytoplasmic ratio showed a slight nuclear
205 enrichment of 1.08 (mean [3-5 hours] 95% CI 1.07-1.10) for 100 ng/ml WNT3A. This indicates
206 that not only the turn-over, but also the subcellular localization of CTNNB1 is actively
207 regulated both before and after WNT pathway activation.

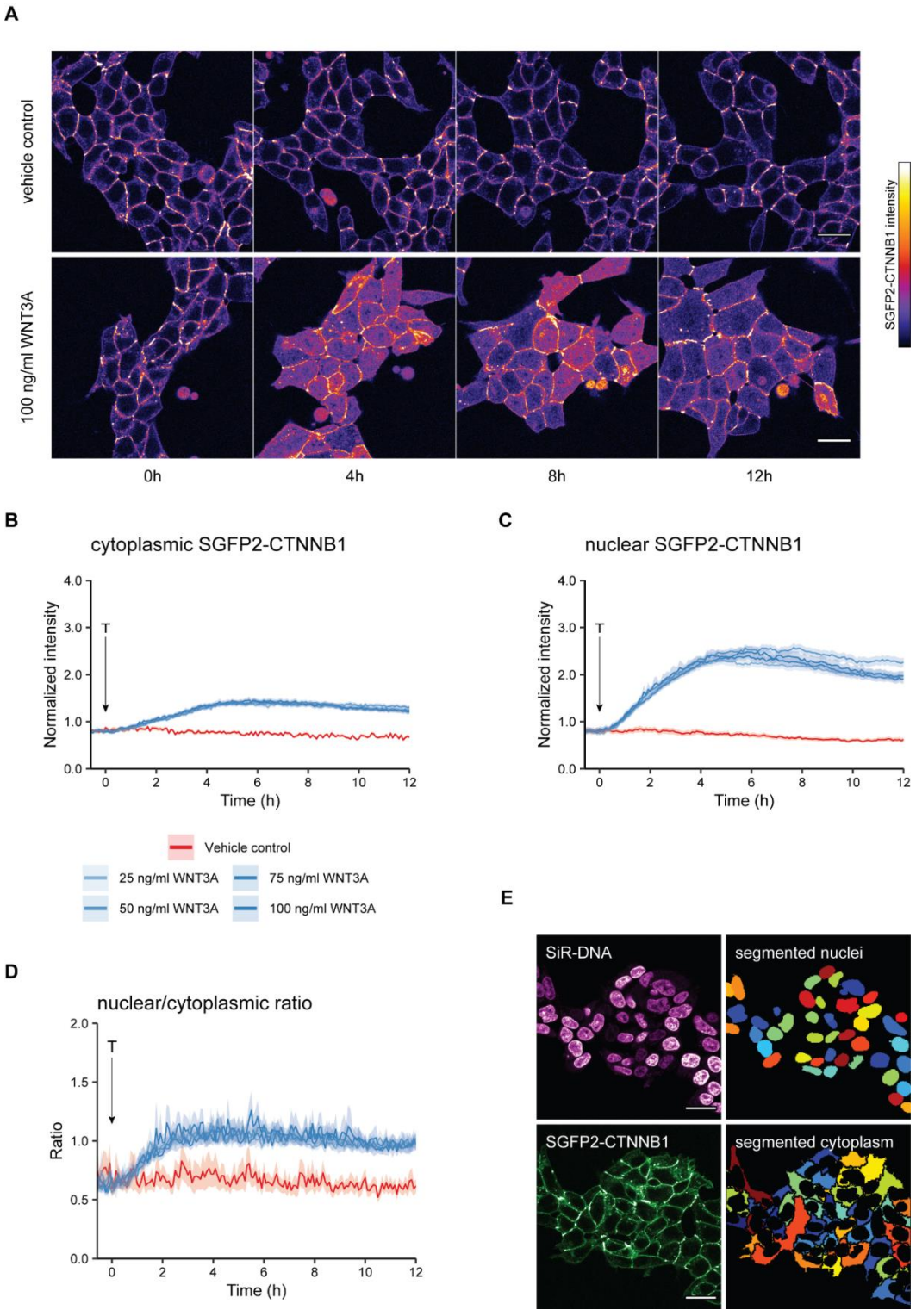

208

Figure 3: Live imaging of HAP1SGFP2-CTNNB1. A) Representative stills from confocal time-lapse experiments corresponding to Supplementary Movies 1-2, showing an increase of SGFP2-CTNNB1 after treatment with 100 ng/ml WNT3A (bottom) relative to a vehicle control (BSA) treated sample (top). Scale bar = 20 µm. B-D) Quantification of time-lapse microscopy series, using the segmentation pipeline shown in (E). Arrow indicates the moment of starting the different treatments (T, see legend in B for details). B-C) Graph depicting the normalized intensity of SGFP2-CTNNB1 in the cytoplasm (B) or nucleus (C) over time. Solid lines represent the mean normalized fluorescence intensity and shading indicates the 95% confidence interval. n=155-393 cells for each condition and time point, pooled data from n=3 independent biological experiments. D) Graph depicting the nuclear/cytoplasmic ratio of SGFP2-CTNNB1 over time, calculated from raw intensity values underlying (B) and (C). E) Segmentation of nuclei (top) and cytoplasm (bottom) based in the SiR-DNA signal and SGFP2-CTNNB1 signal. Scale bar = 20µm.

The following figure supplements are available for Figure 3:
Figure supplement 1: Verification of imaging results with WNT3A three independent HAP1$^{SGFP2\text{-}CTNNB1}$ clones.
Figure supplement 2: Difference analysis of SGFP2-CTNNB1 fluorescence.
Figure supplement3: Unnormalized nuclear and cytoplasmic intensity measurements

Establishing a fitting model for SGFP2-CTNNB1 diffusion

Having measured the relative changes in the cytoplasmic and nuclear levels of CTNNB1 in response to WNT3A stimulation, we next sought to exploit our experimental system to quantify additional molecular properties of CTNNB1 in each of these subcellular compartments using Fluorescence Correlation Spectroscopy (FCS). FCS is a powerful method to measure the mobility and absolute levels of fluorescent particles in a nanomolar range, compatible with typical levels of signaling proteins in a cell (reviewed in Hink, 2014). It has for instance been used to gain insight into the assembly of DVL3 supramolecular complexes (Yokoyama et al., 2012), the endogenous concentrations and mobility of nuclear complexes (Holzmann et al., 2019; Lam et al., 2012), and most recently, to quantify ligand-receptor binding reactions in the WNT pathway (Eckert et al., 2020). In point FCS, the fluorescence intensity is measured in a single point (Figure 4A,D-E). Diffusion of labeled particles, in this case SGFP2-CTNNB1, causes fluctuation of the fluorescence signal over time (Figure 4B). By correlating the fluorescence intensity signal to itself over increasing time-intervals, an autocorrelation curve is generated (Figure 4C). To extract relevant biophysical parameters, such as mobility (a measure for size) and the absolute numbers of the fluorescent particles (corresponding to their concentration), this autocorrelation curve is fitted with an appropriate model.

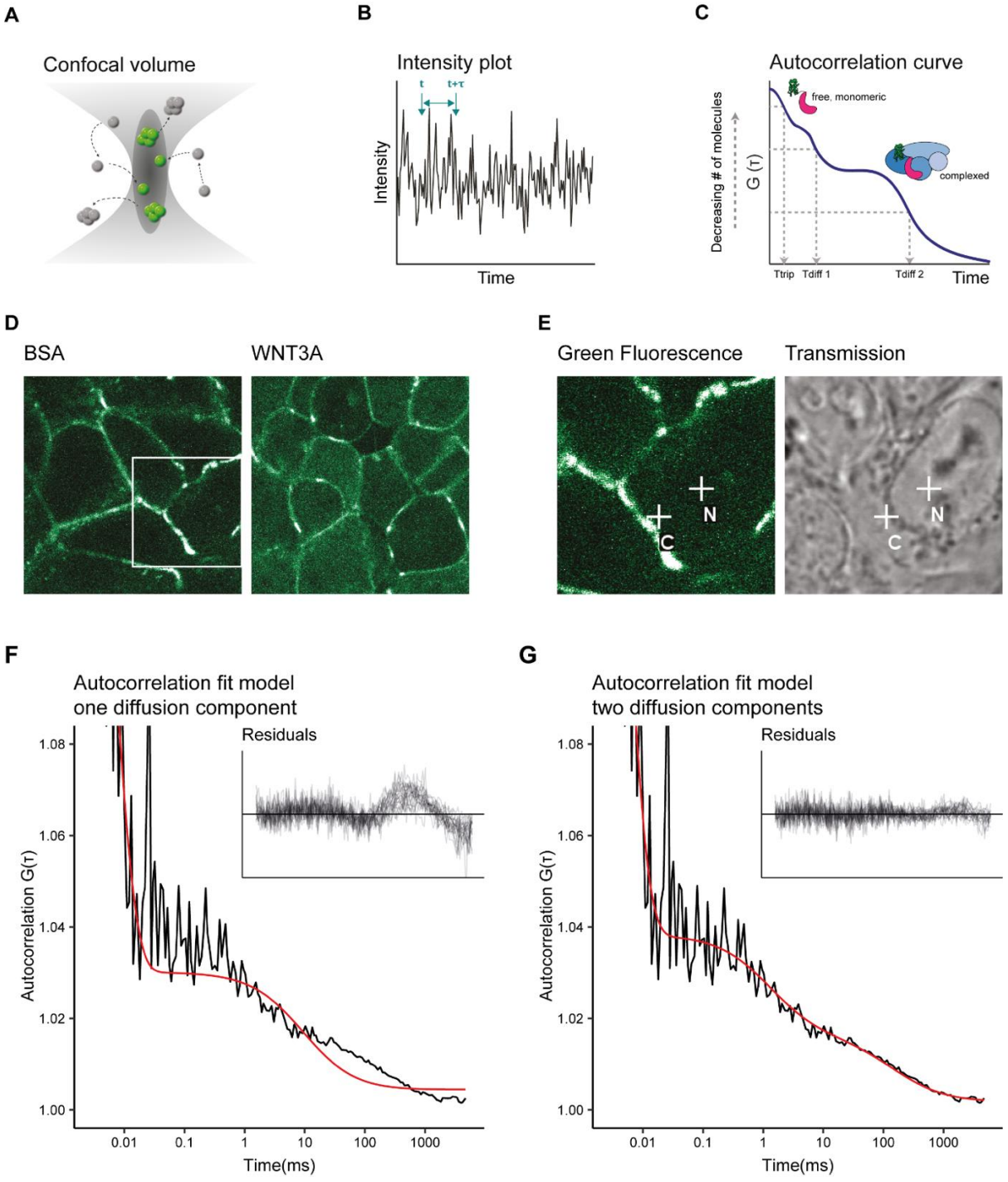

Figure 4: Two diffusion-component fit-model for SGFP2-CTNNB1 FCS measurements. A) Schematic representation of the point FCS technique, depicting the confocal volume with fluorescent particles diffusing in and out. Particles in FCS are defined by their coherent movement; therefore, a particle can be made up of monomers or multimers in isolation or complexed to unlabeled molecules. B) Schematic representation of intensity fluctuations over time as measured in the confocal volume. Fluctuations are the result of both photo-physics (e.g. blinking of the fluorophore) and diffusion. C) Graphical representation of the two diffusion-component fitting model used for our autocorrelation curves. T_{trip} describes the blinking of the SGFP2 fluorophore and the after-pulsing artefact. T_{diff1} and T_{diff2} describe the monomeric and complexed form of SGFP2-CTNNB1, respectively. Details of all fitting parameters are described in Materials and Methods. D) Representative confocal images of $HAP1^{SGFP2\text{-}CTNNB1}$ cells treated for 4 hours with BSA (left) or 100 ng/ml WNT3A (right). E) Zoom in of the white rectangle in (D), with representative locations of FCS measurement points for cytoplasm (C) and nucleus (N) indicated with white crosses in the SGFP2-CTNNB1 channel and transmission channel. F-G) Fitting of a representative autocorrelation curve with one unfixed diffusion-component (F) or a two diffusion-component model (G), where the first diffusion component was fixed to the speed of free monomeric SGFP2-CTNNB1 (14.9$\mu m^2/s$) and the second diffusion component was unfixed. The black line represents the autocorrelation curve generated from the FCS measurement, the red line represents the fitted model. The residuals after fitting of 25 individual curves are shown in the upper right corner of the graphs.

We first attempted to fit the autocorrelation curves obtained with point FCS measurements of HAP1$^{SGFP2\text{-}CTNNB1}$ cells with a one-component model (i.e. containing one single diffusion speed for SGFP2-CTNNB1). This model was unable to fit most of our data (Figure 4F). The current literature suggests that while a large portion of CTNNB1 is present as a monomer (Gottardi and Gumbiner, 2004; Maher et al., 2010), CTNNB1 is also present in multiprotein complexes in the cytoplasm and in the nucleus (reviewed in Gammons and Bienz, 2018). Therefore, we next used a model with two diffusion components, in which the first diffusion component was fixed to the diffusion speed of monomeric, unbound SGFP2-CTNNB1 (14.9 $\mu m^2/s$) and the second diffusion component was limited to slower speeds compatible with point-FCS imaging (see materials and methods for details). This model provided good fits for our autocorrelation curves obtained in both cytoplasmic and nuclear point FCS measurements (Figure 4G), consistent with the presence of free monomeric CTNNB1 and larger CTNNB1 containing complexes in both the nucleus and cytoplasm.

Quantification of absolute SGFP2-CTNNB1 concentrations

Using this fitting model, we determined, for the first time, the absolute concentrations of endogenous CTNNB1 in living cells in presence and absence of a physiological WNT stimulus (Figure 5A). In the absence of WNT3A, we determined the total concentration of SGFP2-CTNNB1 to be 180 nM (median, 95%CI 127-218) in the cytoplasm and 122 nM (median, 95%CI 91-158) in the nucleus. This is consistent with the nuclear exclusion we observed with confocal imaging (Figure 3).

In the presence of WNT3A, we measured a 1.2-fold increase in the total SGFP2-CTNNB1 concentration to 221 nM (median, 95%CI 144-250 nM) in the cytoplasm. This increase was smaller than expected from fluorescence intensity measurements (Figure 3B), for which we

currently have no explanation (Figure 5 supplement 1). In the nucleus the concentration increased 2.0-fold to 240 nM (median, 95%CI 217-325) upon pathway activation. Nuclear concentrations of SGFP2-CTNNB1 therefore exceed cytoplasmic concentrations after WNT3A treatment, consistent with the nuclear accumulation observed with live imaging (Figure 3). These concentrations are in a similar range as those previously determined by quantitative mass spectrometry in different mammalian cell lines (Kitazawa et al., 2017; Tan et al., 2012). Of note, the exact concentrations can vary between cell types and may be dependent on the intricacies and assumptions that underlie each individual technique.

Table 1: Total number of SGFP2-CTNNB1 molecules and calculated concentrations obtained from FCS measurements in n=3 independent experiments. The concentration is calculated from the number of molecules and the calibrated confocal volume (see material and methods). The number of molecules is consistent with those measured with N&B analysis (Figure 5 supplement 1A, Supplementary file 1)

			Number of molecules		Concentration (nM)	
compartment	treatment	n	median	95% CI	median	95% CI
Cytoplasm	BSA	21	80	70-116	180	127-218
	WNT3A	21	95	85-122	221	144-250
Nucleus	BSA	21	63	53-72	122	91-158
	WNT3A	18	135	127-150	240	217-325

Our two-component fitting model also allowed us to discriminate between pools of SGFP2-CTNNB1 with different mobility, i.e. fast diffusing monomeric CTNNB1 (Figure 5B) and slow diffusing complexed CTNNB1 (Figure 5C). In the nucleus, the concentration of fast moving CTNNB1 increased 2.0-fold from 87 nM (median, 95%CI 78-119) to 170 nM (median, 95%CI 147-214), while slow moving CTNNB1 concentration increased 3.9-fold from 22 nM (median, 95%CI 4-40) to 86 nM (median, 95%CI 67-114). This is also reflected by the increase in the bound fraction of SGFP2-CTNNB1 the nucleus (Figure 5D). The preferential increase of the slow-moving fraction is consistent with the notion that upon WNT stimulation CTNNB1 will become associated with the chromatin in a TCF dependent transcriptional complex (or “WNT enhanceosome”).

Table 2: Number and concentration of SGFP2-CTNNB1 molecules with the fast or slow diffusion coefficient obtained from FCS measurements in n=3 independent experiments. The concentration is calculated from the number of molecules and the calibrated confocal volume (see material and methods).

			Fast SGFP2-CTNNB1				Slow SGFP2-CTNNB1			
			Number of molecules		Concentration (nM)		Number of molecules		Concentration (nM)	
compartment	treatment	n	median	95% CI	median	95% CI	median	95% CI	median	95% CI
Cytoplasm	BSA	21	51	40-63	91	66-139	29	20-37	57	38-76
	WNT3A	21	60	47-80	145	76-168	35	30-41	68.	57-76
Nucleus	BSA	21	48	41-66	87	78-119	13	2-22	22	4-40
	WNT3A	18	96	81-101	170	147-214	47	37-49	86	64-104

Of note, in the cytoplasm, the concentration of both fast and slow SGFP2-CTNNB1 increased upon WNT3A treatment (Figure 5B-C), with the fraction of bound SGFP2-CTNNB1 remaining equal between stimulated (median 0.38, 95%CI 0.29-0.46) and unstimulated cells (median 0.34, 95%CI 0.31-0.4) (Figure 5D). The fact that a large portion of CTNNB1 remains in a complex after WNT stimulation, challenges the view that mainly monomeric CTNNB1 accumulates, as commonly depicted in the textbook model (Figure 1A).

Figure 5: Abundance and mobility of SGFP2-CTNNB1 molecules in living cells after 4 hours WNT3A treatment or control. Details on sample size and statistics can be found in supplementary file 1. A) Graph depicting the total concentration of SGFP2-CTNNB1 particles (monomeric plus complexed) as measured with FCS. B) Graph depicting the concentration of SGFP2-CTNNB1 particles with the fast diffusion component (i.e. free monomeric). C) Graph depicting the concentration of SGFP2-CTNNB1 containing particles with the slow diffusion component (i.e. complex associated).D-E) Graphs depicting the fraction (D) and speed (E) of the second diffusion component (i.e. SGFP2-CTNNB1 containing complex) measured by FCS. F) Example of typical regions of interest in two cells used in N&B analysis. Solid line represents the analysis ROI, dashed line, marks the outline of the nuclear envelope. G) Schematic representation of a confocal volume with different brightness species. On the left are 6 monomers with a brightness of 1, on the right 2 trimers with a brightness of 3, both result in a fluorescence of 6. N&B analysis is able to extract the number and the brightness of such samples, for more detail see supplement 1 of this figure. H) Graph depicting the molecular brightness of SGFP2-CTNNB1 in the cytoplasm and nucleus relative to controls as measured with N&B in the same subcellular compartments. EGFP monomer was used for normalization and EGFP dimer as a control for N&B measurements.
The following supplements are available for Figure 6:
Figure supplement 1: Quantification of SGFP2-CTNNB1 particles, fluorescence and fluorescence lifetime.
Figure supplement 2: Number and Brightness analysis
Supplementary File 1: Lists all summary statistics (mean, median, 95% confidence intervals, differences, p-values) of the FCS and N&B parameters show in Figure 6 and Figure 6 supplement 1.

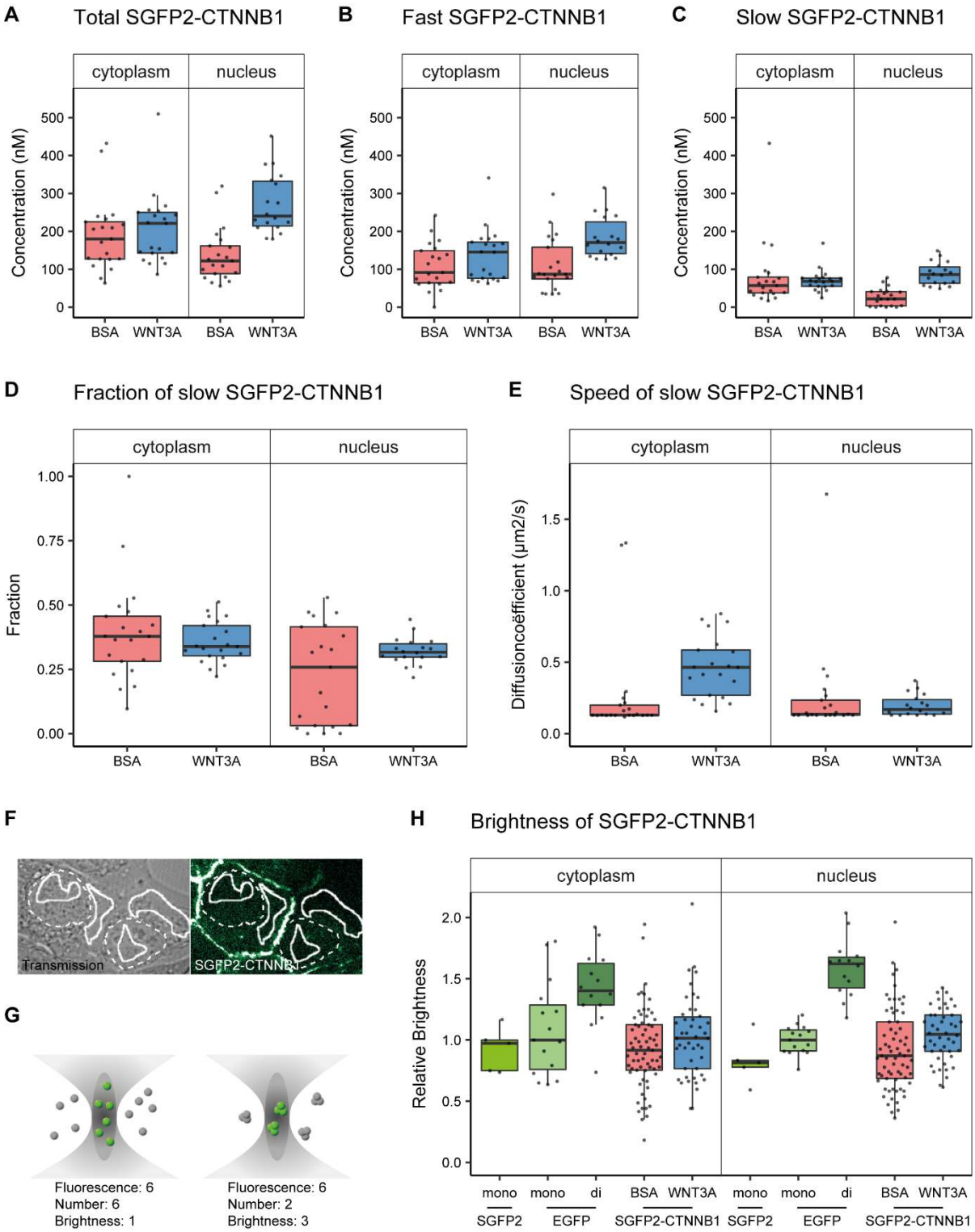

326

Quantification of SGFP2-CTNNB1 mobility

While we cannot determine the exact composition of the SGFP2-CTNNB1 complex, we do obtain biophysical parameters that are linked to its size. For instance, the diffusion coefficient of the nuclear SGFP2-CTNNB1 complex was 0.17 $\mu m^2 s^{-1}$, (median, 95%CI 0.14-0.22) in cells treated with purified WNT3A (Figure 5E). This is comparable to the diffusion coefficients measured for other chromatin bound transcriptional activators (Lam et al., 2012), which further supports that this pool represents the WNT enhanceosome.

In the cytoplasm, we determined the second diffusion coefficient of SGFP2-CTNNB1 to be 0.13 $\mu m^2 s^{-1}$ (median, 95% CI 0.13-0.17) in the absence of WNT3A stimulation (Figure 5E). This is indicative of very large complexes containing SGFP2-CTNNB1 that move with diffusion kinetics comparable to those previously observed for the 26S proteasome (Pack et al., 2014). After WNT3A treatment, the speed of the cytoplasmic complex increased 3.5-fold to 0.46 $\mu m^2 s^{-1}$ (95% CI of the median 0.37-0.57). Because a 3.5-fold change in speed would result in 3.5^3-change in size for a spherical particle (assuming Einstein-Stokes, see equation 7 in the material and methods section for details), this indicates that the size of the cytoplasmic CTNNB1 complex drastically changes when the WNT pathway is activated. Thus, although the fraction of CTNNB1 that resides in a complex remains the same, the identity of the cytoplasmic complex is quite different in unstimulated and WNT3A stimulated cells.

Determining the multimerization status of SGFP2-CTNNB1

Recent work suggests that the CTNNB1 destruction complex (also known as the "degradosome") is a large and multivalent complex, mainly as the result of AXIN and APC multimerization (reviewed in Schaefer and Peifer, 2019). The second diffusion coefficient, determined by our FCS measurements (Figure 5E), is consistent with this model. Such a large, multivalent destruction complex would be expected to have multiple CTNNB1 binding sites. To measure the multimerization status (i.e. the number of bound SGFP2-CTNNB1 molecules) within this cytoplasmic complex, we performed Number and Brightness (N&B) analysis (Figure 5F-G, Figure 5 supplement 2). N&B is a fluorescence fluctuation spectroscopy technique similar to point FCS, but it makes use of image stacks acquired over time rather than individual point measurements (Digman et al., 2008). By quantifying the variance in fluorescence intensity of this stack, not only the number of particles but also their brightness can be determined. The number of particles we determined using N&B, were highly similar to those obtained with FCS (compare Figure 5 supplement 1A with Table 1).

Because brightness is an inherent property of a fluorophore, a change in brightness is a measure of the number of fluorophores per particle. In our case, the brightness is indicative of the number of SGFP2-CTNNB1 molecules per complex. As N&B does not incorporate diffusion kinetics, we cannot differentiate between monomeric (which would have a brightness of one) and complexed CTNNB1 (which would have a brightness exceeding one if multiple CTNNB1 molecules reside in a single complex). Therefore, the measured brightness of SGFP2-CTNNB1 in our N&B analysis is an average of both fractions. We observe that the total pool of SGFP2-CTNNB1 in both the cytoplasm and nucleus has a brightness similar to EGFP and SGFP2 monomers (Figure 5H, Table 3). Because we found a large fraction of SGFP2-

CTNNB1 to reside in a complex using point FCS (Figure 5C-D), this suggests that few, if any, of these complexes contain multiple SGFP2-CTNNB1 molecules. If the cytoplasmic SGFP2-CTNNB1 containing complex indeed represents a large, multivalent destruction complex, this would imply that under physiological conditions, quite unexpectedly, most CTNNB1 binding sites are unoccupied in both the absence and presence of WNT3A.

Table 3: Brightness of SGFP2-compared relative to EGFP-monomer and -dimer controls in n=2 independent experiments. P-values were calculated using PlotsOfDifferences that uses a randomization test (Goedhart, 2019).Note that only the EGFP-dimer is significantly different to the EGFP-monomer control, while SGFP2-CTNNB1 is not.

Fluorophore	Compartment	Treatment	n	median	95CI median	P-value to matched control (EGFP monomer in the nucleus or cytoplasm)
EGFP-monomer	Cytoplasm	NA	15	1	0.79 - 1.34	1.000
EGFP-dimer	Cytoplasm	NA	14	1.4	1.29 - 1.60	0.011*
SGFP2-CTNNB1	Cytoplasm	BSA	69	0.92	0.83 – 1.00	0.738
SGFP2-CTNNB1	Cytoplasm	100ng/ml WNT3A	46	1.01	0.93 - 1.11	0.919
EGFP-monomer	Nucleus	NA	15	1	0.91 - 1.07	1.000
EGFP-dimer	Nucleus	NA	14	1.62	1.44 - 1.69	<0.001*
SGFP2-CTNNB1	Nucleus	BSA	69	0.87	0.78 - 0.96	0.192
SGFP2-CTNNB1	Nucleus	100ng/ml WNT3A	46	1.05	0.95 - 1.15	0.578

A minimal computational model of WNT/CTNNB1 signaling

Quantitative measurements and physical parameters of WNT pathway components and their interactions remain limited (Kitazawa et al., 2017; Lee et al., 2003; Tan et al., 2012), especially in living cells. As we obtained measurements of different functional pools of CTNNB1, we next sought to integrate these biophysical parameters in a minimal computational model of WNT signaling to identify the critical nodes of regulation of subcellular SGFP2-CTNNB1 distribution (Figure 6A, Table 4-5, Materials and Methods). This minimal model is based on a previous model of Kirschner and colleagues (Lee et al., 2003), and incorporates the new data obtained in our study, supplemented with parameters from the literature (Lee et al., 2003; Tan et al., 2012).

Our model diverges from the model presented by Lee et al. on two major points. First, the model is simplified by replacing the details of the destruction complex formation cycle and

the individual actions of APC and AXIN with a single, fully formed destruction complex. We chose this option because our study does not provide new quantitative data on the formation and dynamics of the destruction complex, but does provide absolute concentrations of CTNNB1 that is in a bound state in the cytoplasm. Second, we explicitly include shuttling of CTNNB1 between the cytoplasm and nucleus in both directions (Schmitz et al., 2013; Tan et al., 2014).

Thus, our model (Figure 6A) describes the binding of cytoplasmic CTNNB1 ('CB') to the destruction complex ('DC') leading to its phosphorylation and degradation (described by k3), which releases the DC. Transport of CTNNB1 from the cytoplasm to the nucleus, allows nuclear CTNNB1 ('NB') to bind to TCF forming a transcriptional complex (NB-TCF). When WNT is present in the system, we describe the inactivation of the destruction complex ('DC*') by DVL. The model is available as interactive app at https://wntlab.shinyapps.io/WNT_minimal_model/ and allows users to explore the effects of modulating different equilibria and constants in an intuitive way.

Our model faithfully recapitulates the dynamic changes that we observe with functional imaging (compare Figure 6B-F to Figure 3 and 5). Moreover, it reveals two critical regulatory nodes in addition to the requisite inactivation of the destruction complex (described by k5/k4). The first additional node of regulation is nuclear import and export (or 'shuttling', described by k6/k7). Upon WNT stimulation, the ratio of k6/k7 needs to increase in order for the model to match the free CTNNB1 concentrations we measured by FCS (Table 5, Figure 5B). Thus, the balance shifts from nuclear export before WNT, to nuclear import after WNT. The second additional node of regulation is the association of CTNNB1 with the TCF transcriptional complex (or 'retention'), described by k9/k8. Upon WNT stimulation, the ratio

of k9/k8 needs to decrease by almost a factor of 10 in order for the model to reproduce the concentrations of free and bound CTNNB1 in the nucleus as measured by FCS (Table 5, Figure 6F, Figure 5B-C). Thus, association of CTNNB1 to the TCF transcriptional complex is favored after WNT stimulation.

In summary, our model suggests that WNT/CTNNB1 signaling is regulated at three distinct levels of the signal transduction pathway: destruction complex inactivation, nucleocytoplasmic shuttling and nuclear retention.

Table 4: Variables Minimal Model of WNT signaling.

Model name	Variable	Compound	Values obtained from	WNT OFF (nM)	WNT ON (nM)
CB	x_1	Free cytoplasmic CTNNB1	FCS data this report	91	145
DC	x_2	Free destruction complex	Model equations	82.4	52
CB*-DC	x_3	DC-bound phosphorylated CTNNB1	FCS data this report*	62.5*	62.5*
DC*	x_4	Inactivated destruction complex	Model equations	0	30.5
NB	x_5	Free nuclear CTNNB1	FCS data this report	87	170
TCF	x_6	Free TCF	Model equations	81	17
NB-TCF	x_7	TCF-bound nuclear CTNNB1	FCS data this report	22.2	86
TCF^0	TCF^0	Total TCF	x_7 and Tan et al., 2012 - Figure 11	103	103

Under the assumption that k3 does not change, the levels of CB-DC remain equal. Since there was no significant difference between the concentration of slow SGFP2-CTNNB1 (Table 2) the average of both medians was used

Table 5: Equilibrium conditions for the Minimal Model of WNT signaling. All rates are multiplied with factor R=20, so that the equilibrium is reached at 4.5h according to Figure 4 C, D.

Rate constant		Biological process	Values based on	WNT OFF	WNT ON
b	$nMmin^{-1}$	CTNNB1 synthesis	v_{12} from Lee	0.423	0.423
$\frac{k_2}{k_1}$	nM	Binding to and phosphorylation by the destruction complex of cytoplasmic CTNNB1	K_8 from Lee	120	120
k_3	min^{-1}	Dissociation and degradation of phosphorylated CTNNB1 from the destruction complex	Deduced from b and x_3	0.0068	0.0068
$\frac{k_5}{k_4}$	nM	Inactivation of the destruction complex by activated DVL	Fitted to x_1 and x_7	N.A.	1.7
$\frac{k_6}{k_7}$		Ratio between nuclear import and export of CTNNB1	Deduced from x_1 and x_5	0.96	1.17
$\frac{k_9}{k_8}$	nM	Dissociation of nuclear CTNNB1 from TCF	Deduced from x_5, TCF^0, x_7	320	33.6

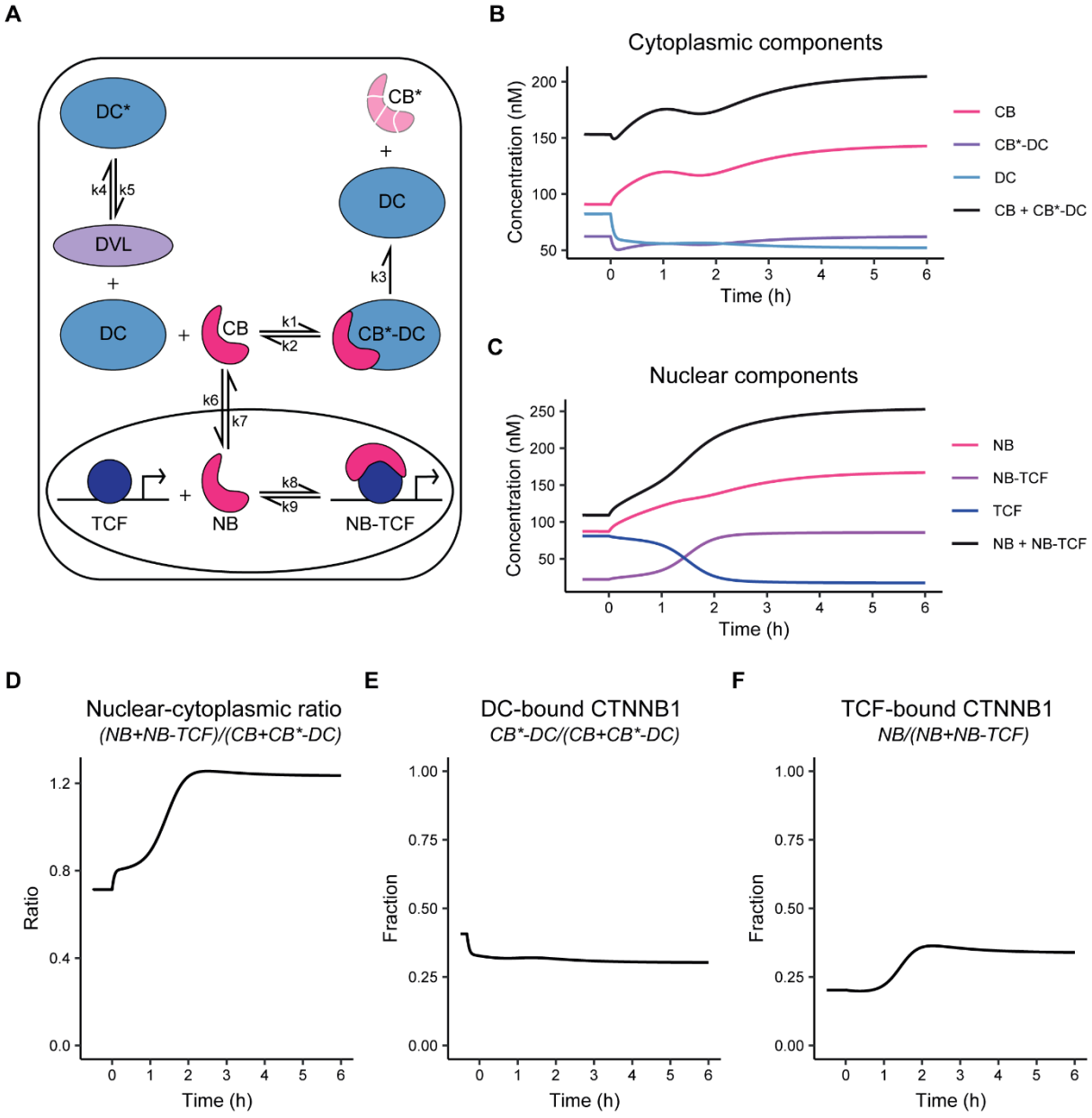

Figure 6: Computational model of WNT/CTNNB1 based on FCS concentrations for free and complexed CTNNB1 (Table 1-2). A) Schematic overview of the model. DC=destruction complex, DC*= DVL-inactivated DC, CB=cytoplasmic CTNNB1, CB*=phosphorylated CB, NB=nuclear CTNNB1, TCF=TCF/LEF transcription factors, DVL=WNT-activated DVL. The model assumes that there is no activated DVL in the absence of WNT, therefore k5/k4 do not play any role in the WNT 'OFF' equilibrium. Note that CB* is degraded and therefore plays no role in the model. B) Graph depicting the modelled concentrations of cytoplasmic components over time. The black line indicates total concentration of cytoplasmic CTNNB1, corresponding to Figure 4C. C) Graph depicting the modelled concentrations of nuclear components over time. The black line indicates total concentration of nuclear CTNNB1, corresponding to Figure 4D. D) Graph depicting the ratio of total nuclear and cytoplasmic CTNNB1 over time, corresponding to the measurements in 4E. E) Graph depicting the DC-bound CTNNB1 fraction ratio over time. F) Graph depicting the TCF-bound CTNNB1 fraction ratio over time.

Perturbing the system to mimic oncogenic WNT signaling

WNT signaling is often disrupted in cancer (reviewed in Polakis, 2000; Zhan, Rindtorff, & Boutros, 2017), in many cases due to inactivating mutations of negative regulators or activating mutations in CTNNB1 itself (Bugter et al., 2020). One of the earliest identified mutations in CTNNB1 was a substitution of serine-45 for a phenylalanine (S45F) (Morin et al., 1997). This mutation removes the CSNK1 priming phosphorylation site on CTNNB1 that is needed for sequential phosphorylation by GSK3, and thus blocks its proteasomal degradation (Amit et al., 2002; Liu et al., 2002).

We generated the S45F mutation in one of our HAP1$^{SGFP2\text{-}CTNNB1}$ cell lines through a second step of CRISPR/Cas9 mediated genome editing (Fig 7 supplement 1A-D). As expected, the mutation resulted in higher CTNNB1 levels (Figure 7 supplement 1E-F) and constitutive downstream activation of the pathway (Figure 7 supplement 1G-H). Next, we used this cell line for two purposes. First, we used FCS and N&B to compare the complex-state of wild-type and mutant CTNNB1 in the cytoplasm (Figure 7). Second, we reproduced the same perturbation in silico to strengthen the link between our experimental data and the computational model (Figure 8).

Similar to the situation detected under physiological conditions (Figure 5D), we find a large fraction of SGFP2-CTNNB1^{S45F} to reside in a cytoplasmic complex (Figure 7A). As observed for physiological stimulation with WNT3A (Figure 5E), the speed of this complex is increased in SGFP2-CTNNB1^{S45F} compared to unstimulated HAP1$^{SGFP2\text{-}CTNNB1}$ cells (Figure 7B). We find similar behavior when we block the GSK3 mediated phosphorylation of wild-type CTNNB1 using CHIR99021 (Figure 7C-D). The reduction in cytoplasmic complex size therefore must occur downstream of CTNNB1 phosphorylation. Intriguingly, our N&B analyses suggest that

these smaller S45F mutant cytoplasmic complexes have a higher occupancy of CTNNB1 (Figure 7E) than the those in WNT3A (Figure 5H) or CHIR99021 (Figure 7F) stimulated wildtype cells. The S45F mutant (median 1.304, 95% CI 1.139-1.418, p=0.002) was significantly brighter than the SGFP2 monomer control (median 0.866, 95% CI 0.573 - 0.949), where the WT tagged HAP1 cells again did not diverge from the monomer (0.886, 95% CI 0.722-1, p=0.845) (Supplementary file 1).

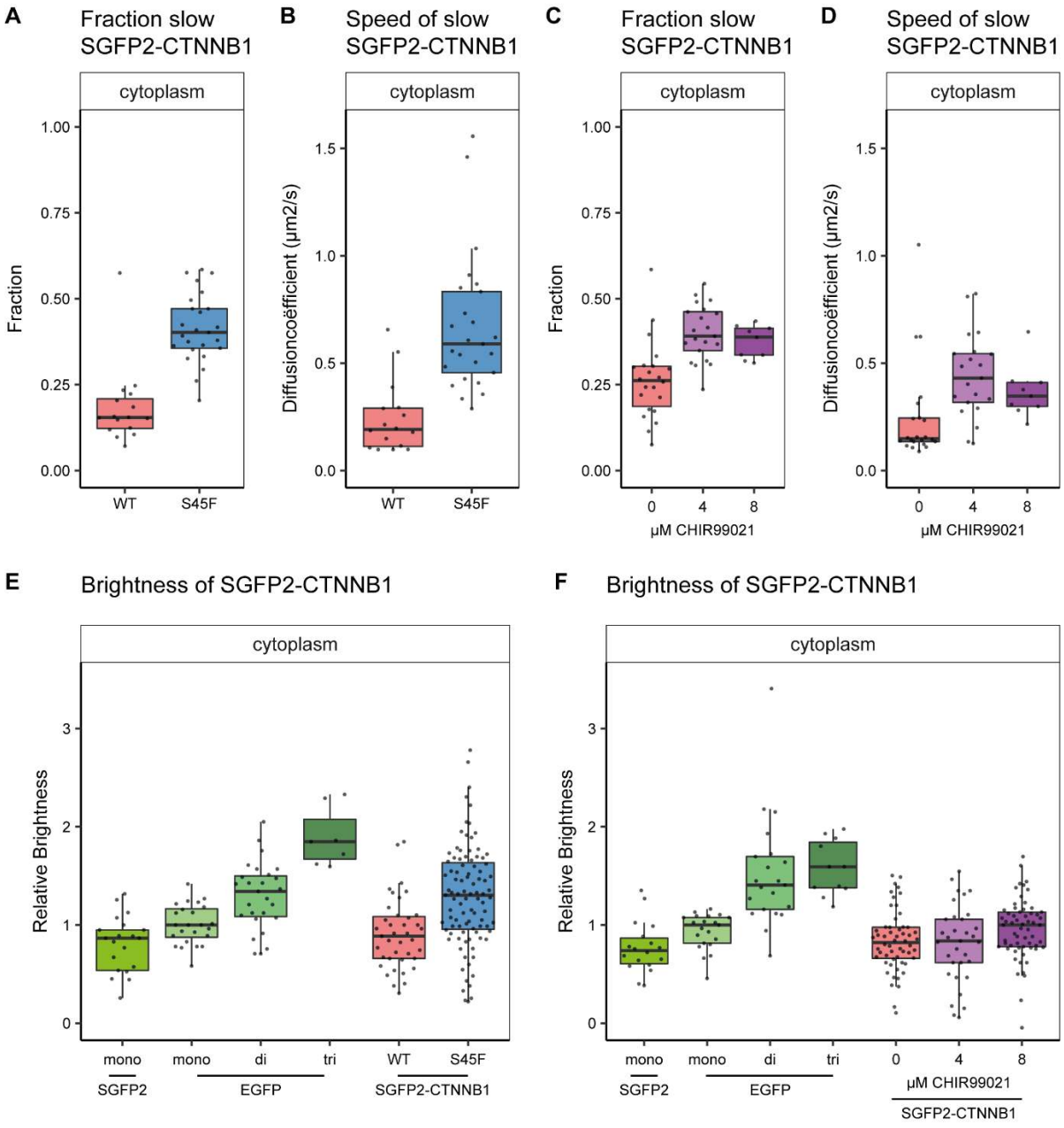

Figure7 Cytoplasmic complex characteristics in absence of SGFP2-CTNNB1 N-terminal phosphorylation. The S45F mutant was introduced using CRISPR (see Figure 7 supplement 1) and CHIR treated and control cells were measured after 24 hours. Details on sample size and statistics can be found in supplementary file 1. A) Graph depicting the fraction of particles with the second diffusion component (i.e. SGFP2-CTNNB1 containing complex) measured by FCS for S45F mutant B) Graph depicting the speed of the second diffusion component (i.e. SGFP2-CTNNB1 containing complex) measured by FCS for S45F mutant. C).Graph depicting the fraction of particles with the second diffusion component (i.e. SGFP2-CTNNB1 containing complex) measured by FCS after 24h treatment with CHIR99021 C) Graphs depicting the speed of the second diffusion component (i.e. SGFP2-CTNNB1 containing complex) measured by FCS after 24h treatment with CHIR99021 .E-F) Graphs depicting the molecular brightness of SGFP2-CTNNB1 in the cytoplasm and nucleus relative to controls as measured with N&B in the same subcellular compartments for S45F mutant CTNNB1 (E) or after 24 hours of CHIR99021 treatment (F). EGFP monomer was used for normalization and EGFP dimer and trimer as controls for N&B measurements.
The following supplements are available for Figure 7:
Figure 7 supplement 1: Generation and characterization of a S45F mutant cell line (HAP1$^{SGFP2\text{-}CTNNB1(S45F)}$)

The S45F mutant shows a substantial increase in SGFP2-CTNNB1 levels in the cytoplasm and nucleus (Figure 8A). As this constitutive mutation does not provide any kinetic information, we also measured the dynamic response of SGFP2-CTNNB1 to CHIR99021-mediated GSK3 inhibition (Figure 8 supplement 1, Supplementary movie 3). We see similar initial kinetics as for WNT3A stimulation. However, in contrast to what is observed for WNT3A treatment, no plateau was reached at the highest concentration of CHIR99021 (8 µM). The fact that intracellular SGFP2-CTNNB1 levels in the 8 µM CHIR99021 condition continued to accumulate, suggests that negative feedback, for example through AXIN2 (Lustig et al., 2002) or through internalization of receptor complexes (Agajanian et al., 2019), is overridden under these circumstances. Of note, the quantification also confirms that there is cell to cell heterogeneity in the response, regardless of whether WNT/CTNNB1 signaling is activated at the level of the receptor (WNT3A treatment) or at the level of the destruction complex (CHIR99021 treatment), as can be seen from the spread of intensities measured from individual cells (Figure 3 Supplement 2A-B).

Finally, we compared our biological measurements from these perturbation experiments to our computational model predictions. Both the S45F mutation and CHIR99021 treatment disrupt one of the critical nodes in the model, namely the degradation of phosphorylated CTNNB1 (corresponding to k3, Figure 6A). With FCS and N&B we quantified the accumulation of CTNNB1 levels of mutant SGFP2-CTNNB1^{S45F} (Figure 8B, Figure 8 supplement 2A) and wild-

type SGFP2-CTNNB1 upon CHIR99021 treatment (Figure 8 supplement 2B-C). Both exceeded the levels observed with physiological WNT3A stimulation (Figure 3A-C, Figure 5A). In our computational model we simulated reduced degradation by lowering the value of k3. A reduction in k3 from its initial value (k3=0.0068, Table 5) to k3=0.0043, accurately predicted the higher cytoplasmic concentration measured for the S45F mutant (Figure 8C), but a further reduction of k3=0.0038 was needed to match the measured nuclear concentration (Figure 8D). However, reducing k3 alone was not sufficient to reproduce either the fraction of CTNNB1 that is bound in the nucleus (Figure 8E-G) or the overall nuclear enrichment of CTNNB1 (Figure 8H). The latter requires a predicted nuclear/cytoplasmic (N/C) ratio greater than one, as observed in both physiological and constitutively active WNT/CTNNB1 signaling (Figure 8I-K).

The increase in the bound fraction of SGFP2-CTNNB1 in the nucleus was comparable between our mutant cell line (Figure 8E), CHIR99021 (Figure 8F) and WNT3A (Figure 5D) treatment. To match this experimental observation, we adjusted the k9/k8 ratio as was also required for physiological WNT3A signaling (Table 5, Figure 8G). This shows the importance of this regulatory node not only in physiological, but also in oncogenic signaling. At the same time, the adjustment of k9/k8 on top of k3 still does not predict the observed nuclear enrichment of CTNNB1 (Figure 8H). After changing the nuclear shuttling ratio k6/k7 to the ratio we fitted for the WNT ON situation (Table 5), the model now also reproduces the nuclear enrichment of CTNNB1 (Figure 8L). In figures 8M-N, we show that the changes in parameters k6/k7 and k9/k8 have little effect on the CTNNB1 concentration in the cytoplasm, but do substantially affect the nuclear concentrations of CTNNB1. This suggest that processes downstream of CTNNB1 degradation play a significant and active role in the CTNNB1 dynamics of the cell.

Taken together, our computational model can describe both physiological and oncogenic signaling. Moreover, it underlines the importance of CTNNB1 regulation downstream of destruction complex activity and confirms a critical role for nuclear import and nuclear retention.

Figure 8: In silico and experimental perturbation of WNT signaling. Details on experimental sample size and statistics can be found in supplementary file 1. A) Representative confocal images of HAP1-SGFP2WT (WT, top) and HAP1-SGFP2S45F (S45F, bottom) cells acquired with the same image settings. The S45F mutation leads to the accumulation and nuclear enrichment of CTNNB1 in the cell. B) Graph depicting the total concentration of SGFP2-CTNNB1 particles (monomeric plus complexed) as measured with FCS. C-D) Inhibition of CTNNB1 degradation is modelled as a reduction in the value of k3. C) Graph depicting the predicted total cytoplasmic CTNNB1 concentration as a function of k3. A reduction in k3 from 0.0068 (Table 5, WNT ON and WNT OFF conditions) to ~0.0043 (dotted line) corresponds to the cytoplasmic concentration observed (solid line). D) Graph depicting the predicted total nuclear CTNNB1 concentration as a function of k3. The solid horizontal line indicates the concentration measured for the S45F mutant by FCS. Note that the value of k3 that matches the observed cytoplasm concentration (dotted line) does not match the experimentally determined concentration in the nucleus (solid line). E-F) Graphs depicting the fraction of particles with the second diffusion component (i.e. SGFP2-CTNNB1 containing complex) measured by FCS for wild-type and S45F mutant (E) and after 24-hour CHIR99021 treatment (F). The increase in the bound fraction in the oncogenic mutant or after GSK3 inhibition we find, is comparable to what we observed in WNT3A stimulated cells (Figure 5D). G) Graph showing the predicted nuclear bound fraction of CTNNB1as a function of k3 with the TCF/CTNNB1 binding affinity of the model (Table 4) for WNT OFF (k9/k8 =320, pink line) and for WNT ON (k9/k8=33.5, blue line). Note that for WNT ON, the value for the nuclear bound fraction approximates the experimentally determined slow fraction for the S45F mutant (solid line, panel E) at the value for k3 that matches the cytoplasmic concentration of CTNNB1 (dotted line). H) Graph showing the predicted nuclear/cytoplasmic (N/C)-ratio as a function of k3 with TCF/CTNNB1 binding affinity of the model (Table 4) for WNT OFF (k9/k8=320, pink line) and WNT ON (k9/k8=33.5, blue line). Note that, although for WNT ON the value of the N/C-ratio increases with k3, there is still nuclear exclusion (N/C-ratio lower than 1, dashed line) at the value of k3 that matches the cytoplasmic CTNNB1-concentration (dotted line). I-K) The N/C-ratio as measured by FCS for wild-type and S45F mutant (I), after 24-hour CHIR99021 treatment (J) and after 4 hour WNT3A treatment (K). Note that all perturbations lead to nuclear accumulation (N/C-value exceeding 1). L) Graph showing the predicted N/C-ratio as a function of k3 with the WNT ON value for k9/k8 with the nuclear shuttling ratio of the model (k6/k7 Table 4),corresponding to WNT OFF (k6/k7=0.96, pink line) and WNT ON (k6/k7=1.17, blue line), respectively. Note that the WNT ON value of k6/k7 increases the N/C-ratio to nuclear accumulation at the value for k3 that matches the cytoplasmic concentration (dotted line). M) Graph depicting the predicted total cytoplasmic CTNNB1 concentration as a function of k3 with WNT ON and WNT OFF values for k9/k8 and k6/k7Note that modulation of k9/k8 and k6/k7 has no effect on the predicted cytoplasmic concentration of CTNNB1. The horizontal solid line is the experimentally determined cytoplasmic CTBNN1 concentration (cf. panel B); the vertical dotted line is at the value of k3 that best reproduces this experimental finding in the model. N) Graph depicting the predicted total nuclear CTNNB1 concentration as a function of k3 for WNT ON and WNT OFF values for k9/k8 and k6/k7. Note that if both k9/k8 and k6/7 are changed from their WNT OFF values the predicted nuclear concentration of CTBNN1 better matches the experimentally determined concentration (horizontal solid line) at the value for k3 that matches the cytoplasm concentration (vertical dotted line).

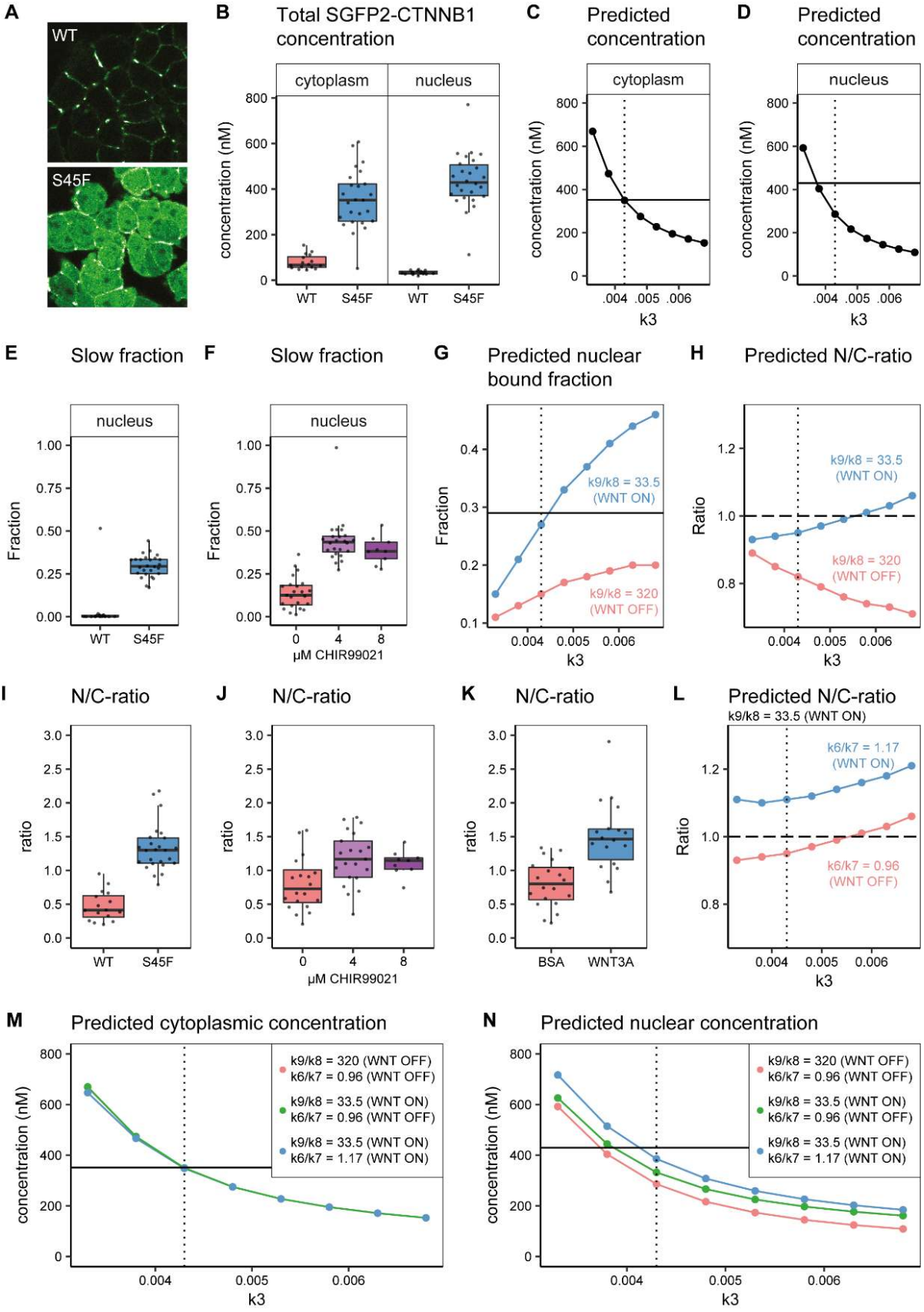

552

Discussion

WNT signaling is critical for tissue development and homeostasis. Although most core players and many of their molecular interactions have been uncovered, dynamic spatiotemporal information with sufficient subcellular resolution remains limited. As both genome editing approaches and quantitative live-cell microscopy have advanced further, the goal of studying WNT/CTNNB1 signaling at endogenous expression levels in living cells now is within reach. Maintaining endogenous expression levels is important, as overexpression may lead to altered stoichiometry of signaling components, as well as changes in subcellular localization (Gibson et al., 2013; Mahen et al., 2014). Indeed, it has been shown that exogenously expressed CTNNB1 is less signaling competent, probably due to its post-translational modification status (Hendriksen et al., 2008). Here we generated functional HAP1$^{SGFP2\text{-}CTNNB1}$ knock-in cell lines to study the dynamic behavior and subcellular complex state of endogenous CTNNB1 in individual living human cells in both a physiological and oncogenic context.

Using live-cell microscopy and automated cell segmentation, we observe that endogenous CTNNB1 only increases 1.7-fold in the cytoplasm and 3.0-fold in the nucleus after WNT3A treatment, which is consistent with the literature (Jacobsen et al., 2016; Kafri et al., 2016; Massey et al., 2019).

Next, we used state-of-the-art, quantitative microscopy to measure the absolute concentration of CTNNB1 within different subcellular compartments and in different complex-states in living cells. The findings from these experiments challenge the dogma that mainly monomeric CTNNB1 accumulates upon WNT pathway stimulation. Moreover, our integrative approach of quantitative imaging and computational modelling revealed three

576 critical nodes of CTNNB1 regulation, namely CTNNB1 degradation, nuclear shuttling and
577 nuclear retention, which together describe the CTNNB1 turnover, subcellular localization and
578 complex status under both physiological and oncogenic conditions.

579 Cytoplasmic regulation of CTNNB1

580 Using FCS, we determined that in unstimulated HAP1 cells a substantial fraction of SGFP2-
581 CTNNB1 is associated with a very large, slow-diffusing cytoplasmic complex (Figure 4-5). The
582 main known cytoplasmic complex containing CTNNB1 is the destruction complex. The
583 combined weight of the individual destruction complex components (AXIN, APC, CSNK1 and
584 GSK3) would be expected to result in a much higher mobility than that displayed by the
585 cytoplasmic CTNNB1-containing complex we observed. However, evidence is growing that
586 the destruction complex forms large phase separated aggregates (also termed biomolecular
587 condensates) (reviewed in Schaefer and Peifer, 2019). Oligomerization of AXIN and APC
588 underlies the formation of these aggregates, and this in turn appears to be required for
589 efficient degradation of CTNNB1 (Fiedler et al., 2011; Kunttas-Tatli et al., 2014; Pronobis et
590 al., 2017; Spink et al., 2000). There is some evidence that these aggregates form at (near)
591 endogenous levels (Fagotto et al., 1999; Faux et al., 2008; Mendoza-Topaz et al., 2011;
592 Pronobis et al., 2015; Schaefer et al., 2018; Thorvaldsen et al., 2015), but it is still an open
593 question what the exact composition and size of the destruction complex is in a physiological
594 context. It should be noted that our imaging does not visualize such aggregates (Figure 3A).
595 In addition, our N&B data indicate that few, if any, complexes exist that contain multiple
596 SGFP2-CTNNB1 molecules in the absence or presence of WNT3A stimulation – something that
597 would be expected in biomolecular condensates formed by the oligomerization of CTNNB1
598 binding partners. Only following the introduction of an S45F mutation, which results in

599 constitutive inhibition of CTNNB1 phosphorylation and degradation, we observe a brightness
600 increase that would be compatible with the accumulation of multiple SGFP2-CTNNB1^{S45F}
601 molecules in a single cytoplasmic complex. This indicates that while the destruction complex
602 might be multivalent in both a physiological and an oncogenic context, CTNNB1 occupancy of
603 the complex is low under physiological conditions, but increased in oncogenic signaling. This
604 has major impacts on how we conceptualize the workings of the CTNNB1 destruction
605 machinery – especially in the context of cancer, since mutations in CTNNB1 (affecting
606 occupancy) may have very different biochemical consequences than mutations in APC
607 (affecting multimerization and valency of the destruction complex itself).

608 The mechanism on destruction complex deactivation remains controversial (Tortelote et al.,
609 2017; Verkaar et al., 2012). The current literature suggests that the destruction complex is
610 sequestered to the FZD-LRP receptor complex upon WNT pathway stimulation. Several
611 models exist for how the membrane sequestration inhibits CTNNB1 degradation, including
612 LRP mediated GSK3 inhibition (Stamos et al., 2014), sequestration of GSK3 in multi vesicular
613 bodies (Taelman et al., 2010), (partial) dissociation of the destruction complex (Liu et al.,
614 2005; Tran and Polakis, 2012), and saturation of CTNNB1 within an intact destruction complex
615 (Li et al., 2012). Our data clearly show that a substantial fraction of CTNNB1 in the cytoplasm
616 remains bound upon pathway stimulation (Figure 5D). This is not predicted by any of the
617 above mentioned models and challenges the long-held view that mainly monomeric CTNNB1
618 accumulates.

619 Additionally, we show that the cytoplasmic CTNNB1 complex in WNT3A or CHIR99021 treated
620 cells as well as in S45F mutant cells has an increased mobility compared to control cells (Figure
621 5E). Therefore, while the diffusion coefficient is still very low (indicating a very large complex),

this implies it is a vastly different complex than that observed in the absence of WNT stimulation. The fact that cells in which GSK3 phosphorylation is inhibited through S45F mutation or CHIR99021 treatment show similar behavior, suggests that the size of the cytoplasmic complex is directly linked to the phosphorylation status of CTNNB1. The destruction complex has been shown to associate with (parts of) the ubiquitin and proteasome machinery (Li et al., 2012; Lui et al., 2011; Schaefer et al., 2020). One interesting possibility, therefore, is that phosphorylated CTNNB1 is required for coupling the destruction complex to the ubiquitination and proteasome machinery. In fact, although not explicitly mentioned in the main text, supplementary table 1 of Li et al., 2012 shows that in HEK293 cells, which harbor no mutation in the core components of the WNT pathway, CTNNB1 was found to interact with subunits of the proteasome, whereas in the S45F-CTNNB1 mutant cell line Ls174T these interactions were not detected. In conclusion, although we do not directly determine its identity, our measured biophysical parameters of the cytoplasmic CTNNB1 complex are consistent with it representing a large, multivalent destruction complex that is coupled to the proteasome as long as CTNNB1 is being phosphorylated.

Nuclear regulation of CTNNB1

The key function of CTNNB1 downstream of WNT is to regulate transcription of TCF/LEF target genes (Doumpas et al., 2019; Schuijers et al., 2014). Proteomic analyses have shown that the WNT enhanceosome consists of CTNNB1, TCF/LEF, PYGO and BCL9 and several other large proteins (Fiedler et al., 2015; van Tienen et al., 2017). Using FCS, we showed that CTNNB1 resides in a nuclear complex with a diffusion coefficient that is compatible with such a DNA-bound transcriptional complex (Figure 5E) (Lam et al., 2012).

Although CTNNB1 is known to associate with TCF/LEF factors in response to WNT/CTNNB1 signaling to drive transcription (Franz et al., 2017; Schuijers et al., 2014), we also detect low levels of nuclear CTNNB1 complex in the absence of a WNT stimulus (Figure 5C). The diffusion coefficient of the nuclear CTNNB1 complex does not change upon the addition of WNT3A (Figure 5E), suggesting that some CTNNB1 is already associated with the DNA even in the absence of a WNT stimulus. At this point, we cannot exclude the contribution of TCF/LEF independent DNA binding (Armstrong et al., 2012; Essers et al., 2005; Kormish et al., 2010), or anomalous subdiffusion in the nucleus, either due to physical obstruction , transient DNA-binding events protein or protein complex formation (Dross et al., 2009; Kaur et al., 2013; Wachsmuth et al., 2000), as FCS only allows us to probe the speed of this complex.

However, upon pathway activation through WNT3A, CHIR99021 or S45F mutation we see a consistent increase in the fraction and absolute levels of this slow-diffusing nuclear CTNNB1 complex (Figure 5E, Figure 8E-F), compatible with increased CTNNB1 binding to its target sites. For WNT stimulation, we measured that the concentration of bound SGFP2-CTNNB1 in the nucleus increased to a 89 nM, which corresponds to something in the order of 20,000 bound CTNNB1 molecules in one nucleus, assuming a small nuclear volume of 0.36 pL (Tan et al., 2012). Published CHIPseq studies report many CTNNB1 DNA binding sites, ranging from several hundred to several thousand sites in mammalian cells (Cantù et al., 2018; Doumpas et al., 2019; Schuijers et al., 2014). It is therefore highly likely that at least part of the slow-diffusing CTNNB1 particles we measure indeed represents CTNNB1 that is associated with the WNT enhanceosome.

Regulation of CTNNB1 nuclear accumulation

In HAP1 cells, endogenous CTNNB1 is excluded from the nucleus in the absence of WNT. Our live imaging data reveal an immediate and preferential increase in nuclear CTNNB1 upon WNT3A stimulation, until an equilibrium is reached between the cytoplasmic and nuclear levels (Figure 3D). This is consistent with previous observations in HEK293 cells stably overexpressing low levels of YFP-CTNNB1 (Kafri et al., 2016).

Intriguingly, CTNNB1 does not contain nuclear import or export signals and can translocate independently of classical importin and exporter pathways (Fagotto et al., 1998; Wiechens and Fagotto, 2001; Yokoya et al., 1999). Hence, the molecular mechanism of CTNNB1 subcellular distribution remains incompletely understood. Evidence from Fluorescence Recovery After Photobleaching (FRAP) studies suggest that the increase in nuclear CTNNB1 is due to changes in binding to its interaction partners in the cytoplasm and nucleus (retention) rather than active changes in nuclear import and export rates (shuttling) (Jamieson et al., 2011; Krieghoff et al., 2006). We argue that the two are not mutually exclusive, as our experimental data and computational model show that WNT regulates both nucleocytoplasmic shuttling and nuclear retention of CTNNB1. Indeed, we see an increase of nuclear CTNNB1 complexes in the nucleus (Figure 5C-D) and the dissociation of CTNNB1 from TCF is reduced almost 10-fold in WNT signaling conditions in our computational model (Table 5). Our model predicts that this increased nuclear retention indeed also increases the nuclear/cytoplasmic ratio (Figure 8H). However, to reconcile our computational prediction with our experimental observations we additionally need to include a shift from nuclear export to nuclear import upon pathway activation (Figure 6, Figure 8). Our integrated experimental biology and computational modelling approach thus reveals that WNT signaling

not only regulates the absolute levels of CTNNB1 through destruction complex inactivation, but also actively changes its subcellular distribution through nuclear retention and shuttling. The fact that direct inhibition of GSK3 mediated phosphorylation of CTNNB1 results in the same behavior, indicates that the phosphorylation status of CTNNB1 plays a critical role. This further emphasizes the importance of posttranslational modifications and conformational changes in CTNNB1 for its subcellular localization and function (Gottardi and Gumbiner, 2004; Sayat et al., 2008; Valenta et al., 2012; van der Wal and van Amerongen, 2020; Wu et al., 2008) .

Challenges and opportunities for fluorescence fluctuation spectroscopy techniques

Using fluorescence fluctuation spectroscopy techniques (FCS and N&B) we have quantified endogenous CTNNB1 concentrations and complexes in living cells for the first time, which provided novel and long-awaited biophysical parameters for computational modelling. Moreover, our approach has also yielded novel insights into CTNNB1 regulation that challenge current dogmas in the field. If we are correct, this has important consequences. First, if only part of the cytoplasmic CTNNB1 pool is uncomplexed (i.e. free or monomeric), regardless of whether the WNT/CTNNB1 pathway is off or on (either via physiological WNT3A stimulation or via oncogenic activation), this is a rewrite of the textbook model. Second, if the slow-diffusion cytoplasmic CTNNB1 complex indeed represents a proteasome-associated destruction complex, this would fuel a debate that has remained unresolved for many years (Li et al., 2012; Verkaar et al., 2012). As more studies will use these image-based techniques to determine biophysical properties of WNT/CTNNB1 signaling components (Ambrosi et al., 2020; Eckert et al., 2020), the field will undoubtedly learn how to interpret these findings.

As with any technique, there are several limitations to consider. First of all, for the determination of the absolute concentration by FCS it should be noted that a small portion of SGFP2-CTNNB1 could be in a non-fluorescent state. Although our FCS analysis model already accounts for dynamic dark states such as the triplet state, non-matured fluorophores could lead to a slight underestimation of our concentrations. However, this is expected to be a very small fraction as SGFP2 has very good maturation kinetics (Kremers et al., 2007). Secondly, our findings concerning the diffusion kinetics are limited by the assumptions we make in the FCS fitting model. Although obvious mistakes in underlying assumptions immediately become clear due to bad fitting results and can therefore be excluded, not every wrong assumption will stand out accordingly. Our data clearly shows that assuming only one diffusion speed for CTNNB1 in HAP1 cells would be incorrect (Figure 4). However, whether with the second diffusion speed we measure a single distinct, large complex, or rather an average of multiple different CTNNB1 containing complexes cannot be determined in our current set-up. In addition, we assume that CTNNB1 is present as a free-floating monomer (as fixed for our first component), based on previous observations (Gottardi and Gumbiner, 2004; Maher et al., 2010). However, at least one report suggests that CTNNB1 is not present as a monomer but rather in small cytoplasmic complexes of ~200 kDa (Gerlach et al., 2014). As diffusion speed is relatively insensitive to differences in size (e.g. an 8-fold increase in protein mass is expected to result in only a 2-fold reduction of the diffusion coefficient for a spherical particle), it is possible that we do not measure truly free-floating CTNNB1, but rather smaller complexes. In addition, point FCS is limited to a single position in the cell. Therefore, in addition to the intercellular differences in the WNT signaling response of individual cells, our measurements also sample intracellular heterogeneity caused by the presence of organelles and molecular crowding. Notwithstanding these limitations, we have been able to show that

a large portion of CTNNB1 is present in a very large complex in both stimulated and unstimulated conditions and that this complex has a statistically and biologically significant different speed after WNT3A treatment.

The biophysical parameters we obtained from point FCS and N&B have allowed us to learn more about the speed and occupancy of the SGFP2-CTNNB1 complexes in living cells. Moreover, using different stimuli and perturbations of the pathway we have been able to link this to the phosphorylation status of CTNNB1. However, FCS and N&B do not provide conclusive evidence on the identity and composition of these complexes. An exciting possibility would be to label additional components presumed to be present in the CTNNB1-containing complexes at the endogenous level to uncover the precise composition and stoichiometry of protein complexes involved in WNT signaling. For instance, Fluorescence Cross Correlation Spectroscopy (FCCS) could be employed to test if two proteins reside within the same complex (Elson, 2011; Hink, 2014; Macháň and Wohland, 2014). Ultimately, a combination of such quantitative functional imaging techniques, biochemical and proteomic approaches, together with additional perturbations will need to be employed to further our understanding of the dynamic composition of endogenous CTNNB1 complexes, as well as to help us resolve the molecular mechanism underlying nucleocytoplasmic shuttling and nuclear retention. As both genome editing and live cell imaging techniques continue to improve, additional possibilities will open up to address longstanding questions in cellular signaling in a physiological context with high spatial and temporal resolution. New opportunities and challenges await as these investigations extend to 3D organoid cultures, developing embryos and living organisms.

Material and Methods

DNA Constructs

The following constructs were used: pSpCas9(BB)-2A-Puro (PX459) V2.0 ((Ran et al., 2013), a kind gift from Feng Zhang, available from Addgene, plasmid #62988), MegaTopflash ((Hu et al., 2007), a kind gift from Dr. Christophe Fuerer and Dr. Roel Nusse, Stanford University), CMV Renilla (E2261,Promega, Madison, WI), pSGFP2-C1 ((Kremers et al., 2007), a kind gift from Dorus Gadella, available from Addgene, plasmid #22881), pmScarlet-i_C1 (Bindels et al., 2017), a kind gift from Dorus Gadella, available from Addgene, plasmid # 85044), pSYFP2-C1 ((Kremers et al., 2006),a kind gift from Dorus Gadella, available from Addgene, plasmid #22878), mTurquoise2-C1 ((Goedhart et al., 2012), a kind gift from Dorus Gadella, available from Addgene, plasmid # 54842), pEGFP (Clontech, Mountain View, CA), $pEGFP_2$ and $pEGFP_3$ ((Pack et al., 2006), a kind gift from Masataka Kinjo) and pBluescript II KS(+) (Stratagene, La Jolla, CA).

The gRNA targeting the start codon in exon2 of human *CTNNB1* was designed using the MIT webtool (crispr.mit.edu) and cloned into pX459. Oligos RVA567 and RVA568 (Table 6) encoding the gRNA were annealed, and ligated into BbsI-digested pX459 plasmid as previously described (Ran et al., 2013) to obtain pX459-CTNNB1-ATG. The gRNA targeting codon 3 of *CTNNB1* for mutagenesis of Serine 45 to Phenylalanine (S45F) was similarly designed and cloned by introducing RVA561 and RVA562 (Table 6) into pX459, yielding pX459-CTNNB1-S45.

The repair plasmid for SGFP2-CTNNB1 (pRepair-SGFP2-CTNNB1) was cloned using Gibson cloning (Gibson et al., 2009). First, a repair plasmid including the Kozak sequence from the pSGFP2-C1 plasmid was generated (pRepair-Kozak-SGFP2 -CTNNB1). For this, 5' and 3'

779 homology arms were PCR amplified from genomic HEK293A DNA with primers RVA618 and
780 RVA581 (5' arm) or RVA619 and RVA584 (3' arm). SGFP2 was amplified with Gibson cloning
781 from pSGFP2-C1 with primers RVA582 and RVA583 and the backbone was amplified from SacI
782 digested pBlueScript KS(+) with primers RVA622 and RVA623. The final repair construct
783 (pRepair-SGFP2-CTNNB1) contains the endogenous *CTNNB1* Kozak sequence before the
784 SGFP2 ATG. To obtain (pRepair-SGFP2-CTNNB1), the backbone and homology regions were
785 amplified from pRepair-SGFP2-Kozak-CTNNB1 with primers RVA1616 and RVA1619 and an
786 SGFP2 without the Kozak sequence was amplified from pSGFP2-C1 with primers RVA1617 and
787 RVA1618. To generate color variants of the repair plasmid SYFP2, mScarlet-i and mTurquoise2
788 were also amplified from their respective C1 vectors with primers RVA 1617 and RVA 1618.
789 PCR products were purified and assembled with a Gibson assembly master mix with a 1:3
790 (vector:insert) molar ratio. Gibson assembly master mix was either purchased (E2611S, NEB)
791 or homemade (final concentrations: 1x ISO buffer (100mM Tris-HCL pH 7.5, 10mM MgCl2,
792 0.2M dNTPs (R0181, Thermo Scientific), 10mM DTT (10792782, Fisher), 5% PEG-8000
793 (1546605, Sigma-Aldrich, St Louis, MO), 1mM NAD+ (B9007S, NEB)), 0.004 U/µl T5
794 exonuclease (M0363S, NEB), 0.5 U/µl Phusion DNA Polymerase (F-530L, Thermo Scientific)
795 and 4 U/µl Taq DNA ligase (M0208S, NEB)).

796 The following plasmids are available from Addgene: pX459-CTNNB1-ATG (#153429), pX459-
797 CTNNB1-S45 (#164587), pRepair-SGFP2-CTNNB1 (#153430), pRepair-mScI-CTNNB1
798 (#153431), pRepair-SYFP2-CTNNB1 (#153432), pRepair-mTq2-CTNNB1 (#153433)).

799

Primers used

Table 6: primers/oligonucleotides used in this study

RVA24	CAAGTTTGTTGTAGGATATGCCC
RVA25	CGATGTCAATAGGACTCCAGA
RVA124	AGTGTGAGGTCCACGGAAA
RVA125	CCGTCATGGACATGGAAT
RVA555	GCCAAACGCTGGACATTAGT
RVA558	AGACCATGAGGTCTGCGTTT
RVA561	CACCGTTGCCTTTACCACTCAGAGA
RVA 562	AAACTCTCTGAGTGGTAAAGGCAAC
RVA567	CACCGTGAGTAGCCATTGTCCACGC
RVA568	AAACGCGTGGACAATGGCTACTCAC
RVA581	tgctcaccatggtggGATTTTCAAAACAGTTGTATGGTATACTTC
RVA582	actgttttgaaaatcCCACCATGGTGAGCAAGGGC
RVA583	agtagccattgtccaCTTGTACAGCTCGTCCATGCCG
RVA584	gacgagctgtacaagTGGACAATGGCTACTCAAGGTTTG
RVA618	atacgactcactatagggcgaattggagctGATGCAGTTTTTTTCAATATTGC
RVA619	ttctagagcggccgccaccgcggtggagctCTCTCTTTTCTTCACCACAACATTTTATTTAAAC
RVA622	AAGAGAGAGCTCCACCGCGGTGGCGGCCG
RVA623	TGCATCAGCTCCAATTCGCCCTATAGTGAGTCG
RVA1616	tgtccacgctgGATTTTCAAAACAGTTGTATGG
RVA1617	atacaactgttttgaaaatccagcgtggacaATGGTGAGCAAGGGCGAG
RVA1618	cacaaaccttgagtagccatCTTGTACAGCTCGTCCATGC
RVA1619	ATGGCTACTCAAGGTTTGTGTCATTAAATC
RVA2540	CTTACCTGGACTCTGGAATCCATTCTGGTGCCACTACCACAGCTCCTTTCCTGTCCGGTAAAGGCAATCCTGAGGAAGA GGATGTGGATACCTCCCAAGT

Cell Culture, Treatment and Transfection

HAP1 cells (a kind gift from Thijn Brummelkamp, NKI) were maintained in full medium (colorless IMDM (21056023, Gibco, Thermo Fisher Scientific, Waltham, MA) supplemented with 10% FBS (10270106, Gibco) and 1X Glutamax (35050061, Gibco)) under 5% CO2 at 37°C in humidifying conditions and passaged every 2-3 days using 0.25% Trypsin-EDTA (25200056, Gibco). Cells were routinely tested for mycoplasma. We verified the haploid identity of the parental HAP1^{WT} by karyotyping of metaphase spreads. To maintain a haploid population, cells were resorted frequently (see below) and experiments were performed with low passage number cells.

Where indicated, cells were treated with CHIR99021 (6mM stock solution in DMSO) (1677-5, Biovision, Milpitas, CA) or Recombinant Mouse Wnt-3a (10µg/ml stock solution in 0.1% BSA in PBS) (1324-WN-002, R&D systems, Bio-Techne, Minneapolis, MN) with DMSO and 0.1% BSA in PBS as vehicle controls, respectively.

Cells were transfected using Turbofect (R0531, ThermoFisher, Thermo Fisher Scientific, Waltham, MA), X-tremeGene HP (6366546001, Roche, Basel, Switzerland) or Lipofectamine 3000 (Invitrogen, Thermo Fisher Scientific, Waltham, MA) in Opti-MEM (Gibco) according to the manufacturer's instructions.

HAP1$^{SGFP2\text{-}CTNNB1}$ and HAP1$^{SGFP2\text{-}CTNNB1(S45F)}$ generation

800.000 HAP1 cells/well were plated on 6-well plates. The following day, cells were transfected with Turbofect and 2000 ng DNA. pX459-CTNNB1-ATG and pRepair-SGFP2-CTNNB1 were transfected in a 2:1, 1:1 or 1:2 ratio. pSGFP2-C1, pX459 or pX459-CTNNB1-ATG were used as controls. From 24 to 48 hours after transfection cells were selected with 0.75 µg/ml puromycin (A1113803, Gibco). Next, cells were expanded and passaged as needed until FACS sorting at day 9. For FACS analysis and sorting cells were washed, trypsinized, resuspended with full medium and spun down at 1000 rpm for 4 minutes. For sorting, cells were stained with 1 µg/ml Dapi (D1306, Invitrogen) in HF (2 % FBS in HBSS (14175053, Gibco)), washed with HF and resuspended in HF. To determine the haploid population, a separate sample of cells was stained with 5 µM Vybrant® DyeCycleTM Violet Stain (V35003, Invitrogen) in full medium for 30 minutes and kept in vibrant containing medium. Cells were filtered with a 70 µm filter and then used for FACS sorting and analysis on a FACSARIA3 (BD, Franklin Lanes, NJ). Vybrant-stained cells were analyzed at 37° and used to set a size gate only containing haploid cells. Dapi-stained cells were single cell sorted at 4°C into 96-well plates, that were

previously coated overnight with 0.1 % gelatin (G9391, Sigma-Aldrich) in MQ and contained full medium supplemented with 1 % penicillin/streptomycin (15140122, Gibco) and 0.025 M HEPES (H3375 Sigma-Aldrich, 1 M stock solution, pH 7.4, filter sterilized). The 3 independent clones used in this study were obtained from separate transfections of the same parental cell line. Clones were genotyped and sanger sequenced using primers RVA555 and RVA558 (Table 6).

HAP1$^{SGFP2\text{-}CTNNB1(S45F)}$ were generated from HAP1$^{SGFP2\text{-}CTNNB1}$ clone 1. The same procedure as above was followed with slight adaptations; Cells were transfected 1000 ng pX459-CTNNB1-S45 or pX459 with 2 or 4 µl 10mM repair oligo (RVA 2540) with Turbofect, selected with puromycin and expanded as described above. Haploid single cells were sorted after 11 days as described above. For haploid size discrimination Vybrant™ DyeCycle™ Ruby Stain (V10273) was used. The 5 clones used in this study were obtained from 2 separate transfection (clone 2,3,16,24 from the same transfection, clone 27 from a second transfection). Clones were genotyped using primers RVA555 and RVA558 (Table 6), followed by HpaII (ER0511, ThermoFisher) restriction as per the manufacturer's instruction. RVA555 was used for sanger sequencing.

Resorting of the cell lines was also performed with the same FACS procedure, with collection of cells in 15 mL tubes containing full medium with 1 % penicillin and 0.025 M HEPES.

FACS data were analyzed and visualized with FlowJo™.

Luciferase Assay

For luciferase assays, 100.000 cells per well were seeded on a 24-well plate. Cells were transfected with 1µl X-tremeGene HP and 400 ng MegaTopflash reporter and 100 ng CMV-Renilla or 500 ng SGFP2-C1 as a negative control 24 hours later. Cells were treated with the

indicated concentration of CHIR99021 24 hours after transfection and after another 24 hours medium was removed and the cells were harvested with 50 µl Passive Lysis Buffer (E1941, Promega). Luciferase activity was measured on a GloMax Navigator (Promega) using 10µl lysate in a black OptiPlate 96-well plate (6005279, Perkin Elmer, Waltham, MA) and 50 µL homemade firefly and luciferase reagents (according to (Fuerer et al., 2014; Hampf and Gossen, 2006)).

For luciferase assays, three technical replicates (i.e. three wells transfected with the same transfection master mix) were pipetted and measured for each sample in each experiment. For each technical triplicate, the average MegaTopflash activity was calculated and depicted as a single dot in Figure 2C and Figure 7 supplement 1G. Three independent biological experiments, each thus depicted as an individual dot, were performed. To calculate MegaTopflash activity, Renilla and Luciferase luminescence values were corrected by subtracting the average background measured in the SGFP2-transfected control. MegaTopflash activity was calculated as the ratio of corrected Firefly and Renilla luminescence and normalized to the average reporter activity of the relative DMSO control.

Western Blot

The remaining lysates from the technical triplicates of the luciferase assay were combined and they were cleared by centrifugation for 10 minutes at 12.000 g at 4°C. Western blot analysis was performed and quantified as previously described (Jacobsen et al., 2016). Antibodies were used with the following dilutions, 1:1000 Non-phosphorylated (Active) β-catenin clone D13A1 (8814S, Cell Signaling, Danvers, MA), 1:2000 total β-catenin clone 14 (610153, BD), 1:1000 α-Tubulin clone DM1A (T9026, Sigma-Aldrich), 1:1000 GFP polyclonal (A-6455, Invitrogen), 1:20.000 IRDye 680LT Goat anti-Rabbit IgG (926-68021, LI-COR, Lincoln,

NE), 1:20.000 IRDye 800CW Donkey anti-Mouse IgG (926–32212, LI-COR). Raw data for all blots have been made available at https://osf.io/vkexg/.

qRT-PCR

For qRT-PCR analysis, 100.000 HAP1 cells per well were seeded on a 24-well plate. After 48 hours, cells were treated with indicated concentrations of CHIR99021. Cells were harvested 24 hours after treatment. RNA was isolated with Trizol (15596018, Invitrogen) according to the manufacturer's instructions. cDNA was synthesized using SuperScriptIV (18090010, Invitrogen) according to the manufacturer's instructions. qRT-PCR was performed with SyberGreen (10710004, Invitrogen). The endogenous WNT target gene *AXIN2* was amplified using primers RVA124 and RVA125, and HPRT housekeeping control was amplified using primers RVA24 and RVA25.

For qRT-PCR experiments, three technical replicates (i.e. three reactions with the same cDNA) were pipetted and measured for each sample in each experiment. For each technical triplicate, the mean fold-change in AXIN2 expression was calculated and depicted as a single dot in Figure 2D and Figure 7 supplement 1H. Three independent biological experiments, each thus depicted as an individual dot, were performed. Relative expression levels of *AXIN2* were calculated using the comparative Delta-Ct method (Livak and Schmittgen, 2001; Schmittgen and Livak, 2008). Briefly, *AXIN2* expression was normalized for *HPRT* expression and then the relative fold-change to a WT DMSO sample was calculated for all clones and conditions.

Time-lapse imaging

The day before imaging, 88.000 cells/well were seeded on an 8 well chamber slide with glass bottom (80827-90, Ibidi, Gräfelfing, Germany). HAP1$^{SGFP2\text{-}CTNNB1}$ clone 2 was used for the main Figure 3, all 3 clones were used for Figure 3 supplement 1. HAP1$^{SGFP2\text{-}CTNNB1(S45F)}$ clone 2 was

imaged for Figure 8A. Approximately 6 hours before imaging, medium was replaced with full medium supplemented with 1% penicillin/streptomycin, 0.025M HEPES and 500nM SiR-DNA (SC007, Spirochrome, Stein am Rhein, Switzerland). Time lapse experiments were performed on an SP8 confocal microscope (Leica Microsystems, Wetzlar, Germany) at 37°C with a HC PL APO CS2 63x/1.40 oil objective (15506350, Leica), 488 and 633 lasers, appropriate AOBS settings, using HyD detectors for fluorescent signal with a 496-555 for SGFP2-CTNNB1 and 643-764 bandpass for SiR-DNA, and a transmission PMT. Using multi-position acquisition, up to 24 images were captured every 5 minutes. Focus was maintained using AFC autofocus control on demand for every time point and position. Automated cell segmentation and intensity quantification was performed using a custom CellProfiler™ pipeline (made available at https://osf.io/6pmwf/). Output data was further analyzed in R/RStudio. Cells with a segmented cytoplasmic area of less than 10 pixels were excluded. Intensities were normalized per position to the average intensity in the cellular compartment (nucleus or cytoplasm) for that position before the addition of the compounds. The imaging settings resulted in low signal in regions not occupied by cells (~10% of the nuclear intensity, and ~5% of the cytoplasmic intensity in untreated cells), and the data was therefore not background-corrected. The nuclear cytoplasmic ratio was calculated by dividing the raw nuclear intensity by the raw cytoplasmic intensity. Movies and still images were extracted with FIJI/ImageJ.

FCS and N&B cell preparation and general settings

Two days before FCS and N&B experiments, 44.000 cells/well were seeded on an 8-well chamber slide with a glass bottom (80827-90, Ibidi). For low, FFS-compatible expression of control samples, $HAP1^{WT}$ cells were transfected with ~5 ng pSGFP2-C1, pEGFP (monomer), $pEGFP_2$ (dimer) or $pEGFP_3$ (trimer) and ~200 ng pBlueScript KS(+) per well with Turbofect, X-

tremeGene HP or Lipofectamine 3000 the day before the experiment. Lipofectamine 3000 yielded the best transfection efficiency. For Figure 4, 5, 8K and accompanying supplements, HAP1$^{SGFP2\text{-}CTNNB1}$ clone 2 was used. For Figure 7, 8 and accompanying supplements, CHIR99021 data was recorded and pooled for all three HAP1$^{SGFP2\text{-}CTNNB1}$ clones, and S45F data was recorded and pooled from HAP1$^{SGFP2\text{-}CTNNB1(S45F)}$ clones 2, 24 and 27 and HAP1$^{SGFP2\text{-}CTNNB1}$ clone 1 (the parental line for these S45F mutant clones) was used as the wild-type control.

FCS and N&B measurements were performed on an Olympus FV-1000 equipped with SepiaII and PicoHarp 300 modules (Picoquant, Berlin, Germany) at room temperature. An Olympus 60x water immersed UPLS Apochromat (N.A. 1.2) objective was used for FCS acquisition and Figure 3 supplement 1E, and an Olympus 60x silicon immersed UPLS Apochromat (N.A. 1.4) objective was used for N&B measurements. Green fluorophores were excited with a 488 nm diode laser (Picoquant) pulsing at 20 MHz and detected through a 405/480-488/560/635 nm dichroic mirror (Chroma, Bellows Falls, VT) and 525df45 nm bandpass filter (Semrock, Rochester, NY) with an Avalanche Photodiode (APD) (MPD, Bolzano, Italy). For, figure 2 supplement 1E and for FCS and N&B reference images the same laser and dichroic were used, but the signal was detected through a 505-540 bandpass filter with an internal PMT of the FV-1000 Olympus microscope.

FCS data acquisition and analysis

For FCS measurements, a confocal image was recorded. In this reference image, a single pixel was set as region of interest (ROI), based on its localization in the cytoplasm or nucleus as judged by the transmission image. In this ROI, the fluorescence intensity was measured over time using an APD, for typically 120 seconds.

FCS measurements were analyzed in FFS Dataprocessor version 2.3 (SSTC, Minsk, Belarus). The autocorrelation curve ($G(\tau)$) was calculated from the measured intensity (I) according to equation 1. Intensity traces with significant photobleaching, cell movement or focal drift were excluded from further analysis (see supplementary file 1 – tab FCS measurements and fitting). From other traces a portion of the trace with minimal (less than 10%) intensity drift or bleaching was selected to generate autocorrelation curve (AC).

$$G(\tau) = 1 + \frac{< \delta I(t) * \delta I(t+\tau) >}{< I >^2} \qquad \text{Eq. 1}$$

The resulting AC was fitted with a Triplet-state-diffusion model, described in equation 2. G_∞ accounts for offset in the AC for example by intensity drift. N is the average of the number of particles that reside in the confocal volume. F_{trip} and τ_{trip} describe the fraction of molecules in the dark state and the relaxation of this dark state respectively. Of note, in this case, F_{trip} and τ_{trip} account both for blinking of the fluorescent molecules and for the afterpulsing artefact of the APD. $\tau_{diff,i}$ describes the diffusion rate of the fluorescent molecules with the corresponding fraction, F_i. This diffusion time depends on the structural parameter (sp), which is defined as the ratio of the axial (ω_z) over the radial axis (ω_{xy}) of the observation volume.

$$G(\tau) = G_\infty + \frac{1}{< N >} * \frac{F_{trip}}{1 - F_{trip}} e^{\frac{-\tau}{\tau_{trip}}} * \sum_j \frac{F_i}{\left(1 + \frac{\tau}{\tau_{diff,i}}\right)\sqrt{1 + \frac{\tau}{\tau_{diff,i} * sp^2}}} \qquad \text{Eq. 2}$$

The apparent particle numbers (N_{apa}) for SGFP2-CTNNB1 were corrected for autofluorescence and bleaching (equation 3). The autofluorescence ($I_{autofluorescence}$) of HAP1 cells in the nucleus and cytoplasm was measured in untransfected HAP1 cells using the same settings as for FCS measurements. The correction for moderate bleaching is based on the intensity of the

968 selected portion of the intensity trace for AC calculation (I_{ana}) and the intensity at the start of
969 the measurement (I_{start}).

970 The size and shape of the observation volume was calibrated daily by measuring Alexa Fluor™
971 488 NHS Ester (A20000, Molecular probes, Thermo Scientific, stock dilution in MQ) in PBS in
972 a black glass-bottom cell imaging plate with 96 wells (0030741030, Eppendorf, Hamburg,
973 Germany). From the FCS measurements of Alexa488, the τ_{diff} and sp were determined by
974 fitting with a single diffusion and blinking component. The diffusion coefficient (D) of
975 Alexa488 in aqueous solutions at 22.5 °C is 435 $\mu m^2 s^{-1}$ (Petrášek and Schwille, 2008). From
976 these parameters, the axial diameter can be determined with equation 4 and the volume can
977 be approximated by a cylinder (equation 5). This allows for transformation of particle
978 numbers to concentrations (equation 5) and diffusion times to diffusion coefficients (equation
979 4) that are independent of measurement settings and small daily changes in alignment of the
980 microscope.

$$N_{corr} = N_{apa} * \left[1 - \frac{I_{autofluorescence}}{I_{total}}\right]^2 * \left[\frac{I_{start}}{I_{ana}}\right] \quad \text{Eq. 3}$$

$$\tau_{diff} = \frac{{\omega_{xy}}^2}{4D} \quad \text{Eq. 4}$$

$$V = 2\pi {\omega_{xy}}^3 * sp \quad \text{Eq. 5}$$

$$C = \frac{N_{corr}}{V * N_A} \quad \text{Eq. 6}$$

981 The model to fit SGFP2-CTNNB1 measurements contained 2 diffusion components. The first
982 diffusion component was fixed to the speed of monomeric SGFP2-CTNNB1. To estimate the

speed of monomeric SGFP2-CTNNB1, the speed of free floating SGFP2, transfected in HAP1 cells, was measured to be 24.1 $\mu m^2 s^{-1}$ using FCS. Subsequently, this speed was used to calculate the speed of monomeric SGFP2-CTNNB1 with Einstein-Stokes formula (Equation 7). As the temperature (T), dynamic viscosity (η) and Boltzmann's constant (k_B) are equal between SGFP2 and SGFP2-CTNNB1 measurements, the expected difference in diffusion speed is only caused by the radius (r) of the diffusing molecule assuming a spherical protein. The difference in radius was approximated by the cubic root of the ratio of the molecular weight of the SGFP2-CTNNB1 fusion protein (88 + 27=115 kDa) and the size of the SGFP2 protein (27 kDa), thus expecting a 1.62 times lower diffusion coefficient (compared to free floating SGFP2) of 14.9 $\mu m^2 s^{-1}$ for SGFP2-CTNNB1. It must be noted that, especially for larger protein complexes, the linearity between the radius of the protein and the speed is not ensured, if the shape is not globular, and due to other factors such as molecular crowding in the cell and hindrance from the cytoskeletal network. We therefore did not estimate the size of the measured CTNNB1 complexes, but rather compared them to measurements from other FCS studies.

$$D = \frac{k_B T}{6\pi\eta r} \qquad \text{Eq. 7}$$

In the fitting model, the structural parameter was fixed to the one determined by the Alexa488 measurements of that day. To ensure good fitting, limits were set for other parameters; G_∞ [0.5-1.5], N [0.001, 500], τ_{trip} [$1*10^{-6}$-0.05 ms], τ_{diff2} [10-150 ms]. This model was able to fit most Autocorrelation Curves from FCS measurements. In case of clear misfits, as judged by the distribution of residuals around the fitted curves, the measurement was excluded (see supplementary file 1 – tab FCS measurements and fitting).

N&B data acquisition and analysis

For N&B analysis, 50 images were acquired per measurement with a pixel time of 100 µs/pixel and a pixel size of 0.138-0.207 µm. The fluorescent signal was acquired with the APD described above for the FCS measurements. As a control and to optimize acquisition settings, HAP1 cells transfected with SGFP2, EGFP monomer, dimer or trimer were measured alongside HAP1$^{SGFP2\text{-}CTNNB1}$ cells treated with BSA, WNT3A, DMSO or CHIR99021, or HAP1$^{SGFP2\text{-}CTNNB1(S45F)}$ cells. APD readout was converted to a TIF stack using a custom build *.ptu* converter (Crosby et al., 2013). This TIF stack was further analyzed using an ImageJ macro script (modified from (Crosby et al., 2013), made available at https://osf.io/ys5qw/) based on Digman, Dalal, Horwitz, & Gratton, 2008. Within the script, average brightness and particle numbers were calculated for nuclear or cytoplasmic ROIs, which were set based on transmission image (see Figure 5F). Static or slow-moving particles, including membrane regions, were excluded by thresholding and/or ROI selection, since they can severely impact the brightness measured.

Data were further analyzed in R/RStudio. Brightness was normalized to the median value of the EGFP-monomer brightness measured on the same day in the same cellular compartment (nucleus/cytoplasm). Our FCS and N&B analysis assume a different confocal volume. In FCS we assume a cylinder with factor γ=1, whereas in N&B we assume a 3D-Gauss with factor γ=0.3536. To be able to compare particle numbers obtained with both techniques, particle numbers obtained with N&B were divided by the factor γ=0.3536.

Data representation and statistical analysis

Data processing and representation were performed in RStudio (version 1.1.456 running R 3.5.1 or 3.6.1). 95% confidence intervals of the median mentioned in the text and shown in Table 1-2 and Supplementary file 1 were calculated using PlotsOfDifferences (Goedhart,

2019). The P-values in Table 3 and Supplementary file 1 were also calculated using PlotsOfDifferences, which uses a randomization test and makes no assumption about the distribution of the data. Representation of the imaging data in Figure 4 supplement 2 and in supplementary movies 3-4 were generated in RStudio using a script based on PlotsOfDifferences (made available at https://osf.io/sxakf/).

Model description

We developed a minimal model for WNT signaling based on a previous model from the Kirschner group (Lee et al., 2003). The model is available as an interactive app at https://wntlab.shinyapps.io/WNT_minimal_model/ and the R source code of the model is available at https://osf.io/jx29z/ (WNT_minimal_model_v2.3.R).

Our minimal model comprises the following reactions:

$CB + DC \underset{k1}{\overset{k2}{\leftrightharpoons}} CB^* - DC$	Binding of cytoplasmic CTNNB1 (CB) to destruction complex	(1)
$CB^* - DC \overset{k3}{\rightarrow} DC + CB^*$	Release of phosphorylated CB (CB*) and recycling of the destruction complex	(2)
$DVL + DC \underset{k4}{\overset{k5}{\leftrightharpoons}} \mathrm{DC}^*$	Inactivation of the destruction complex by DVL	(3)
$CB \underset{k6}{\overset{k7}{\leftrightharpoons}} NB$	Nucleocytoplasmic shuttling of CB to and from the nucleus	(4)
$NB + TCF \underset{k8}{\overset{k9}{\leftrightharpoons}} NB - TCF$	Binding of NB to TCF	(5)

Below, we show the differential equations that govern the concentrations of the different compounds over time for the reactions described above. Table 4 in the main text gives the correspondence between the variables (i.e. x_1) in the differential equations and the model name (i.e. CB) in the reactions. The parameter w in equations (7) and (8) is $w = 0$ in the absence of WNT and $w = 1$ if WNT is present, i.e. in our minimal model the inactive form of

the destruction complex (DC*) is only present if WNT is present. The parameter b in equation (6) represents the constant production of CTNNB1, corresponding to v_{12} in Lee et al., 2003.

$$\frac{dx_1}{dt} = -k_1x_1x_2 + k_2x_3 - k_6x_1 + k_7x_5 + b \quad (6)$$

$$\frac{dx_2}{dt} = -k_1x_1x_2 + (k_2 + k_3)x_3 - w(k_4x_2 - k_5x_4) \quad (7)$$

$$\frac{dx_3}{dt} = k_1x_1x_2 - (k_2 + k_3)x_3 \quad (8)$$

$$\frac{dx_4}{dt} = w(k_4x_2 - k_5x_4) \quad (9)$$

$$\frac{dx_5}{dt} = k_6x_1 - k_7x_5 - k_8x_5x_6 + k_9x_7 \quad (10)$$

$$\frac{dx_6}{dt} = -k_8x_5x_6 + k_9x_7 \quad (11)$$

$$\frac{dx_7}{dt} = k_8x_5x_6 - k_9x_7 \quad (12)$$

Equilibrium conditions without WNT

The parameters in our model can in part be determined from our measurements of the equilibrium concentrations of CB, NB and their complexes, see Table 4-5 in the main text. Where we could not determine the parameters from our measurements, we used published values as indicated.

Under equilibrium conditions, the concentrations of the compounds do not change with time and the left-hand side of equations (6) - (12) is zero. From equations (10) and (11) we can determine the ratio of the rate constants k_6 and k_7 from the measured values of x_1 and x_5:

$$k_6x_1 = k_7x_5 \Leftrightarrow \frac{k_6}{k_7} = \frac{x_5}{x_1} = \frac{87}{91} = 0.96 \quad (13)$$

From equations (6), (8), (10) and (11) we have:

$$-k_3 x_3 + b = 0 \Leftrightarrow k_3 = \frac{b}{x_3} = \frac{0.423}{62.5} = 0.0068 \text{ min}^{-1} \quad (14)$$

Our reaction (1) corresponds closely to step 8 in Lee et al. therefore, we use the value of the dissociation constant $K_8 = 120$ nM from Lee et al. for our dissociation constant $K_1 = \frac{k_2}{k_1}$.

The concentration of the destruction complex is obtained from equation (1) under equilibrium conditions using equations (6), (8), (10), (11) and (14)

$$-k_1 x_1 x_2 + k_2 x_3 + b = 0$$

The value of b is assumed to be small compared to the two other terms, so we calculate the concentration of the destruction complex as:

$x_2 = K_1 \frac{x_3}{x_1} = 120 \frac{62.5}{91} = 82.4$ nM. It was then verified in our interactive app that this value for the destruction complex is indeed consistent with the equilibrium conditions without WNT stimulation.

To calculate the dissociation constant for the NB-TCF complex, we estimate an equilibrium concentration for free TCF (x_6) from Tan et al. (2012). From their Figure 11 it is seen that the bound TCF concentration in equilibrium in the presence of WNT has about the same value as the initial free TCF concentration and that no initial bound TCF is present. However, we measured NB-TCF also in the initial state. Therefore, we consider the free TCF concentration value from Tan et al. as a lower bound for the estimate of total TCF. Also, from Figure 11 of Tan et al. (2012) we estimate that of the initial free TCF, a fifth remains in the nucleus as free TCF after WNT is turned on. We measured 86 nM NB-TCF in the nucleus after the application of WNT. This leads to an estimate of the total concentration of TCF, TCF^0, in the nucleus of:

$[TCF^0] = 86 + 0.2 \times 86 = 103$ nM. If we assume that the total TCF concentration does not change by the application of WNT, we calculate the dissociation constant of the NB-TCF complex from equation (12):

$$k_8 x_5 (TCF^0 - x_7) = k_9 x_7 \Rightarrow \frac{k_9}{k_8} = K_2 = \frac{x_5 (TCF^0 - x_7)}{x_7} = \frac{87*81}{22} = 320 \text{ nM} \quad (15)$$

Equilibrium conditions with WNT

We model the action of WNT by deactivation of the destruction complex by DVL through reaction 3 by setting $w = 1$ in equations (7) and (9). The dissociation constant of CB*-DC, K_1, is assumed not to change in the presence of WNT. The measurements of free CB and NB in equilibrium (see Table 2) give for the ratio of k_6 and k_7:

$$k_6 x_1 = k_7 x_5 \Leftrightarrow \frac{k_6}{k_7} = \frac{x_5}{x_1} = \frac{170}{145} = 1.17 \quad (16)$$

The value of the rate of decay of the phosphorylated complex CB*-DC, k_3, is found to be the same for the "without WNT" situation:

$$-k_3 x_3 + b = 0 \Leftrightarrow k_3 = \frac{b}{x_3} = \frac{0.423}{62.5} = 0.0068 \text{ min}^{-1} \quad (17)$$

To uniquely determine the ratio of k_4 and k_5, we need the concentrations of the destruction complex DC and DC$*$ neither of which we have access to. We can, however, fit this ratio with our model to the measured values of x_1 and x_7 and find $k_4/k_5 = 1.7$.

We again calculate the dissociation constant of the NB-TCF complex from equation (12), using the concentrations for NB and NB-TCF obtained with FCS.

$$k_8 x_5 (TCF^0 - x_7) = k_9 x_7 \Rightarrow \frac{k_9}{k_8} = K_2 = \frac{x_5 (TCF^0 - x_7)}{x_7} = \frac{170*17}{86} = 33.6 \text{ nM} \quad (18)$$

Notice that we determined the ratios of the rate constants from the measured equilibrium values of free and bound CTNNB1 in the cytoplasm and the nucleus. This means that our rate constants are determined up to a multiplicative factor: the equilibrium equations do not change if all rate constants k_i and the parameter b are multiplied by the same factor, $Rate$. The factor $Rate$ determines how fast our model system reaches equilibrium. By comparing the times equilibrium was reached by the cytoplasmic and nuclear SGFP2-CTNNB1 signals (Figure 4 C, D) of about 4.5 hours, we fitted a factor $Rate = 20$ for our model.

Our model shows that the ratios of k_6/k_7 and k_9/k_8 are different for the conditions without and with WNT stimulation, suggesting a change in mechanism for nuclear shuttling of CTNNB1 and nuclear retention of CTNNB1 in going from the WNT 'off' situation to the WNT 'on' situation. It seems likely that such changes do not occur instantaneously. In our model we therefore allow a gradual rise in k_5/k_4 and a gradual transition of the ratios of k_6/k_7 and k_9/k_8 from WNT 'off' to the WNT 'on'. In our model this is included by setting a parameter ("Steep") that indicates the time after application of WNT the transition from WNT 'off' parameter values to WNT 'on' parameter values is complete. The value that gives a good approximation of the experimentally observed concentration curves is *Steep =150* minutes (Figure 6 panels B-F).

Acknowledgements

We thank the van Leeuwenhoek Centre for Advanced Microscopy (LCAM, Section Molecular Cytology, Swammerdam Institute for Life Sciences, University of Amsterdam) for the use of their facilities and LCAM staff for sharing their expertise and providing technical support, Jasmijn Span for cloning the color variants of the repair plasmid as a student in our lab, Marten Postma and Joachim Goedhart for assistance with data handling and analysis, Dorus Gadella for carefully reading the manuscript, and all colleagues for stimulating discussions and suggestions.

Figure supplements

Figure 1 - supplement 1: FACS Gating strategy for haploid HAP1 cells.

Figure 1 - supplement 2: *SGFP2-CTNNB1* locus

Figure 2 - supplement 1: Verification of the WNT/CTNNB1 responsiveness of HAP1 cells.

Figure 3 - supplement 1: Verification of imaging results with WNT3A three independent HAP1$^{SGFP2\text{-}CTNNB1}$ clones.

Figure 3 - supplement 2: Difference analysis of SGFP2-CTNNB1 fluorescence.

Figure 3 supplement 3: Unnormalized nuclear and cytoplasmic intensity measurements.

Figure 5 - supplement 1: Quantification of SGFP2-CTNNB1 particles, fluorescence and fluorescence lifetime.

Figure 5 supplement 2: Number and Brightness analysis

Figure 7 supplement 1 Generation and characterization of a S45F mutant cell line (HAP1$^{SGFP2\text{-}CTNNB1(S45F)}$).

Figure 8 supplement 1 Live imaging of HAP1$^{SGFP2\text{-}CTNNB1}$ upon CHIR99021 stimulation.

Figure 8 supplement 2 additional biophysical properties of SGFP2-CTNNB1^{S45F} and SGFP2-CTNNB1 under CHIR99021 stimulation.

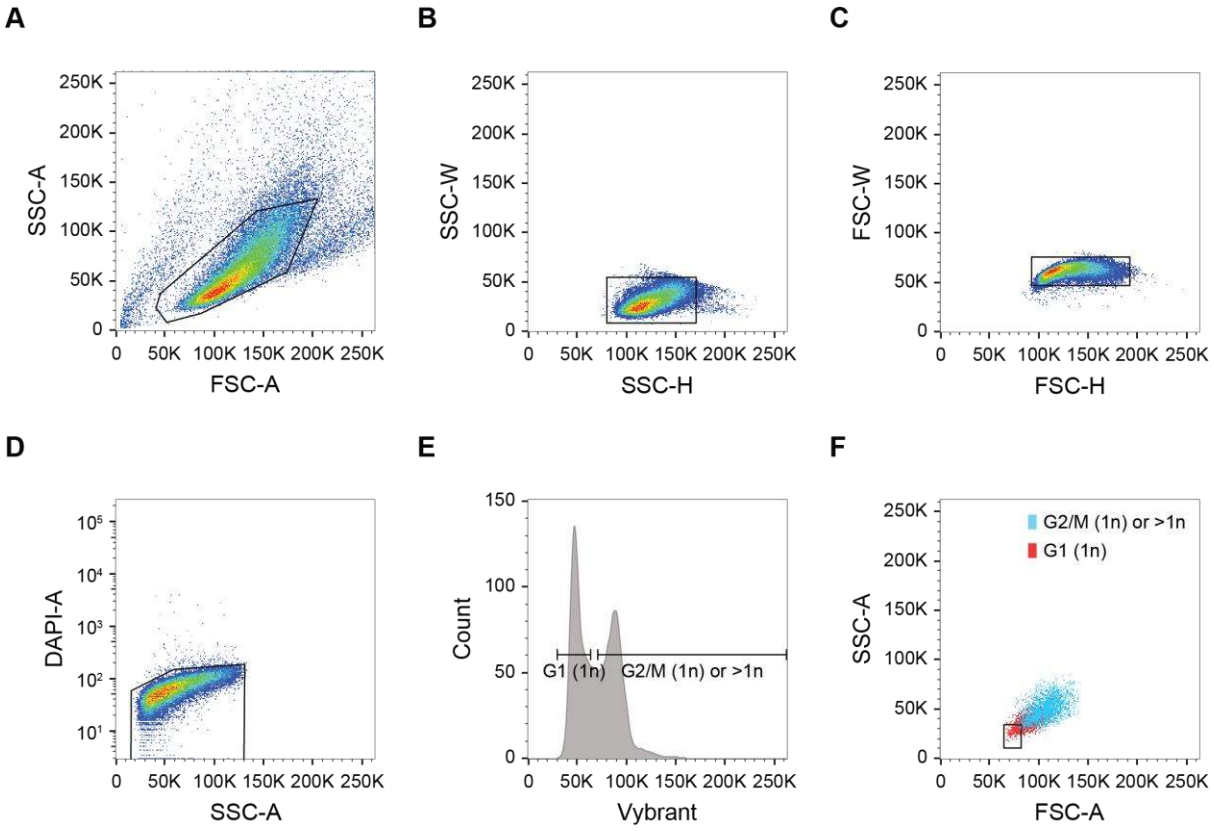

Figure 1 – supplement 1: FACS Gating strategy for haploid HAP1 cells. A-C) Single-cell gating based on forward scatter (FSC) and side scatter (SSC). D) Live cell gating based on DAPI exclusion. E-F) Haploid cell sorting based on Vibrant live-cell DNA dye. E) Haploid cell cycle profile. Only cells in G1 can be confidently identified as haploid (1n). The second peak contains both G2/M haploid cells, as well as diploid (2n) and polyploid events. Of note, the depicted HAP1^{WT} population is mainly haploid. F) Back-gating of the haploid G1 population from E onto the forward and side scatter plot. A stringent gate is set based on cell size to ensure only G1 (1n) cells qualify for sorting.

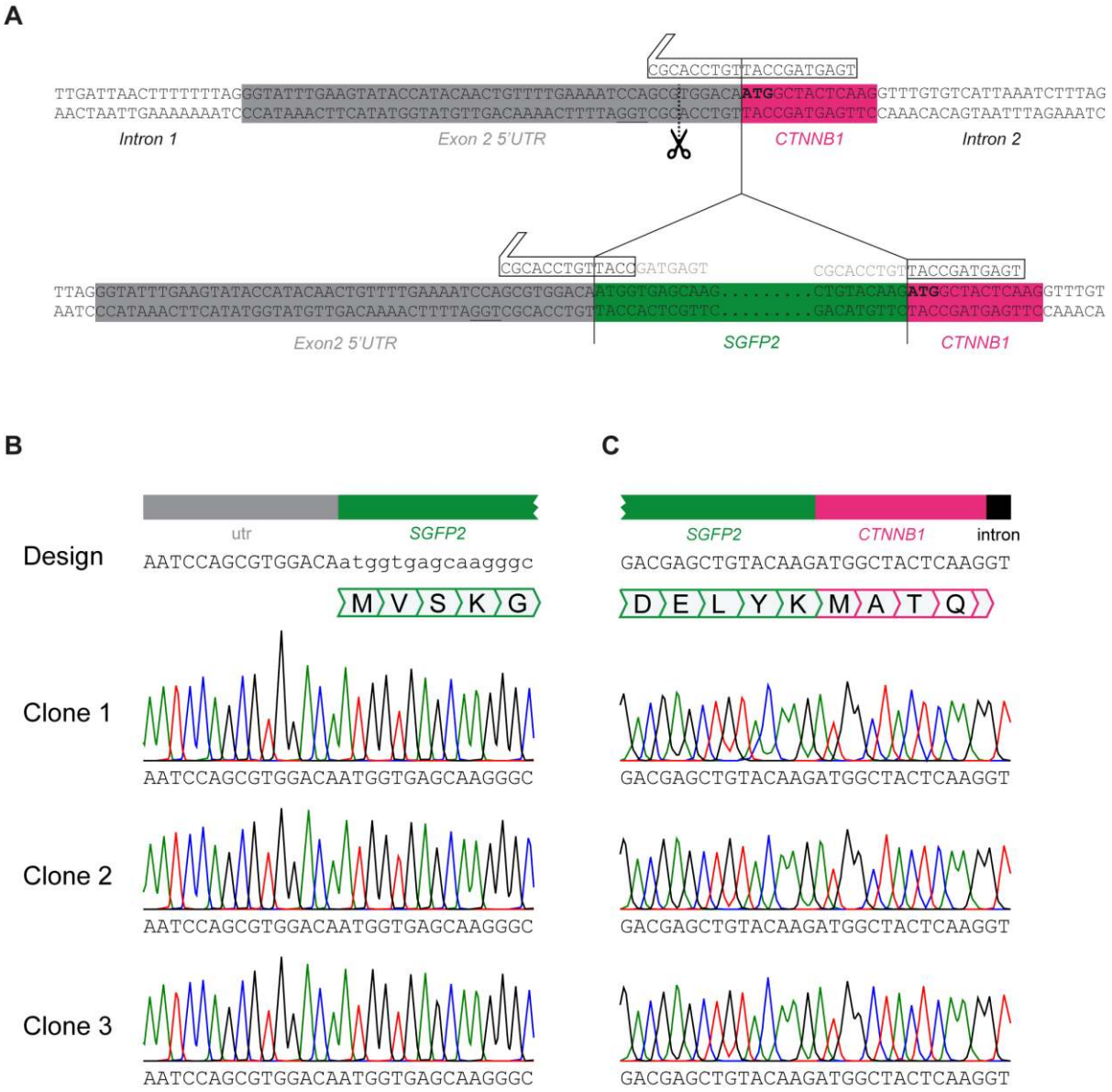

Figure 1 – supplement 2: *SGFP2-CTNNB1* locus A) Detailed view of *CTNNB1* exon 2 depicting gRNA design relative to the wildtype (top) and repaired (bottom) CTNNB1 allele. Note that the repair template contains the same sequence as the repaired allele depicted here. CTNNB1 sequences are shown in capital letters, SGFP2 sequences shown in lowercase. 5' UTR, *SGFP2* and *CTNNB1* and intron regions are indicated below the colored boxes. The gRNA (white arrow box above sequence) overlaps the start codon (depicted in bold), resulting in a Cas9-mediated double-strand break in the 5'UTR (predicted cut site indicated by dotted line and scissor, PAM site underlined). After successful homologous recombination, most of the gRNA binding site is destroyed, thus minimizing the chance of cutting the repair template or re-cutting the repaired allele. PCR based screening confirmed that 22/23 single-cell sorted clones indeed showed an integration of the expected size at the CTNNB1 locus. Complete sequence coverage of the insertion site in exon 2 was obtained for 9/11 sequenced clones, of which 8 showed the desired repair, and 1 clone showed an additional point mutation in the repaired locus. B-C) Sequencing of three independent HAP1$^{SGFP2\text{-}CTNNB1}$ clones on the 5' (B) and the 3' (C) end of *SGFP2* integration in exon 2 of *CTNNB1*. Sanger sequencing of the endogenous *CTNNB1* locus of clone 1, clone 2 and clone 3 shows an exact match to the design and thus correct homology directed repair.

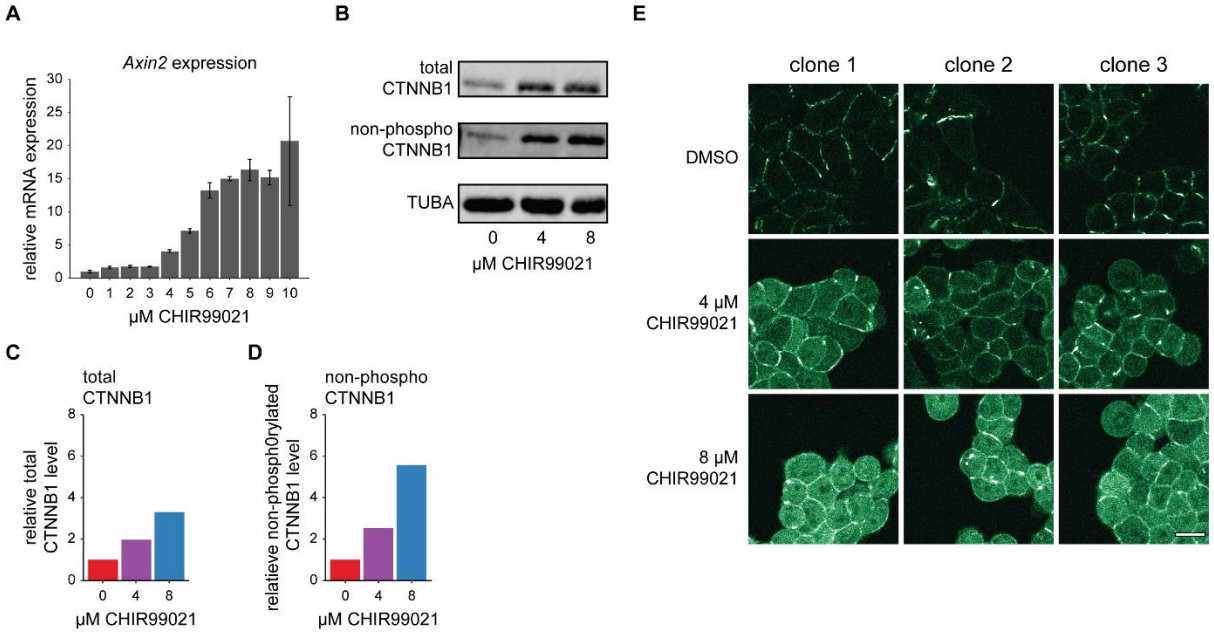

Figure 2 supplement 1: Verification of the WNT/CTNNB1 responsiveness of HAP1 cells. A) Graph depicting *AXIN2* qRT-PCR results from HAP1^{WT} cells treated with the indicated range of CHIR99021 (1-10 µM) or DMSO vehicle control (0 µM) for 24 hours. *HPRT* was used as a reference gene. Error bars represent standard deviation within technical triplicates from n=1 biological experiment. Based on this, we selected 4uM and 8 µM as intermediate and high levels of WNT/CTNNB1 pathway induction for follow up experiments. B) Western blot, showing the increase in total (top) and non-phosphorylated (i.e. active) CTNNB1 levels (middle) in response to pathway stimulation. HAP1^{WT} cells were treated for 24 hours with 4 or 8 µM CHIR99021, or DMSO vehicle control (0 µM). Alpha-Tubulin (TUBA, bottom) serves as a loading control. C-D) Quantification of the western blot from (B) depicting the relative fold change of total CTNNB1 (C) or non-phosphorylated CTNNB1 (D) to DMSO control corrected for Tubulin loading. E) Representative confocal microscopy images of three independent HAP1$^{SGFP2\text{-}CTNNB1}$ clones, treated for 24 hours with 4 or 8 µM CHIR99021, or DMSO vehicle control. Scalebar is 10 µm.

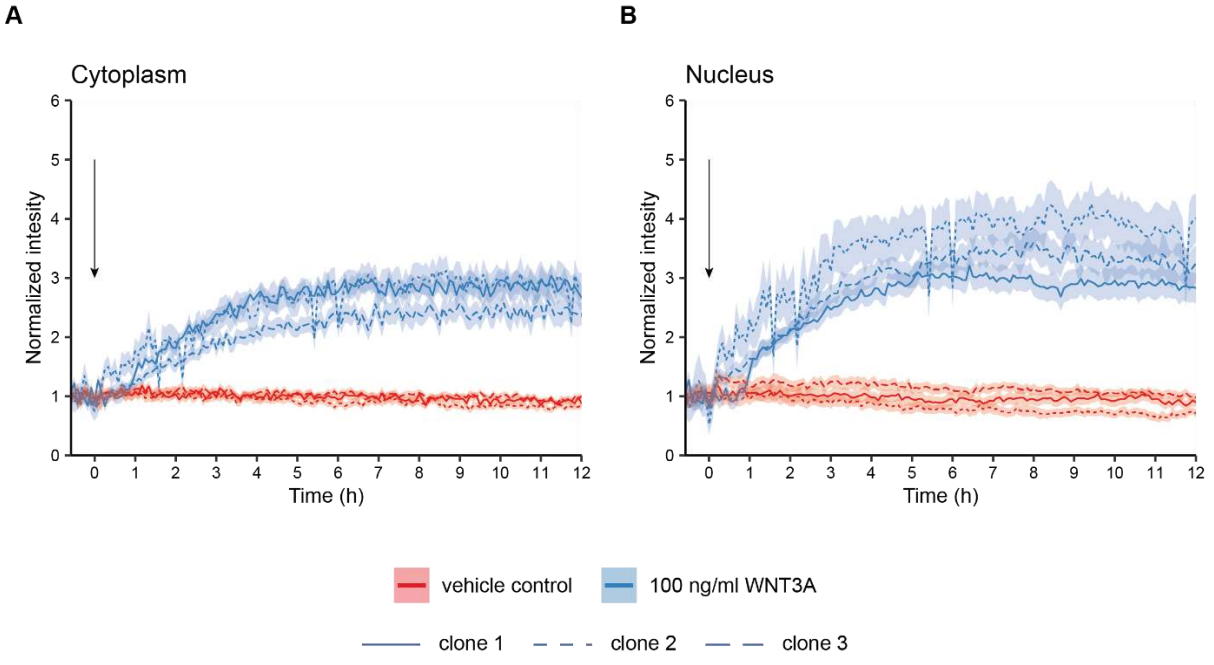

Figure 3 supplement 1: Graphs showing quantification of time-lapse microscopy experiments with three independent HAP1$^{SGFP2\text{-}CTNNB1}$ clones. Stills of this experiment are shown in Figure 3C. Segmentation was performed as described in Figure 4. Arrow indicates the moment of starting the different treatments (BSA in red or 100 ng/ml WNT3A in blue). Solid lines represent the mean normalized intensity and shading the 95% confidence interval in the cytoplasm (A) or nucleus (B). Line pattern indicates the three different clones. n=13-158 cells for each condition and time point for n=1 biological experiment.

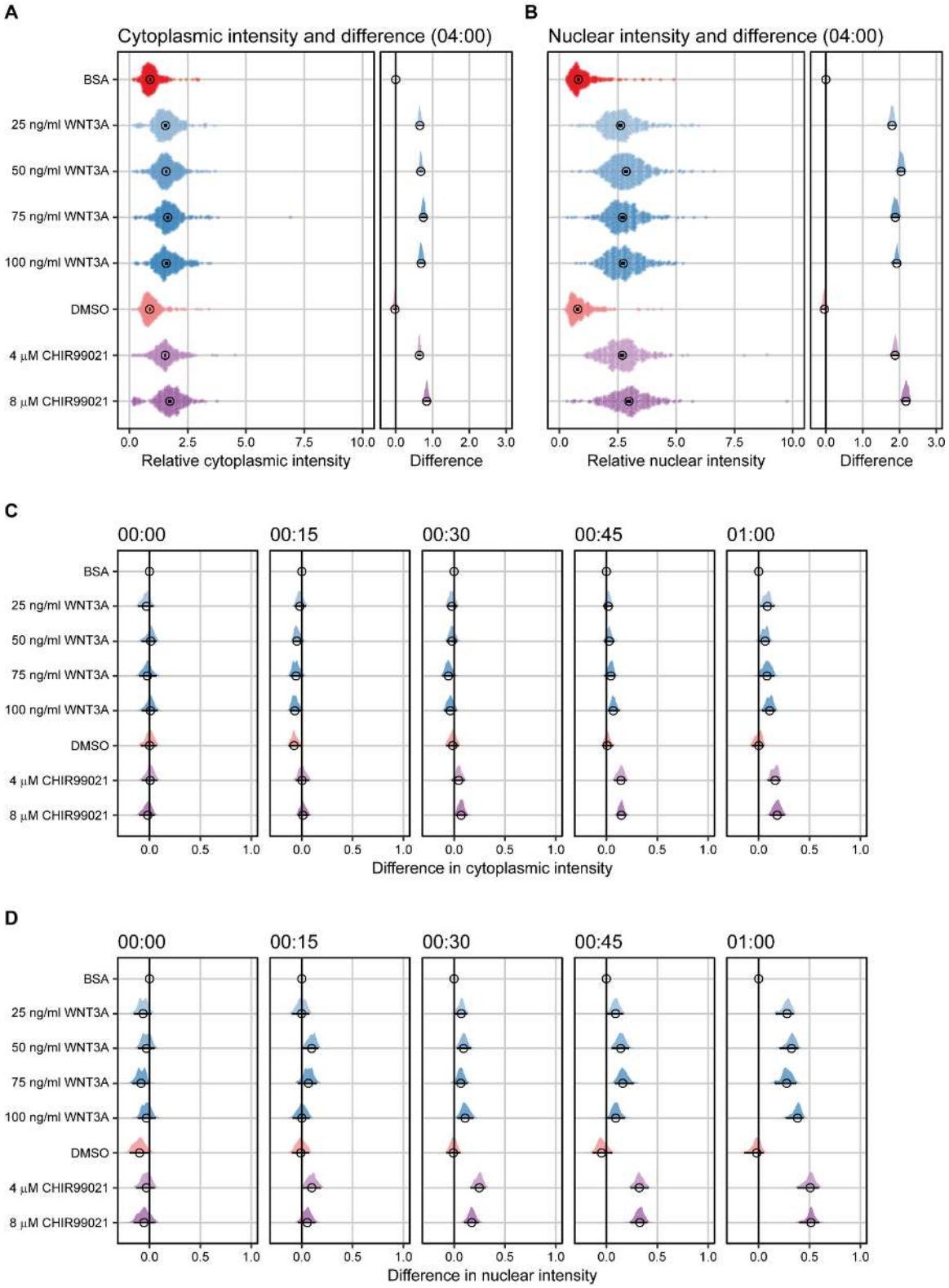

Figure 3 supplement 2: Difference analysis of SGFP2-CTNNB1 fluorescence. A-B) Plots depicting the relative intensity (left) and the difference in relative intensity to BSA treated cells (right) in the cytoplasm (A) and nucleus (B) after 4 hours of treatment. Circles indicate the median value and bars indicate the 95% CI. In the relative intensity plot (left) the distribution is built from individual data points in a violin-type fashion to faithfully represent the distribution of data. In the difference plot (right) the distribution of differences is represented in a half violin plot. If the 95% CI in the difference plot does not overlap the zero line, which indicates no difference, the sample is significantly different from BSA control condition. C-D) Plots depicting the difference in relative intensity in the cytoplasm (C) and nucleus (D) between the moment of addition and 1 hour of treatment. Titles indicate the time (hh:mm). The distribution of differences is represented in a half violin plot. Circles indicate the median value and bars indicate the 95% CI. If the 95% CI does not overlap the zero line, which indicates no difference, the sample is significantly different from the BSA control condition.

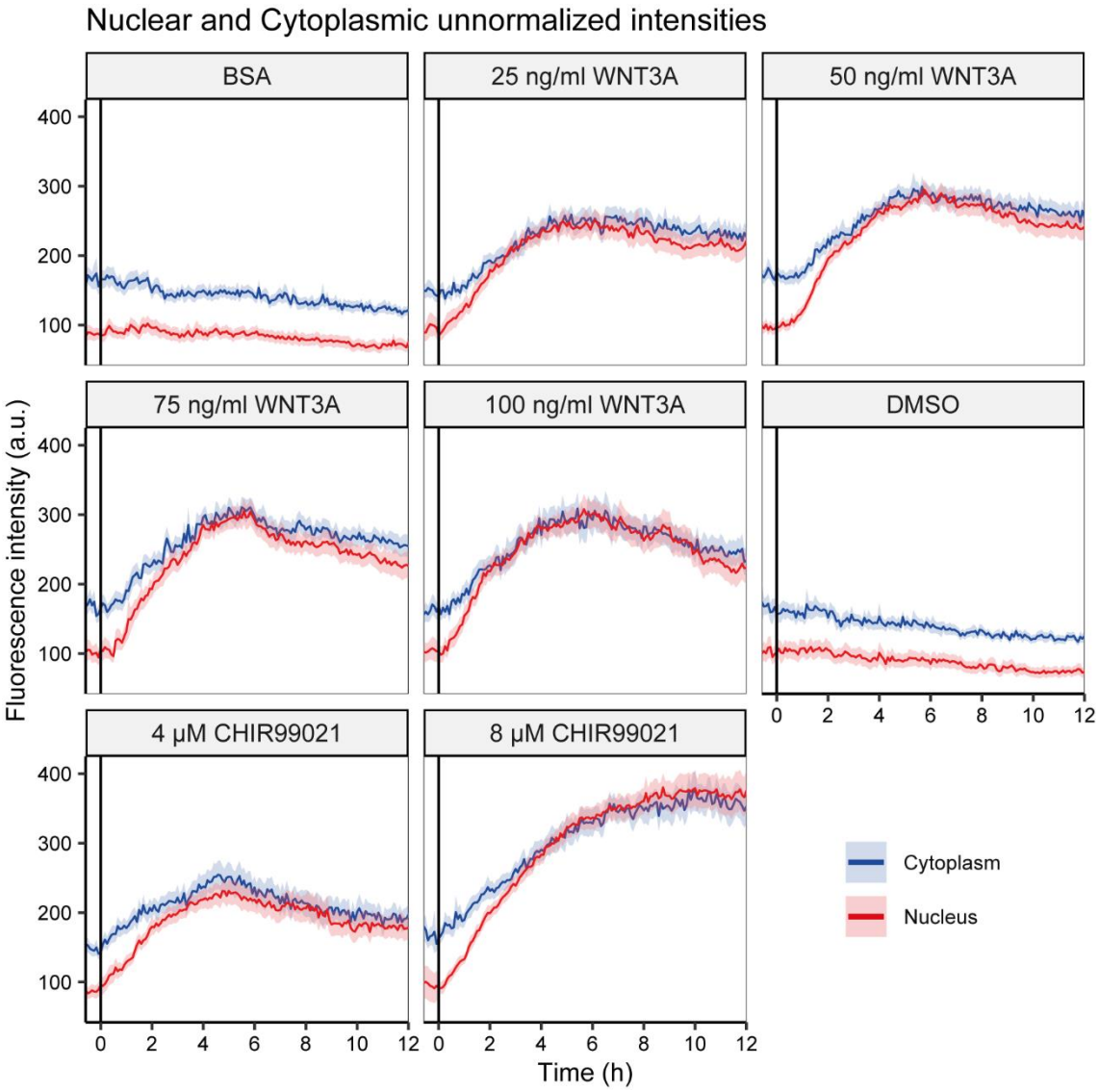

Figure 3 supplement 3: Unnormalized nuclear and cytoplasmic intensity measurements. Graphs showing the unnormalized fluorescence intensities quantified for a single biological replicate shown in Figure 3. The vertical black lines indicate the moment of starting the different treatments (as indicated on top of each graph). Solid lines represent the mean normalized intensity and shading the 95% confidence interval in the cytoplasm (blue) or nucleus (red). n=64-148 cells for each condition and time point.

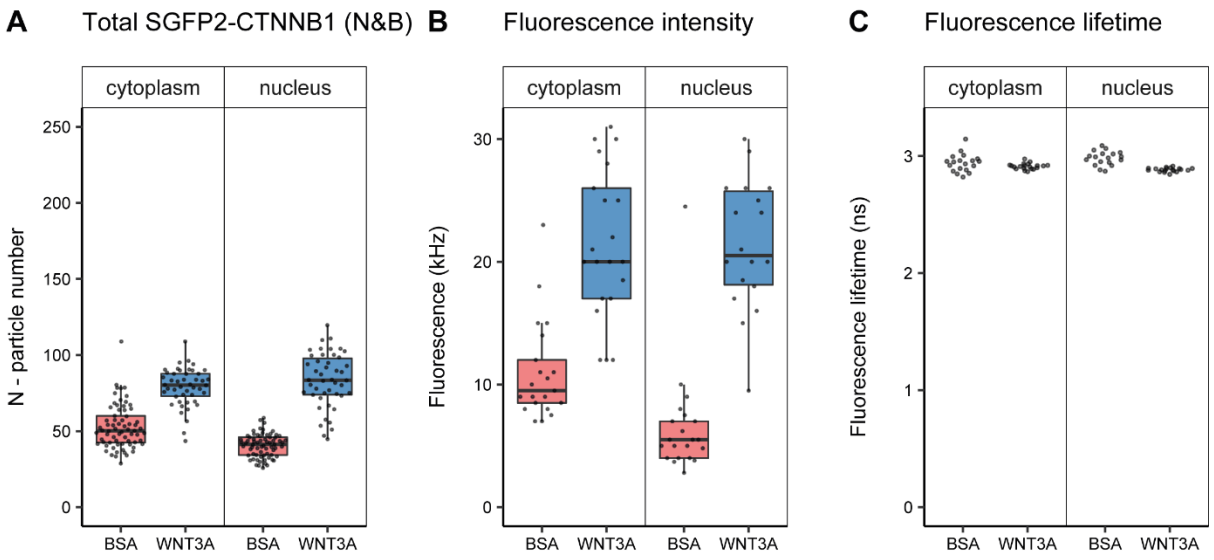

Figure 5 supplement 1 Quantification of SGFP2-CTNNB1 particles, fluorescence and fluorescence lifetime. Details on sample size and statistics can be found in supplementary file 1. A) Graph depicting the total number of SGFP2-CTNNB1 particles as measured with N&B. B) Graph depicting the average fluorescence intensity at the start of the FCS measurement. The increase in SGFP2-CTNNB1 fluorescence in the cytoplasm (2.1-fold) exceeds the increase in the SGFP2-CTNNB1 concentration (1.1-fold, Figure 5A), but does correspond to the relative increase measured by time-lapse imaging (1.7-fold, Figure 4C). C) Graph depicting fluorescence lifetimes calculated from the FCS measurements. The Fluorescence lifetime of SGFP2-CTNNB1 is independent of the subcellular compartment and treatment. Therefore, photophysical effects are not the cause for the difference between the fold-change in fluorescence and concentrations of the FCS measurements as described in (B).

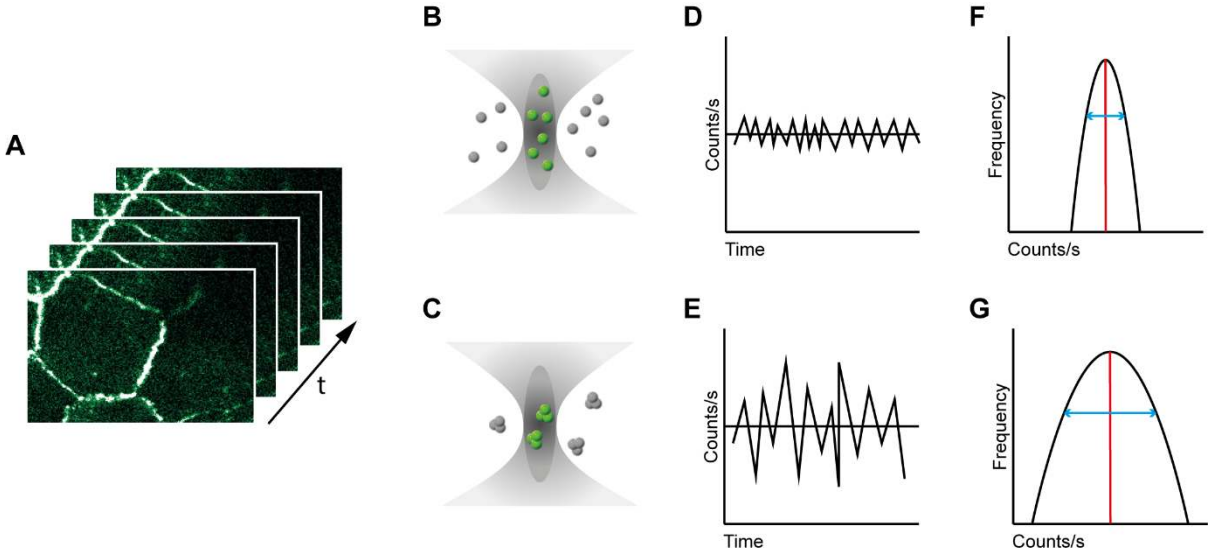

Figure 5 supplement 2: Number and Brightness analysis A) A series of images are acquired over time (t) B-C) Representation of the confocal volume in a single pixel of the image in (A) representing monomers with a brightness of 1 (B) and trimers with a brightness of 3 (C) both confocal volumes emit a fluorescence of 6. D-E) Graph depicting the variation in fluorescence, measured by an APD in counts/s, in a single pixel over time for the monomer (D) and trimer (E). With a higher brightness the variation around the average becomes larger. Note that the time-scale in N&B is much larger than in FCS (Figure 4 A-C) due to the use of images rather than a single point and therefore the variation is no longer dependent on diffusion kinetics. F-G) Graph depicting the distribution of fluorescence observed in a single pixel. The average (red line) in our case is the same for 6 monomers (F) or 2 trimers (G), but the standard deviation (blue line) is much larger for the trimer. The average and standard deviation are used to calculate the number

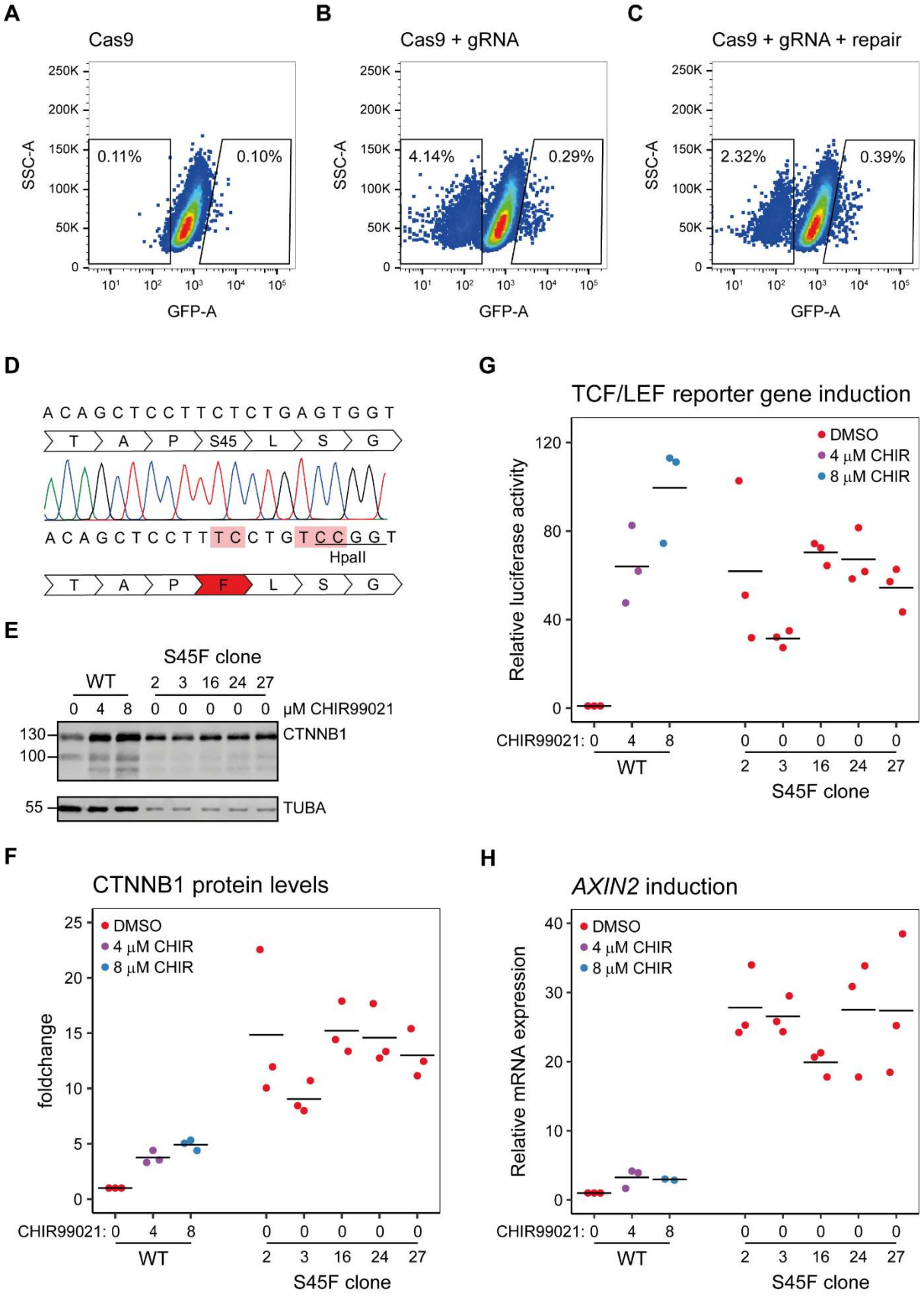

Figure 7 supplement 1 Generation and characterization of a S45F mutant cell line (HAP1$^{SGFP2\text{-}CTNNB1(S45F)}$). A-C) FACS graphs showing the selection strategy for HAP1$^{SGFP2\text{-}CTNNB1(S45F)}$ cells. HAP1$^{SGFP2\text{-}CTNNB1}$ clone 1 was transfected with CRISPR constructs similar to figure 1C, see material and methods for details. Transfection with a guide RNA in the third exon of CTNNB1 resulted in a population with reduced SGFP2 fluorescence and a population with increased fluorescence (B) compared to a Cas9 only control (A). Co-transfection of a single stranded

oligo repair, led to a reduction in the population with decreased SGFP2 fluorescence (representing cells repaired with NHEJ that resulted in a loss of the SGFP2-CTNNB1 fusion protein) and an increase in the population with increased SGFP2 fluorescence (representing cells repaired with NHEJ that resulted in a stabilizing SGPF2-CTNNB1 truncation, mutation, insertion or deletion as well as cells with the correct HDR resulting in the stabilizing S45F mutation). Cells with increased fluorescence were sorted as single haploid cells (see Figure 1 Supplement 1) and expanded for further analysis D) Graphical representation of part of the 3rd exon of SGFP2-CTNNB1 before (top) and after (bottom) CRISPR/Cas9-mediated mutagenesis. Sanger sequencing is shown for one correctly targeted clone. The mutation changes the 45th serine to a phenylalanine (S45F) and additionally removes the gRNA binding site and a silent mutation that introduces a HpaII restriction site for screening purposes. Mutated bases are indicated in light red. 14/32 single cell clones showed the expected genotyping fragment size and 7/32 showed large insertions or deletions. 7/14 clones showed the expected genotyping band contained the HpaII restriction site, 3/14 did not. Sanger sequencing coverage for the exon3 locus was obtained for 6/7 clones and all showed correct targeting (as shown for 1 clone here). Five clones were further analyzed; Clone 2,3,16 and 24 are from one single transfection, clone 27 from an independent transfection. E) Western blot, showing SGFP2-CTNNB1^{WT} (WT) and SGFP2 CTNNB1^{S45F} (S45F clone) protein levels. All panels are from one blot that was cut at the 70 kDa mark. Top: HAP1$^{SGFP2\text{-}CTNNB1(WT)}$and HAP1$^{SGFP2\text{-}CTNNB1(S45F)}$ clones express the SGFP2-CTNNB1 protein at the expected height. Bottom: alpha-Tubulin (TUBA) loading control. A representative image of n=3 independent experiments is shown. F) Quantification of Western blots from n=3 independent experiments, including the one in, normalized to the SGFP2-CTNNB1^{WT} control (E), showing that the S45F clones express higher levels of SGFP2-CTNNB1 than their HAP1$^{SGFP2\text{-}CTNNB1(WT)}$ parental line, even after 24h treatment with 8µM CHIR99021. Horizontal bar indicates the mean. G) Graph depicting the results from a MegaTopflash dual luciferase reporter assay, showing increased levels of TCF/LEF reporter gene activation for and HAP1$^{SGFP2\text{-}CTNNB1(S45F)}$, comparable to HAP1$^{SGFP2\text{-}CTNNB1(WT)}$ cells treated for 24 hours with 8µM CHIR99021 treatment. Data points from n=3 independent experiments are shown. Horizontal bar indicates the mean. Values are depicted relative to the DMSO control, which was set to 1 for each individual cell line. H)

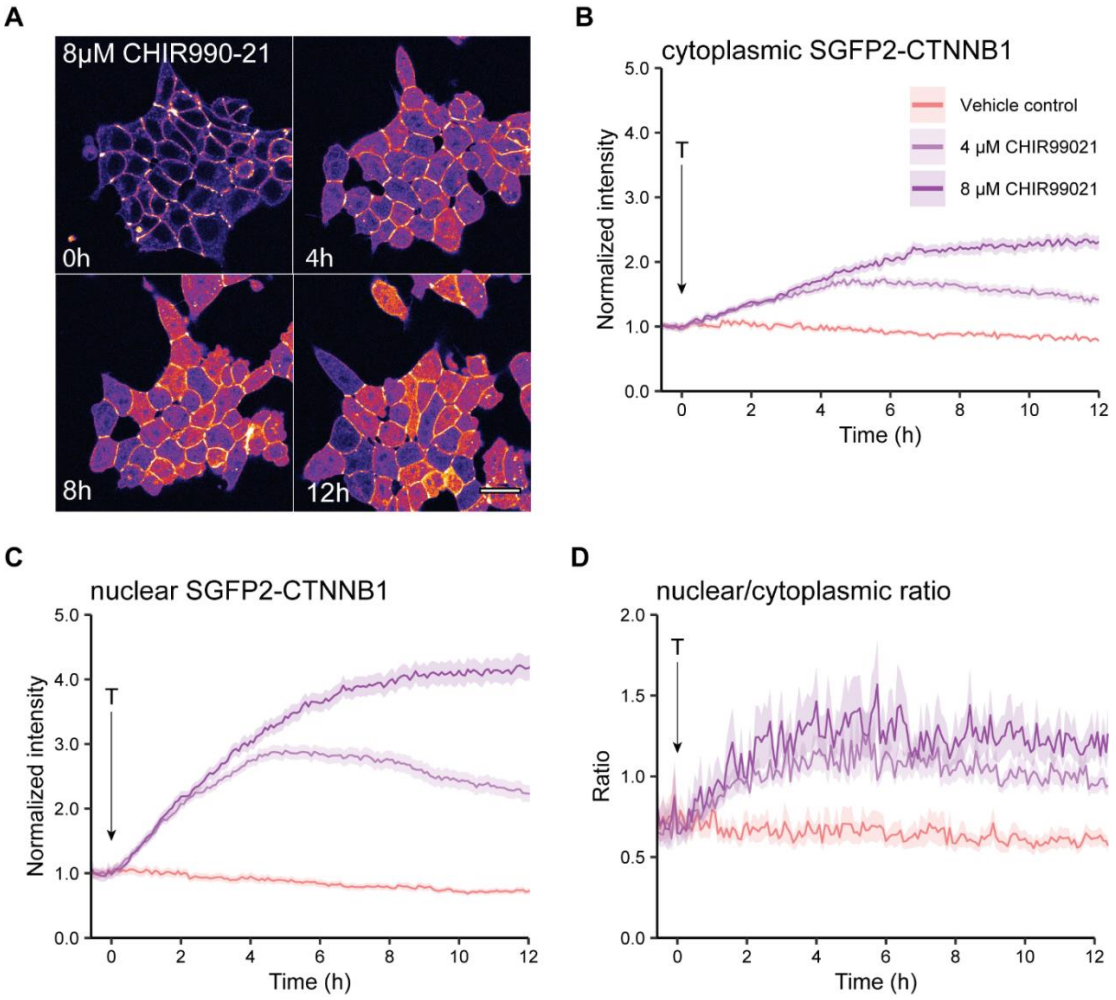

Figure 8 supplement 1 Live imaging of HAP1$^{SGFP2\text{-}CTNNB1}$ upon CHIR99021 stimulation. A) Representative stills from confocal time-lapse experiments corresponding to Supplementary Movies 3, showing an increase of SGFP2-CTNNB1 after treatment with 8µM CHIR99021. Scale bar = 20 µm. B-D) Quantification of time-lapse microscopy series, using the segmentation pipeline shown in Figure 3E. Arrow indicates the moment of starting the different treatments (T, see legend in B for details). B-C) Graph depicting the normalized intensity of SGFP2-CTNNB1 in the cytoplasm (B) or nucleus (C) over time. Solid lines represent the mean normalized fluorescence intensity and shading indicates the 95% confidence interval. n=166-400 cells for each condition and time point, pooled data from n=3 independent biological experiments. D) Graph depicting the nuclear/cytoplasmic ratio of SGFP2-CTNNB1 over time, calculated from raw intensity values underlying (B) and (C). This experiment was recorded simulateously with the data shown in Figure 3. Additional data representation of this experiment is found in Figure 3 supplement 2 and Supplementary movies 4-6.

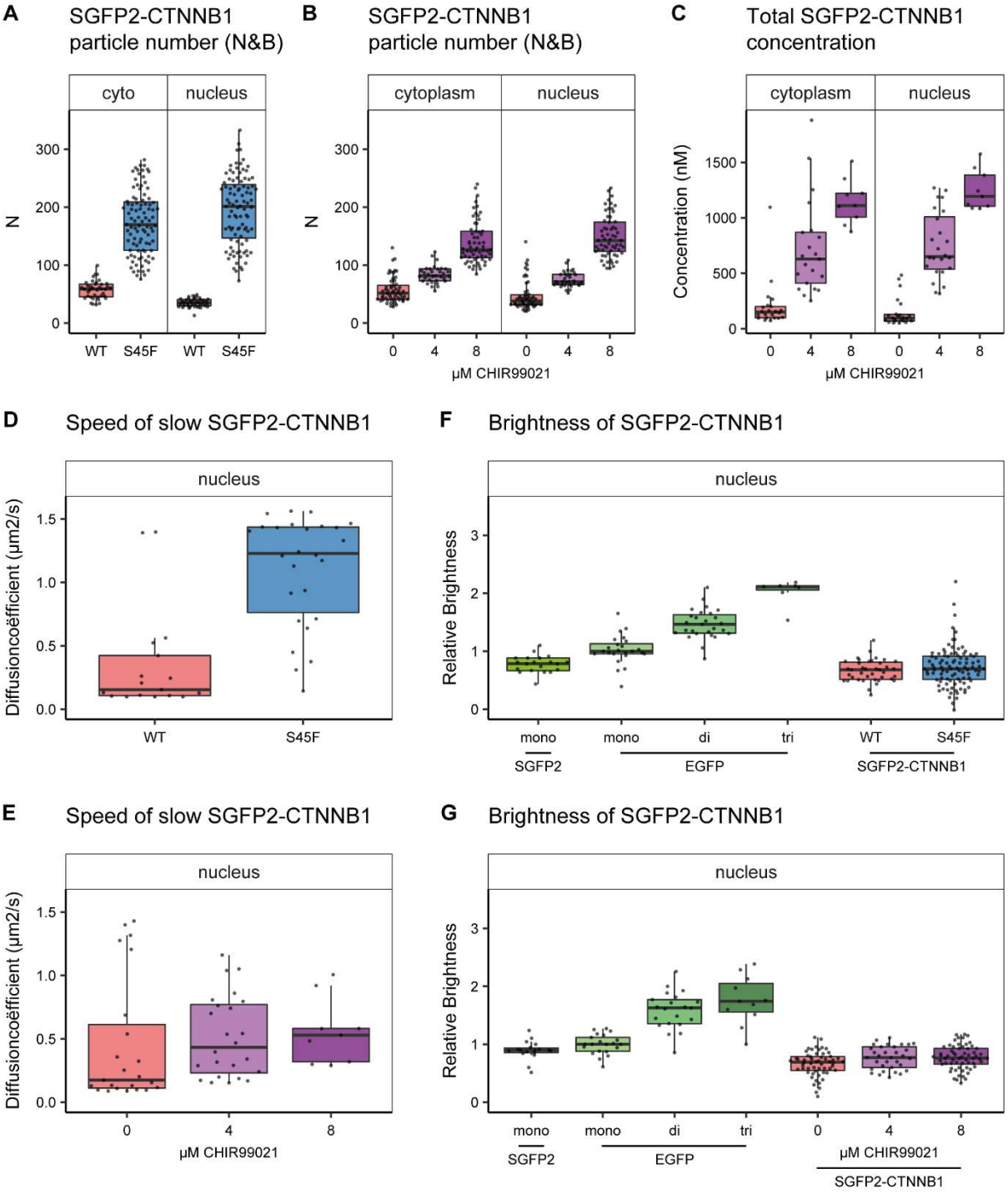

Figure 8 supplement 2 additional biophysical properties of SGFP2-CTNNB1^{S45F} and SGFP2-CTNNB1 under CHIR99021 stimulation. The S45F mutant was introduced using CRISPR (see Figure 7 supplement 1) and CHIR treated and control cells were measured after 24 hours. Details on sample size and statistics can be found in supplementary file 1. A-B) Graph depicting the total number of SGFP2-CTNNB1 particles as measured with N&B upon S45F mutation (A) or CHIR99021 stimulation (B). C) Graph depicting the total concentration of SGFP2-CTNNB1 particles (monomeric plus complexed) as measured with FCS upon CHIR99021 treatment. D-E) Graphs depicting the speed of the second diffusion component (i.e. SGFP2-CTNNB1 containing complex) in the nucleus measured by FCS for S45F mutant (D) or 24 hour CHIR99021 treatment (E). E-F) Graph depicting the molecular brightness of SGFP2-CTNNB1 in the nucleus relative to controls as measured with N&B. EGFP monomer was used for normalization and EGFP dimer and trimer as controls for N&B measurements.

Supplementary Movie legends

Supplementary Movie 1-3: Representative movies of confocal time-lapse experiments, showing SGFP2-CTNNB1 (left, green), SiR-DNA staining (middle, magenta) and transmission image (right, grey) after treatment with vehicle control (BSA) (**Supplementary Movie 1**), 100 ng/ml WNT3A (**Supplementary Movie 2**) or 8 µM CHIR99021 (**Supplementary Movie 3**). Time of addition is at 00:00:00 (indicated at the top left). Scale bar in the lower right represents 20µm.

Supplementary Movie 4-6: Movies showing the quantification of time-lapse microscopy series (from Figure 4 and Supplementary Movie 1-3) at each time point showing all individual cells from 3 biological experiments. Time of addition of the indicated substances is at 00:00:00 (indicated at the top left). The left graph represents the raw data (colored dots, each dot is one cell, n=155-400 cells for each condition and time point), the median (black circle) and the 95% CI of the median (black bar). The right graph represents the median difference (black circle) from the treatments to the control (BSA). When the 95% CI (black bar) does not overlap 0, the difference between the two conditions is significant.

Supplementary Movie 4: Quantification of the normalized intensity of SGFP2-CTNNB1 in the cytoplasm. Significant changes in intensity can first be observed after 40 minutes of 8 µM CHIR99021, and after 70-80 minutes of 4 µM CHIR99021 or 25-100ng/ml WNT3A treatment.

Supplementary Movie 5: Quantification of the normalized intensity of SGFP2-CTNNB1 in the nucleus. Significant changes in intensity can be observed for all treatments (but not controls) after 20-50 minutes.

Supplementary Movie 6: Quantification of the nuclear-cytoplasmic ratio of SGFP2-CTNNB1, calculated from raw intensity values underlying Supplementary Movies 4 and 5. Significant changes in the nuclear-cytoplasmic ratio can be observed for all treatments (but not controls) after 20-50 minutes.

Supplementary Files

Supplementary File 1: Tables of all summary statistics (mean, median, 95% confidence intervals, differences, p-values) of the FCS and N&B parameters show in Figure 5, 7 and 8 and accompanying supplements.

References

Aberle, H., Bauer, A., Stappert, J., Kispert, A., and Kemler, R. (1997). β-catenin is a target for the ubiquitin-proteasome pathway. EMBO J. *16*, 3797–3804.

Agajanian, M.J., Walker, M.P., Axtman, A.D., Ruela-de-Sousa, R.R., Serafin, D.S., Rabinowitz, A.D., Graham, D.M., Ryan, M.B., Tamir, T., Nakamichi, Y., et al. (2019). WNT Activates the AAK1 Kinase to Promote Clathrin-Mediated Endocytosis of LRP6 and Establish a Negative Feedback Loop. Cell Rep. *26*, 79-93.e8.

Ambrosi, G., Voloshanenko, O., Eckert, A., Kranz, D., Nienhaus, G.U., and Boutros, M. (2020). Allele-specific endogenous tagging and quantitative analysis of β-catenin in colon cancer cells. BioRxiv.

van Amerongen, R., and Nusse, R. (2009). Towards an integrated view of Wnt signaling in development. Development *136*, 3205–3214.

van Amerongen, R., Bowman, A.N., and Nusse, R. (2012). Developmental stage and time dictate the fate of Wnt/β-catenin-responsive stem cells in the mammary gland. Cell Stem Cell *11*, 387–400.

Amit, S., Hatzubai, A., Birman, Y., Andersen, J.S., Ben-shushan, E., Mann, M., Ben-neriah, Y., and Alkalay, I. (2002). Axin-mediated CKI phosphorylation of β-catenin at Ser 45: a molecular switch for the Wnt pathway. Genes Dev. *16*, 1066–1076.

Andersson, B.S., Beran, M., Pathak, S., Goodacre, A., Barlogie, B., and McCredie, K.B. (1987). Ph-positive chronic myeloid leukemia with near-haploid conversion in vivo and establishment of a continuously growing cell line with similar cytogenetic pattern. Cancer Genet. Cytogenet. *24*, 335–343.

1295 Armstrong, N.J., Fagotto, F., Prothmann, C., and Rupp, R.A.W. (2012). Maternal Wnt/β-
1296 catenin signaling coactivates transcription through NF-κB binding sites during xenopus axis
1297 formation. PLoS One *7*.

1298 Bain, J., Plater, L., Elliott, M., Shpiro, N., Hastie, C.J., Mclauchlan, H., Klevernic, I., Arthur,
1299 J.S.C., Alessi, D.R., and Cohen, P. (2007). The selectivity of protein kinase inhibitors: A further
1300 update. Biochem. J. *408*, 297–315.

1301 Barker, N., van Es, J.H., Kuipers, J., Kujala, P., van den Born, M., Cozijnsen, M., Haegebarth,
1302 A., Korving, J., Begthel, H., Peters, P.J., et al. (2007). Identification of stem cells in small
1303 intestine and colon by marker gene Lgr5. Nature *449*, 1003–1007.

1304 Behrens, J., von Kries, J.P., Kühl, M., Bruhn, L., Wedlich, D., Grosschedl, R., and Birchmeier,
1305 W. (1996). Functional interaction of beta-catenin with the transcription factor LEF-1. Nature
1306 *382*, 638–642.

1307 Bilic, J., Huang, Y.-L., Davidson, G., Zimmermann, T., Cruciat, C.-M.C.-M., Bienz, M., and
1308 Niehrs, C. (2007). Wnt induces LRP6 signalosomes and promotes dishevelled-dependent
1309 LRP6 phosphorylation. Science *316*, 1619–1622.

1310 Bindels, D.S., Haarbosch, L., van Weeren, L., Postma, M., Wiese, K.E., Mastop, M., Aumonier,
1311 S., Gotthard, G., Royant, A., Hink, M.A., et al. (2017). mScarlet: a bright monomeric red
1312 fluorescent protein for cellular imaging. Nat. Methods *14*, 53–56.

1313 Bugter, J.M., Fenderico, N., and Maurice, M.M. (2020). Mutations and mechanisms of WNT
1314 pathway tumour suppressors in cancer. Nat. Rev. Cancer.

1315 Canaj, H., Hussmann, J.A., Li, H., Beckman, K.A., Goodrich, L., Cho, Nathan, H., Li, Y.J., Santos,
1316 D.A., McGeever, A., Stewart, E.M., et al. (2019). Deep profiling reveals substantial

heterogeneity of integration outcomes in CRISPR knock-in experiments. BioRxiv.

Cantù, C., Felker, A., Zimmerli, D., Prummel, K.D., Cabello, E.M., Chiavacci, E., Méndez-Acevedo, K.M., Kirchgeorg, L., Burger, S., Ripoll, J., et al. (2018). Mutations in Bcl9 and Pygo genes cause congenital heart defects by tissue-specific perturbation of Wnt/β-catenin signaling. Genes Dev. *32*, 1443–1458.

Carette, J.E., Raaben, M., Wong, A.C., Herbert, A.S., Obernosterer, G., Mulherkar, N., Kuehne, A.I., Kranzusch, P.J., Griffin, A.M., Ruthel, G., et al. (2011). Ebola virus entry requires the cholesterol transporter Niemann-Pick C1. Nature *477*, 340–343.

Chhabra, S., Liu, L., Goh, R., Kong, X., and Warmflash, A. (2019). Dissecting the dynamics of signaling events in the BMP, WNT, and NODAL cascade during self-organized fate patterning in human gastruloids. PLOS Biol. *17*, e3000498.

Crosby, K.C., Postma, M., Hink, M.A., Zeelenberg, C.H.C., Adjobo-Hermans, M.J.W., and Gadella, T.W.J. (2013). Quantitative analysis of self-association and mobility of Annexin A4 at the plasma membrane. Biophys. J. *104*, 1875–1885.

Digman, M.A., Dalal, R., Horwitz, A.F., and Gratton, E. (2008). Mapping the number of molecules and brightness in the laser scanning microscope. Biophys. J. *94*, 2320–2332.

Doumpas, N., Lampart, F., Robinson, M.D., Lentini, A., Nestor, C.E., Cantù, C., and Basler, K. (2019). TCF / LEF dependent and independent transcriptional regulation of Wnt/β-catenin target genes . EMBO J. *38*, 1–14.

Dross, N., Spriet, C., Zwerger, M., Müller, G., Waldeck, W., and Langowski, J. (2009). Mapping eGFP oligomer mobility in living cell nuclei. PLoS One *4*, 1–13.

Eckert, A.F., Gao, P., Wesslowski, J., Wang, X., Rath, J., Nienhaus, K., Davidson, G., and

1339 Nienhaus, G.U. (2020). Measuring ligand-cell surface receptor affinities with axial line-
1340 scanning fluorescence correlation spectroscopy. Elife *9*.

1341 Elson, E.L. (2011). Fluorescence correlation spectroscopy: Past, present, future. Biophys. J.
1342 *101*, 2855–2870.

1343 Essers, M.A.G.G., De Vries-Smits, L.M.M.M., Barker, N., Polderman, P.E., Burgering, B.M.T.T.,
1344 and Korswagen, H.C. (2005). Functional interaction between β-catenin and FOXO in
1345 oxidative stress signaling. Science (80-.). *308*, 1181–1184.

1346 Essletzbichler, P., Konopka, T., Santoro, F., Chen, D., Gapp, B. V., Kralovics, R.,
1347 Brummelkamp, T.R., Nijman, S.M.B., and Bürckstümmer, T. (2014). Megabase-scale deletion
1348 using CRISPR/Cas9 to generate a fully haploid human cell line. Genome Res. *24*, 2059–2065.

1349 Fagotto, F., Glück, U., and Gumbiner, B.M. (1998). Nuclear localization signal-independent
1350 and importin/karyopherin-independent nuclear import of β-catenin. Curr. Biol. *8*, 181–190.

1351 Fagotto, F., Jho, E.H., Zeng, L., Kurth, T., Joos, T., Kaufmann, C., and Costantini, F. (1999).
1352 Domains of Axin involved in protein-protein interactions, Wnt pathway inhibition, and
1353 intracellular localization. J. Cell Biol. *145*, 741–756.

1354 Faux, M.C., Coates, J.L., Catimel, B., Cody, S., Clayton, A.H.A., Layton, M.J., and Burgess, A.W.
1355 (2008). Recruitment of adenomatous polyposis coli and beta-catenin to axin-puncta.
1356 Oncogene *27*, 5808–5820.

1357 Fiedler, M., Mendoza-Topaz, C., Rutherford, T.J., Mieszczanek, J., and Bienz, M. (2011).
1358 Dishevelled interacts with the DIX domain polymerization interface of Axin to interfere with
1359 its function in down-regulating β-catenin. Proc. Natl. Acad. Sci. U. S. A. *108*, 1937–1942.

1360 Fiedler, M., Graeb, M., Mieszczanek, J., Rutherford, T.J., Johnson, C.M., and Bienz, M.

(2015). An ancient Pygo-dependent Wnt enhanceosome integrated by chip/LDB-SSDP. Elife *4*, 1–22.

Franz, A., Shlyueva, D., Brunner, E., Stark, A., and Basler, K. (2017). Probing the canonicity of the Wnt/Wingless signaling pathway. PLoS Genet. *13*, 1–18.

Fuerer, C., Nostro, M.C., and Constam, D.B. (2014). Nodal·Gdf1 heterodimers with bound prodomains enable serum-independent nodal signaling and endoderm differentiation. J. Biol. Chem. *289*, 17854–17871.

Gammons, M., and Bienz, M. (2018). Multiprotein complexes governing Wnt signal transduction. Curr. Opin. Cell Biol. *51*, 42–49.

Gerlach, J.P., Emmink, B.L., Nojima, H., Kranenburg, O., and Maurice, M.M. (2014). Wnt signalling induces accumulation of phosphorylated β-catenin in two distinct cytosolic complexes. Open Biol. *4*, 140120.

Gibson, D.G., Young, L., Chuang, R.Y., Venter, J.C., Hutchison, C.A., and Smith, H.O. (2009). Enzymatic assembly of DNA molecules up to several hundred kilobases. Nat. Methods *6*, 343–345.

Gibson, T.J., Seiler, M., and Veitia, R.A. (2013). The transience of transient overexpression. Nat. Methods *10*, 715–721.

Goedhart, J. (2019). PlotsOfDifferences - a web app for the quantitative comparison of unpaired data. BioRxiv 578575.

Goedhart, J., von Stetten, D., Noirclerc-Savoye, M., Lelimousin, M., Joosen, L., Hink, M.A., van Weeren, L., Gadella, T.W.J., and Royant, A. (2012). Structure-guided evolution of cyan fluorescent proteins towards a quantum yield of 93%. Nat. Commun. *3*, 751.

1383 Gottardi, C.J., and Gumbiner, B.M. (2004). Distinct molecular forms of β-catenin are
1384 targeted to adhesive or transcriptional complexes. J. Cell Biol. *167*, 339–349.

1385 Hampf, M., and Gossen, M. (2006). A protocol for combined Photinus and Renilla luciferase
1386 quantification compatible with protein assays. Anal. Biochem. *356*, 94–99.

1387 Hendriksen, J., Jansen, M., Brown, C.M., van der Velde, H., van Ham, M., Galjart, N.,
1388 Offerhaus, G.J., Fagotto, F., and Fornerod, M. (2008). Plasma membrane recruitment of
1389 dephosphorylated β-catenin upon activation of the Wnt pathway. J. Cell Sci. *121*, 1793–
1390 1802.

1391 Hink, M. a. (2014). Quantifying intracellular dynamics using fluorescence fluctuation
1392 spectroscopy. Protoplasma *251*, 307–316.

1393 Holstein, T.W. (2012). The evolution of the wnt pathway. Cold Spring Harb. Perspect. Biol. *4*,
1394 1–17.

1395 Holzmann, J., Politi, A.Z., Nagasaka, K., Hantsche-Grininger, M., Walther, N., Koch, B., Fuchs,
1396 J., Dürnberger, G., Tang, W., Ladurner, R., et al. (2019). Absolute quantification of cohesin,
1397 CTCF and their regulators in human cells. Elife *8*, 1–31.

1398 Hu, M., Kurobe, M., Jeong, Y.J., Fuerer, C., Ghole, S., Nusse, R., and Sylvester, K.G. (2007).
1399 Wnt/β-catenin signaling in murine hepatic transit amplifying progenitor cells.
1400 Gastroenterology *133*, 1579–1591.

1401 Jacobsen, A., Heijmans, N., Verkaar, F., Smit, M.J., Heringa, J., van Amerongen, R., and
1402 Feenstra, K.A. (2016). Construction and experimental validation of a Petri net model of
1403 Wnt/β-catenin signaling. PLoS One *11*, 1–30.

1404 Jamieson, C., Sharma, M., and Henderson, B.R. (2011). Regulation of β-catenin nuclear

dynamics by GSK-3β involves a LEF-1 positive feedback loop. Traffic *12*, 983–999.

Kafri, P., Hasenson, S.E., Kanter, I., Sheinberger, J., Kinor, N., Yunger, S., and Shav-Tal, Y. (2016). Quantifying β-catenin subcellular dynamics and cyclin D1 mRNA transcription during Wnt signaling in single living cells. Elife *5*, 1–29.

Kaur, G., Costa, M.W., Nefzger, C.M., Silva, J., Fierro-González, J.C., Polo, J.M., Bell, T.D.M.M., and Plachta, N. (2013). Probing transcription factor diffusion dynamics in the living mammalian embryo with photoactivatable fluorescence correlation spectroscopy. Nat. Commun. *4*, 1637.

Kitazawa, M., Hatta, T., Ogawa, K., Fukuda, E., Goshima, N., and Natsume, T. (2017). Determination of rate-limiting factor for formation of beta-catenin destruction complexes using absolute protein quantification. J. Proteome Res. *16*, 3576–3584.

Kormish, J.D., Sinner, D., and Zorn, A.M. (2010). Interactions between SOX factors and Wnt/β-catenin signaling in development and disease. Dev. Dyn. *239*, 56–68.

Kotecki, M., Reddy, P.S.S., and Cochran, B.H. (1999). Isolation and characterization of a near-haploid human cell line. Exp. Cell Res. *252*, 273–280.

Kremers, G.-J., Goedhart, J., van den Heuvel, D.J., Gerritsen, H.C., and Gadella, T.W.J. (2007). Improved green and blue fluorescent proteins for expression in bacteria and mammalian cells. Biochemistry *46*, 3775–3783.

Kremers, G.J., Goedhart, J., Van Munster, E.B., Gadella, T.W.J.J., Munster, E.B. Van, and Gadella, T.W.J.J. (2006). Cyan and yellow super fluorescent proteins with improved brightness , protein folding , and FRET förster radius. Biochemistry *45*, 6570–6580.

Krieghoff, E., Behrens, J., and Mayr, B. (2006). Nucleo-cytoplasmic distribution of β-catenin

1427 is regulated by retention. J. Cell Sci. *119*, 1453–1463.

1428 Kunttas-Tatli, E., Roberts, D.M., and McCartney, B.M. (2014). Self-association of the APC
1429 tumor suppressor is required for the assembly, stability, and activity of the Wnt signaling
1430 destruction complex. Mol. Biol. Cell *25*, 3424–3436.

1431 Lam, C.S., Mistri, T.K., Foo, Y.H., Sudhaharan, T., Gan, H.T., Rodda, D., Lim, L.H., Chou, C.,
1432 Robson, P., Wohland, T., et al. (2012). DNA-dependent Oct4-Sox2 interaction and diffusion
1433 properties characteristic of the pluripotent cell state revealed by fluorescence spectroscopy.
1434 Biochem. J. *448*, 21–33.

1435 Latres, E., Chiaur, D.S., and Pagano, M. (1999). The human F box protein β-Trcp associates
1436 with the Cul1/Skp1 complex and regulates the stability of β-catenin. Oncogene *18*, 849–854.

1437 Lebensohn, A.A.M., Dubey, R., Neitzel, L.R., Tacchelly-Benites, O., Yang, E., Marceau, C.D.,
1438 Davis, E.M., Patel, B.B., Bahrami-Nejad, Z., Travaglini, K.J., et al. (2016). Comparative genetic
1439 screens in human cells reveal new regulatory mechanisms in WNT signaling. Elife *5*, e21459.

1440 Lee, E., Salic, A., Krüger, R., Heinrich, R., and Kirschner, M.W. (2003). The roles of APC and
1441 axin derived from experimental and theoretical analysis of the Wnt pathway. PLoS Biol. *1*,
1442 116–132.

1443 Li, V.S.W., Ng, S.S., Boersema, P.J., Low, T.Y., Karthaus, W.R., Gerlach, J.P., Mohammed, S.,
1444 Heck, A.J.R., Maurice, M.M., Mahmoudi, T., et al. (2012). Wnt signaling through inhibition of
1445 β-catenin degradation in an intact Axin1 complex. Cell *149*, 1245–1256.

1446 Lim, X., Tan, S., Koh, W.W.L.C., Chau, R., Yan, K., Kuo, C.J., van Amerongen, R., Klein, A.M.,
1447 and Nusse, R. (2013). Interfollicular epidermal stem cells self-renew via autocrine Wnt
1448 signaling. Science (80-.). *342*, 1226–1230.

1449 Liu, C., Li, Y., Semenov, M., Han, C., Baeg, G.-H.H., Tan, Y., Zhang, Z., Lin, X., and He, X.
1450 (2002). Control of β-catenin phosphorylation/degradation by a dual-kinase mechanism. Cell
1451 *108*, 837–847.

1452 Liu, X., Rubin, J.S., and Kimmel, A.R. (2005). Rapid, Wnt-induced changes in GSK3β
1453 associations that regulate β-catenin stabilization are mediated by Gα proteins. Curr. Biol. *15*,
1454 1989–1997.

1455 Livak, K.J., and Schmittgen, T.D. (2001). Analysis of relative gene expression data using real-
1456 time quantitative PCR and the 2-ΔΔCT method. Methods *25*, 402–408.

1457 Loh, K.M., van Amerongen, R., and Nusse, R. (2016). Generating cellular diversity and spatial
1458 form: Wnt signaling and the evolution of multicellular animals. Dev. Cell *38*, 643–655.

1459 Lui, T.T.H., Lacroix, C., Ahmed, S.M., Goldenberg, S.J., Leach, C.A., Daulat, A.M., and Angers,
1460 S. (2011). The ubiquitin-specific protease USP34 regulates Axin stability and Wnt/β-Catenin
1461 Signaling. Mol. Cell. Biol. *31*, 2053–2065.

1462 Lustig, B., Jerchow, B., Sachs, M., Weiler, S., Pietsch, T., Karsten, U., van de Wetering, M.,
1463 Clevers, H., Schlag, P.M., Birchmeier, W., et al. (2002). Negative feedback loop of Wnt
1464 signaling through upregulation of conductin/axin2 in colorectal and liver tumors. Mol. Cell.
1465 Biol. *22*, 1184–1193.

1466 Macháň, R., and Wohland, T. (2014). Recent applications of fluorescence correlation
1467 spectroscopy in live systems. FEBS Lett. *588*, 3571–3584.

1468 Mahen, R., Koch, B., Wachsmuth, M., Politi, A.Z., Perez-gonzalez, A., Mergenthaler, J., Cai, Y.,
1469 Ellenberg, J., and Lippincott-schwartz, J. (2014). Comparative assessment of fluorescent
1470 transgene methods for quantitative imaging in human cells. Mol. Biol. Cell *25*, 3610–3618.

1471 Maher, M.T., Mo, R., Flozak, A.S., Peled, O.N., and Gottardi, C.J. (2010). β-Catenin
1472 phosphorylated at Serine 45 is spatially uncoupled from β-Catenin phosphorylated in the
1473 GSK3 domain: Implications for signaling. PLoS One *5*, e10184.

1474 Massey, J., Liu, Y., Alvarenga, O., Saez, T., Schmerer, M., and Warmflash, A. (2019). Synergy
1475 with TGFβ ligands switches WNT pathway dynamics from transient to sustained during
1476 human pluripotent cell differentiation. Proc. Natl. Acad. Sci. U. S. A. *116*, 4989–4998.

1477 Mendoza-Topaz, C., Mieszczanek, J., and Bienz, M. (2011). The Adenomatous polyposis coli
1478 tumour suppressor is essential for Axin complex assembly and function and opposes Axin's
1479 interaction with Dishevelled. Open Biol. *1*, 110013.

1480 Molenaar, M., van de Wetering, M., Oosterwegel, M., Peterson-Maduro, J., Godsave, S.,
1481 Korinek, V., Roose, J., Destrée, O., and Clevers, H. (1996). XTcf-3 transcription factor
1482 mediates beta-catenin-induced axis formation in Xenopus embryos. Cell *86*, 391–399.

1483 Morin, P.J., Sparks, A.B., Korinek, V., Barker, N., Clevers, H., Vogelstein, B., and Kinzler, K.W.
1484 (1997). Activation of β-catenin-Tcf signaling in colon cancer by mutations in β-catenin or
1485 APC. Science (80-.).

1486 Nusse, R., and Clevers, H. (2017). Wnt/β-Catenin signaling, disease, and emerging
1487 therapeutic modalities. Cell *169*, 985–999.

1488 Pack, C., Saito, K., Tamura, M., and Kinjo, M. (2006). Microenvironment and effect of energy
1489 depletion in the nucleus analyzed by mobility of multiple oligomeric EGFPs. Biophys. J. *91*,
1490 3921–3936.

1491 Pack, C.G., Yukii, H., Toh-E, A., Kudo, T., Tsuchiya, H., Kaiho, A., Sakata, E., Murata, S.,
1492 Yokosawa, H., Sako, Y., et al. (2014). Quantitative live-cell imaging reveals spatio-temporal

dynamics and cytoplasmic assembly of the 26S proteasome. Nat. Commun. *5*, 3396.

Petrášek, Z., and Schwille, P. (2008). Precise measurement of diffusion coefficients using scanning fluorescence correlation spectroscopy. Biophys. J. *94*, 1437–1448.

Polakis, P. (2000). Wnt signaling and cancer. Genes Dev. *14*, 1837–1851.

Pronobis, M.I., Rusan, N.M., and Peifer, M. (2015). A novel GSK3-regulated APC:Axin interaction regulates Wnt signaling by driving a catalytic cycle of efficient βcatenin destruction. Elife *4*, 1–31.

Pronobis, M.I., Deuitch, N., Posham, V., Mimori-Kiyosue, Y., and Peifer, M. (2017). Reconstituting regulation of the canonical Wnt pathway by engineering a minimal β-catenin destruction machine. Mol. Biol. Cell *28*, 41–53.

Ran, F.A., Hsu, P.D., Wright, J., Agarwala, V., Scott, D. a, and Zhang, F. (2013). Genome engineering using the CRISPR-Cas9 system. Nat. Protoc. *8*, 2281–2308.

Rim, E.Y., Kinney, L.K., and Nusse, R. (2020). Beta-catenin-mediated Wnt signal transduction proceeds through an endocytosis-independent mechanism. Mol. Biol. Cell mbc.E20-02-0114.

Sayat, R., Leber, B., Grubac, V., Wiltshire, L., and Persad, S. (2008). O-GlcNAc-glycosylation of β-catenin regulates its nuclear localization and transcriptional activity. Exp. Cell Res. *314*, 2774–2787.

Schaefer, K.N., and Peifer, M. (2019). Wnt/beta-catenin signaling regulation and a role for biomolecular condensates. Dev. Cell *48*, 429–444.

Schaefer, K.N., Bonello, T.T., Zhang, S., Williams, C.E., Roberts, D.M., McKay, D.J., and Peifer,

1514 M. (2018). Supramolecular assembly of the beta-catenin destruction complex and the effect
1515 of Wnt signaling on its localitzation, molecular size, and activity in vivo.

1516 Schaefer, K.N., Pronobis, M., Williams, C.E., Zhang, S., Bauer, L., Goldfarb, D., Yan, F., Major,
1517 M. Ben, and Peifer, M. (2020). Wnt regulation: Exploring Axin-Disheveled interactions and
1518 defining mechanisms by which the SCF E3 ubiquitin ligase is recruited to the destruction
1519 complex. Mol. Biol. Cell mbcE19110647.

1520 Schmittgen, T.D., and Livak, K.J. (2008). Analyzing real-time PCR data by the comparative CT
1521 method. Nat. Protoc. *3*, 1101–1108.

1522 Schmitz, Y., Rateitschak, K., and Wolkenhauer, O. (2013). Analysing the impact of nucleo-
1523 cytoplasmic shuttling of β-catenin and its antagonists APC, Axin and GSK3 on Wnt/β-catenin
1524 signalling. Cell. Signal. *25*, 2210–2221.

1525 Schuijers, J., Mokry, M., Hatzis, P., Cuppen, E., and Clevers, H. (2014). Wnt-induced
1526 transcriptional activation is exclusively mediated by TCF/LEF. EMBO J. *33*, 146–156.

1527 Schwarz-Romond, T., Fiedler, M., Shibata, N., Butler, P.J.G., Kikuchi, A., Higuchi, Y., and
1528 Bienz, M. (2007). The DIX domain of Dishevelled confers Wnt signaling by dynamic
1529 polymerization. Nat. Struct. Mol. Biol. *14*, 484–492.

1530 Spink, K.E., Polakis, P., and Weis, W.I. (2000). Structural basis of the Axin–adenomatous
1531 polyposis coli interaction. EMBO J. *19*, 2270–2279.

1532 Stamos, J.L., Chu, M.L.-H.H., Enos, M.D., Shah, N., and Weis, W.I. (2014). Structural basis of
1533 GSK-3 inhibition by N-terminal phosphorylation and by the Wnt receptor LRP6. Elife *2014*,
1534 e01998.

1535 Taelman, V.F., Dobrowolski, R., Plouhinec, J.L., Fuentealba, L.C., Vorwald, P.P., Gumper, I.,

1536 Sabatini, D.D., and De Robertis, E.M. (2010). Wnt signaling requires sequestration of
1537 Glycogen Synthase Kinase 3 inside multivesicular endosomes. Cell *143*, 1136–1148.

1538 Tan, C.W., Gardiner, B.S., Hirokawa, Y., Layton, M.J., Smith, D.W., and Burgess, A.W. (2012).
1539 Wnt signalling pathway parameters for mammalian cells. PLoS One *7*, 31882.

1540 Tan, C.W., Gardiner, B.S., Hirokawa, Y., Smith, D.W., and Burgess, A.W. (2014). Analysis of
1541 Wnt signaling β-catenin spatial dynamics in HEK293T cells. BMC Syst. Biol. *8*, 44.

1542 Thorvaldsen, T.E., Pedersen, N.M., Wenzel, E.M., Schultz, S.W., Brech, A., Liestøl, K., Waaler,
1543 J., Krauss, S., and Stenmark, H. (2015). Structure, dynamics, and functionality of tankyrase
1544 inhibitor-induced degradasomes. Mol. Cancer Res. *13*, 1487–1501.

1545 van Tienen, L.M., Mieszczanek, J., Fiedler, M., Rutherford, T.J., and Bienz, M. (2017).
1546 Constitutive scaffolding of multiple Wnt enhanceosome components by legless/BCL9. Elife
1547 *6*, 1–23.

1548 Tortelote, G.G., Reis, R.R., de Almeida Mendes, F., and Abreu, J.G. (2017). Complexity of the
1549 Wnt/β-catenin pathway: Searching for an activation model. Cell. Signal. *40*, 30–43.

1550 Tran, H., and Polakis, P. (2012). Reversible modification of adenomatous polyposis coli (APC)
1551 with K63-linked polyubiquitin regulates the assembly and activity of the β-catenin
1552 destruction complex. J. Biol. Chem. *287*, 28552–28563.

1553 Valenta, T., Hausmann, G., and Basler, K. (2012). The many faces and functions of β-catenin.
1554 EMBO J. *31*, 2714–2736.

1555 Verkaar, F., Cadigan, K.M., and van Amerongen, R. (2012). Celebrating 30 years of Wnt
1556 signaling. Sci. Signal. *5*, mr2.

1557 Wachsmuth, M., Waldeck, W., and Langowski, J. (2000). Anomalous diffusion of fluorescent
1558 probes inside living cell investigated by spatially-resolved fluorescence correlation
1559 spectroscopy. J. Mol. Biol. *298*, 677–689.

1560 van der Wal, T., and van Amerongen, R. (2020). Walking the tight wire between cell
1561 adhesion and WNT signalling: a balancing act for β-catenin. Open Biol. *10*, 200267.

1562 Wiechens, N., and Fagotto, F. (2001). CRM1- and Ran-independent nuclear export of β-
1563 catenin. Curr. Biol. *11*, 18–28.

1564 Wiese, K.E., Nusse, R., and van Amerongen, R. (2018). Wnt signalling: conquering
1565 complexity. Development *145*, dev165902.

1566 Wu, X., Tu, X., Joeng, K.S., Hilton, M.J., Williams, D.A., and Long, F. (2008). Rac1 Activation
1567 Controls Nuclear Localization of β-catenin during Canonical Wnt Signaling. Cell *133*, 340–
1568 353.

1569 Yaguchi, K., Yamamoto, T., Matsui, R., Tsukada, Y., Shibanuma, A., Kamimura, K., Koda, T.,
1570 and Uehara, R. (2018). Uncoordinated centrosome cycle underlies the instability of non-
1571 diploid somatic cells in mammals. J. Cell Biol. *217*, 2463–2483.

1572 Yap, A.S., Brieher, W.M., and Gumbiner, B.M. (1997). Molecular and functional analysis of
1573 cadherin-based adherens junctions. Annu. Rev. Cell Dev. Biol. *13*, 119–146.

1574 Yokoya, F., Imamoto, N., Tachibana, T., and Yoneda, Y. (1999). β-Catenin can be transported
1575 into the nucleus in a ran-unassisted manner. Mol. Biol. Cell *10*, 1119–1131.

1576 Yokoyama, N., Markova, N.G., Wang, H., and Malbon, C.C. (2012). Assembly of Dishevelled
1577 3-based supermolecular complexes via phosphorylation and Axin. J. Mol. Signal. *7*, 8.

1578 Zhan, T., Rindtorff, N., and Boutros, M. (2017). Wnt signaling in cancer. Oncogene *36*, 1461–

1579 1473.

1580